A mechanistic approach to studying the antimicrobial and anticancer activity of GL13K-based peptides through their interaction with model membranes.

Javier Porro Suardiaz

A Thesis
in
The Department
of
Chemistry and Biochemistry

Presented in Partial Fulfillment of the Requirements
for the Degree of Master Science (Biochemistry) at
Concordia University
Montréal, Québec, Canada

December, 2021

CONCORDIA UNIVERSITY

SCHOOL OF GRADUATE STUDIES

This is to certify that the thesis prepared

By: Javier Porro Suardiaz

Entitled: A mechanistic approach to studying the antimicrobial and anticancer activity of GL13K-based peptides through their interaction with model membranes.

and submitted in partial fulfillment of the requirements for the degree of

Master of Science (Biochemistry)

complies with the regulations of the University and meets the accepted standards with respect to originality and quality.

Signed by the final examining committee:

Chair_____ Dr. Yves Gélinas

Examiner_____ Dr. Peter Pawelek

Examiner_____ Dr. Paul Joyce

Supervisor_____ Dr. Christine DeWolf

Approved by _____
Yves Gélinas (Graduate Program Director)

_____ 2022 _____
Pascale Sicotte, Dean of Faculty of Arts and Science

ABSTRACT

A mechanistic approach to studying the antimicrobial and anticancer activity of GL13K-based peptides through their interaction with model membranes.

Javier Porro Suardiaz

GL13K is a broad-spectrum antimicrobial peptide with selective bactericidal and antibiofilm activity, which makes it an attractive candidate for targeted antibiotic applications. Many antimicrobial peptides are multifunctional and have exhibited anticancer activity. Along with this precedent, GL13K's potency on cancer has not been yet reported. Therefore, we proceeded to a preliminary assessment of anticancer activity for both D- and L-GL13K enantiomers in cancer cell lines. It emerged that D-GL13K showed selective toxicity in cancer cells. Such enantiomeric differences have previously been attributed to their resistance to proteolytic degradation. To probe if distinct mechanisms of interaction are involved in either their antibacterial vs anticancer activity, we evaluated the roles of peptide chirality and membrane composition by studying the interaction of D- and L-GL13K, as well as a newly designed GL28K peptide, with model membranes that mimic the lipid composition of those in human cancer, erythrocyte cells and bacteria. For this purpose, a combination of bulk and surface-specific biophysical techniques was used. The enantiomers showed differential interactions that can depend on the lipid composition in agreement with their activity (in the absence of proteases) as evidenced by greater binding and insertion in the cancer model membranes. However, in contrast to results in bacterial models neither enantiomer of GL13K displayed a crystalline beta-sheet conformation in presence of the eukaryotic cell model, despite this being a hallmark of their activity with bacterial models. The molecular origins and significance of these results will be discussed.

Acknowledgements

First and foremost, I would like to thank especially my supervisor Dr. Christine DeWolf for her unwavering support, guidance, patience, consideration, and many encouragements along the way. She has been the determining factor for the completion of the degree.

I kindly thank my supervisory committee members, Dr. Peter Pawelek and Dr. Paul Joyce, whose insightful comments, suggestions, and expertise contributed to my training and shaping the project.

To all my lab mates, I am very grateful. They have provided me with great memories and helpful feedback. They were utmost supportive with the X-ray scattering experiments, especially Hala Youssef, Renaud Miclette, Janet Gaba, Jennifer Coulombe, Dalia Ali.

I would like to extend my gratitude to Dr. Rolf Schmidt for his guidance, truthful advice, and unparalleled technical support. Many thanks to Dr. Alissa Piekny for providing resources to support for the cell assays, and to Dr. Brandon Findlay for the training on the antimicrobial testing assay.

Drs. Judith and Jack Kornblatt have my heartfelt appreciation for their assistance with the Circular Dichroism, SPR, and their thoughtful feedback. I thank them for facilitating me their lab to perform the SPR experiments and giving me their kind support.

My sincere gratitude to Dr. Christian Salesse and Benjamin Martial in Université Laval for their guidance, kind help, and sharing their professional expertise on the PM-IRRAS experiments.

I am truly grateful to my friends at Concordia who brought me joy and helped me up from the downs. I will always treasure the times shared together: Franklin, Chris, Cynthia, Gabriella, Rafael, Nav, and Alicia. To Melika Mirabi always.

Nothing would have been possible without my family, especially my parents. They have paved the foundations to all my accomplishments. For having them, I feel blessed.

I feel uniquely grateful to my grandmother, who at her 90s still found ways to inspire and motivate me in her extraordinary ways. Her quotes kept me grounded and encouraged. Wherever you are, my love is with you always.

Table of Contents

List of figures

List of tables

List of equations

List of abbreviations

ACPs	Anticancer peptides
AFM	Atomic Force Microscopy
AMPs	Antimicrobial peptides
CD	Circular Dichroism
CF	Carboxyfluorescein
Chol	Cholesterol
CL	Cardiolipin or 1',3'-bis[1,2-dioleoyl-sn-glycero-3-phospho]-glycerol (18:1)
CPP	Cell-penetrating peptide
DOPC	1,2-dioleoyl-sn-glycero-3-phosphocholine
DOPE	1,2-dioleoyl-sn-glycero-3-phosphoethanolamine
DOPG	1,2-dioleoyl-sn-glycero-3-phospho-(1'-rac-glycerol)
DOPS	1,2-dioleoyl-sn-glycero-3-phospho-L-Serine (18:1)
GIXD	Grazing incidence x-ray diffraction
IC_{50}	Concentration that killed or inhibited growth of 50% of the cells
IM / PM	Inner membrane or Plasma membrane
K_D	Dissociation constant at equilibrium
Ld	Liquid disordered
Lo	Liquid ordered
LPS	Lipopolysaccharides
SPR / LSPR	Surface Plasmon Resonance / Localized SPR
LTA	Lipoteichoic acids
LUVs	Large Unilamellar Vesicles or liposomes
MDR	Multidrug-resistant
MIC	Minimum Inhibitory Concentrations
MRSA	Methicillin-resistant *Staphylococcus aureus*
NMR	Nuclear magnetic resonance
OM	Outer membrane
PBS	Phosphate buffered saline
PE	Phosphatidylethanolamine
PG	Phosphatidylglycerol
P/L ratio	Peptide to lipid ratio
PLs	Phospholipids
PM	Plasma membrane or Inner membrane
PM-IRRAS	Polarization-Modulation Infrared Reflection Absorption Spectroscopy
PS	Phosphatidylserine
RBC	Erythrocytes or red blood cells
SAR	Structure-activity relationship
SM	Sphingomyelin
TA	Teichoic acids
WT	Wild type
XRR	X-ray reflectivity

Chapter 1. **Introduction**

1.1. Foundations for alternatives to antibiotics and chemotherapeutics

Extensive use of antibiotics in therapeutic treatment and in livestock and aquaculture has led to the emergence of antimicrobial resistance worldwide. The occurrence of multidrug-resistant (MDR) pathogenic bacteria is rendering antibiotic therapies inefficient and endangering millions of lives. To the point that the World Economic Forum has identified antibiotic resistance as a global risk that surpasses the management or mitigation capacity of any nation or organization alone (1, 2).

Despite the epidemiological surveillance programs, the frequency of nosocomial infections continues to rise. Immunocompromised individuals are particularly vulnerable to infection and chemotherapeutic regimens make all oncology patients highly susceptible to a multitude of opportunistic and MDR pathogenic microorganisms (3). The first reports of penicillin resistance becoming a clinical problem date from the 1950s, while methicillin-resistant *Staphylococcus aureus* (MRSA) has been reported since the 1960s. The number of bacterial isolates that are confirmed to produce resistant genes to conventional antibiotics has greatly increased since then, especially in the last decades. However, the quantity of new systemic antibiotics developed and approved has decreased steadily over the past thirty years (2, 4). Therefore, fewer options for treatment are left available leading to prolonged diseases and higher morbidity and mortality rates.

Worrying estimations predict that by 2050, antimicrobial resistance will cause nearly 10 million deaths globally, surpassing even cancer (5). In addition, it is been projected that global consumption of antibiotics from 2010 to 2030 will increase by 67% in agriculture, and 99% amongst five of the most populated nations (6). All of this reflects the current need for more effective and broader use antimicrobial agents that are able to circumvent antibiotic resistance, for which antimicrobial peptides have emerged as attractive candidates (7–10).

1.2. Antimicrobial peptides (AMPs)

Antimicrobial peptides (AMPs) or host defense peptides are ubiquitous in nature and one of the main effectors of the innate immune response against pathogens in probably all taxonomic

kingdoms (11). They arise as a promising alternative to antibiotics, as supported by the progressive expansion of the AMP research field and growing number of publications in the last few decades (12). AMPs generally consist of less than 100 amino acids and show great structural diversity in amino acid sequences, length, charge, folding and hydrophobicity. From natural peptides to synthetic variants, they can be broadly classified in four major classes according to their secondary structure: α-helical, β-sheet, loop and extended or unstructured peptides (13), though other more comprehensive classifications may be used (8, 14).

Moreover, AMPs show wide functional plasticity, with a broad spectrum of antimicrobial activities against bacteria, yeasts, fungi, viruses and some parasites, in addition to immunomodulatory effects and anticancer activity (15–18). AMPs with the capacity to kill cancer cells are also referred as anticancer peptides (ACPs).

AMPs/ACPs are selective for negatively charged membranes over zwitterionic eukaryotic membranes due to two main recurrent physicochemical features: cationic charge and amphipathicity. AMPs selectivity is advantageous for their use over conventional antibiotics given that a development of microbial resistance by gene mutation is less prone to occur *via* modifying the composition of the phospholipid membrane. In contrast, most antibiotics have internal targets, or their action is directed to inhibit certain enzymatic pathways in bacterial cells. For which, bacteria present several mechanisms of resistance and intrinsic resistance genes that act against antibiotics of different classes, including β-lactams, fluoroquinolones and aminoglycosides (12, 19–22). Bacterial mechanisms of resistance to antibiotics include among others: down-regulation of porins, increased efflux or overexpression of efflux pumps, genetic mutation or post-translational modification of the antibiotic target, and chemical alteration or degradation of the antimicrobial agent (22).

Naturally occurring AMPs/ACPs may however be subjected to proteolysis, since they consist of L-amino acids which are degradable by proteases *in vivo* (23). This constitutes a disadvantage for a peptide-based therapy in the treatment of antibiotic-resistant bacterial infections and cancer. However, AMPs/ACPs ubiquity in nature provides a great variety of templates for the design of synthetic peptide analogs. The structural diversity of peptides can nowadays be consulted in databases online. One of the most cited and user friendly is Antimicrobial Peptide Database (APD

or APD3) (https://aps.unmc.edu/) which currently contains 3185 proved AMPs, out of which, only 16 are synthetic. At the time of writing this, the database includes 237 anticancer/antitumor peptides, and only one of them is synthetic. APD has classification schemes that facilitate identifying peptides by biological functions, unique structural motifs, available 2D and 3D structures, chemical and biochemical properties, targets, etc. This database also contains design and prediction tools that allow to identify novel AMPs/ACPs (24). Other noteworthy databases such as DAASP and LAMP, are listed in Gabernet et al. (25).

New peptides can be then designed and synthetized to enhance specific antimicrobial functions, improve their selectivity, diminish toxicity, or circumvent proteolysis for therapeutic applications. Introducing charged, hydrophobic or non-natural amino acids in specific positions, changing their chirality or adding non-coded chemical modifications are some of the approaches used in research (14, 26). Following this trend, many natural and synthetic AMPs/ACPs have been studied, some have entered clinical trials, and some have now reached the market (18, 27).

1.2.1. Membrane composition of bacteria and molecular targets for AMPs

For the scope of this thesis, this section is limited to Gram-positive and Gram-negative bacteria. Mycoplasma, L-form bacteria and some archaebacteria are not considered.

Despite the differences between Gram-positives and Gram-negatives, both bacterial groups have a cytoplasmic membrane surrounded by a cell wall. The periplasm is between these and contains several ions, proteins and peptidoglycans involved in metabolic functions, transport, or exchange. Gram-negative bacteria contain an outer membrane (OM) that limits the periplasmic space until the inner membrane (IM). This is the main difference between both bacterial classes (Figure 1.1). The Gram-positive bacteria cell wall comprises many layers of peptidoglycan that stabilize their only membrane and it is thicker than Gram-negatives cell wall. Gram-positive bacteria also have teichoic (TA) and lipoteichoic acids (LTA), the latter anchored in the cytoplasmic membrane, while Gram-negative bacteria present lipopolysaccharides (LPS) as the major component of the outer leaflet of their outer membrane (28, 29).

Membranes in general are composed of three types of lipids: phosphoglycerides, sphingolipids, and steroids. All three types are amphiphilic, with a polar headgroup and nonpolar tail(s), but structural differences among them are responsible for different roles in membranes (30). Bacterial plasma membranes in both groups vary with the species according to the phospholipid composition, their headgroups and fatty acid moieties (Figure 1.1). The main lipid components of bacterial membranes are the negatively charged phosphatidylglycerol (PG) and cardiolipin (CL), with phosphatidylethanolamine (PE) as the predominant zwitterionic lipid. Other lipids are often found in small quantities, such as lysyl-PG (LPG), phosphatidylinositol (PI), phosphatidic acid (PA) and rarely phosphatidylserine (PS). Only very few bacterial groups present sphingolipids. Bacteria can also form phosphorus-free membrane lipids and usually do not have sterols (31).

In general, Gram-negative bacteria contain larger proportions of PE whereas Gram-positives have greater fractions of anionic PG. Bacteria can reduce the PG content while increasing CL, altering membrane composition while preserving the anionic charge. Bacteria have at least 15% of anionic lipids and can reach up to ~ 80% of either PG or CL, or a combination of the two. *Escherichia coli*, the standard model for studying bacterial membranes, comprises about 75% of the zwitterionic PE, with ~ 20% of the anionic lipids PG and CL (28, 29, 31). Tabulated information compiling membrane lipid composition of various Gram-positive and Gram-negative bacterial species is available in references 26, 29 and 30. The presence of peptidoglycans together with LPS, (L)TA and anionic lipids, permits the selective targeting of cationic AMPs for bacteria as opposed to eukaryotic cell membranes (28, 29, 31) (Figure 1.1 and Figure 1.4).

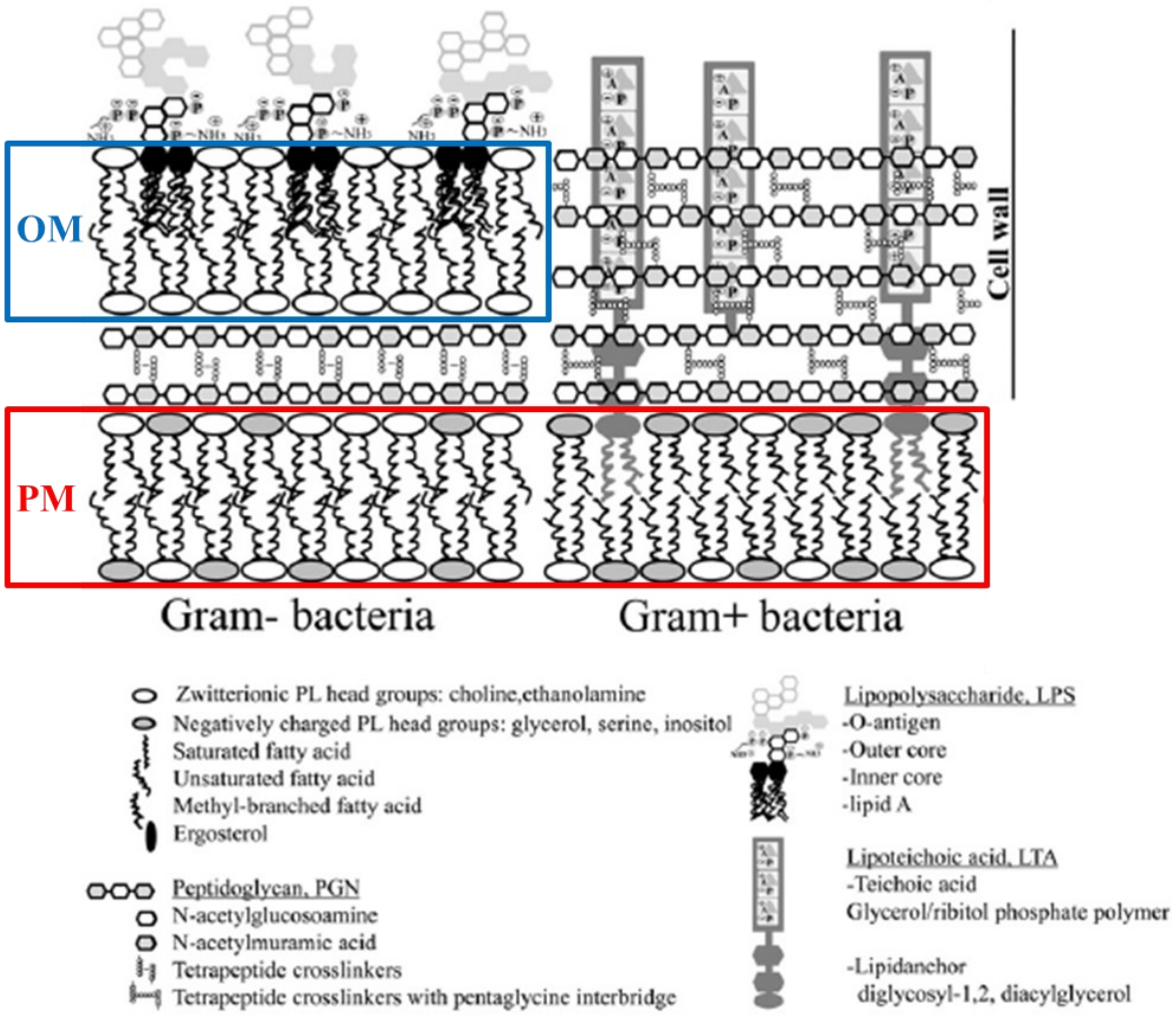

Figure 1.1. Schematic representation of bacterial cell walls showing the membrane composition and main differences between Gram-positive and Gram-negative bacteria. OM: Outer membrane; PM: plasma membrane or inner membrane. Adapted from Malanovic and Lohner (28).

The curvature strain of the membranes is another important property governed by the nature of lipids. PE and CL lipids possess a spontaneous negative curvature given their inverted cone geometry, whereas PC and PG have a lamellar more cylindrical shape (34). CL is located to the cellular poles in *E. coli* and in association with PE can form domains of higher intrinsic curvature, while PG rather forms flat lamellar lipid aggregates (31). It has been suggested that PE lipids are closely packed because of preferential intermolecular hydrogen bonding between the amino and phosphate groups or carbonyl group of the *sn*-2-chain, which favors structures with higher intrinsic curvature (35). Additionally, CL has shown to cause a condensing or stabilizing effect in zwitterionic monolayers with lamellar phospholipids (36, 37). In bacteria, PE and CL encounter

non-ideal mixing, so when AMPs bind to the anionic lipids, the interaction process can alter the membrane phase separation (35). Moreover, curvature changes may facilitate or limit the accessibility of AMPs to the membrane and their interactions with the lipid bilayer core (28, 29).

Gram-negative bacteria contain mostly saturated and unsaturated phospholipids with the main acyl chain distribution being 16:0, 18:0, 16:1 and 18:1 (first number designates the length of the hydrocarbon chains; second number indicates the quantity of unsaturations per chain, which is stereospecific) (28). In contrast, Gram-positive bacteria present more abundantly anteiso and iso-branched fatty acids with C15:0 and C17:0 chains distribution. *Staphylococcus aureus*, for example, contains only saturated membrane lipids with anteiso and iso-methyl branched chains that can functionally replace monounsaturated acyl chains found in other species (28, 38). Changes in charge, acyl chain length and distribution of phospholipids can influence the activity of AMPs (28, 35, 38).

Studies indicate that bacterial cell wall outer components, such as LPS and TA may facilitate AMP accumulation on the membrane surface due their negative charge, but it depends on the concentration of AMPs. The peptidoglycans layer usually contain proteolytic enzymes; however, it is relatively porous and freely penetrable for small molecules or peptides (39). LTA are considered anionic polymers with a strong potential to attract cationic molecules, and they may act as entrappers of AMPs or as ladder directing towards the inner membrane (28, 35).

1.2.2. Membrane composition of eukaryotic cells and molecular targets for anticancer peptides

Eukaryotic membranes differ from bacterial membranes mainly on surface charge and lipid composition. Mammalian cells normally present zwitterionic phospholipids on the outer leaflet of plasma membranes in contrast to the negatively charged components of bacteria. Normal mammalian cells keep an asymmetric lipid distribution across the bilayer of the plasma membrane, as shown in Figure 1.2. The cytosolic leaflet typically contains PE and the negatively charged PS. The overall composition of mammalian lipids is ~ 65% of glycerophospholipids (PC, PE, PS, PI), ~ 10% of sphingolipids and ~25% of sterols. The last two are always present in eukaryotes and are

abundant in the plasma membranes (40, 41). The phospholipid content varies in membranes of different organelles and cell types (42).

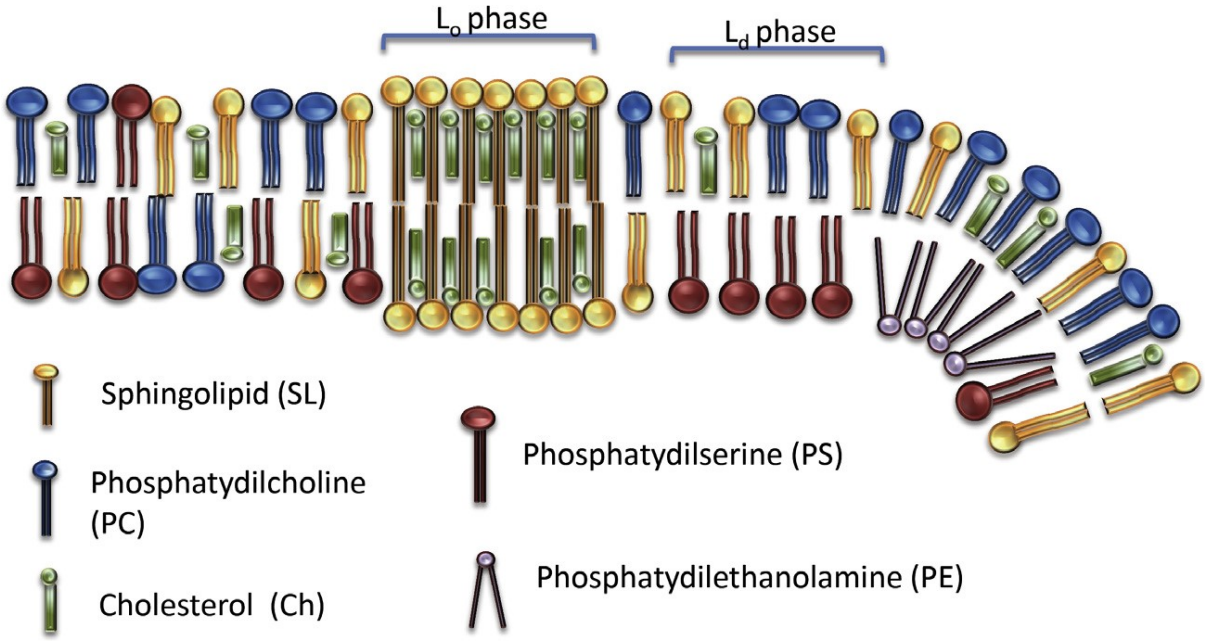

Figure 1.2. Representation of a eukaryotic cell membrane fragment with asymmetric lipid distribution. Phase separation is depicted: Lo) a liquid-ordered phase domain formed by a saturated sphingolipid and cholesterol, presenting a more rigid domain and tighter packing. The liquid-disordered (Ld) phase implies acyl chain conformational freedom and looser packing (34).

The lipids of biological membranes can exist in multiple phase states. At a physiological temperature, the cell membranes are generally considered to be in a liquid-disordered (Ld) phase, which is typified by looser packing and greater miscibility (43). In mixtures with some saturated lipids such as sphingomyelin, cholesterol can form what is known as a liquid-ordered (Lo) phase which comprises all-trans, ordered acyl chains but with the lateral fluidity of the disordered phase. Liquid ordered and liquid disordered phases differ in composition, lipid tail order and thickness (44). The well-ordered and solid-like gel phase (Lβ) can convert at the transition temperature (T_m) to the liquid crystalline (Lα) or liquid disordered (Ld) phase (Lα: lamellar phase with disordered acyl chains and rapid translational diffusion) (45, 46). The terms Lα and Ld are considered interchangeable and dependent only on the presence (Ld) or absence (Lα) of cholesterol (45). In the gel phase the hydrophobic tails are fully extended and in an all-trans conformation, whereas in the Ld, the tails have conformational freedom and are considered fluid. Interestingly, two or three

phases can coexist attending to the regions of macroscopic immiscibility produced by the lipid mixtures (46). Membrane fluidity is highly dependent on the composition, order of saturation of the acyl chains, and the presence of cholesterol. In cell membranes, preferential association of sphingolipids and cholesterol in some regions can promote more stable membrane-ordered assemblies with proteins and form dynamic rigid patches called “rafts” (41, 47).

Cancerous cells undergo metabolic and surface changes that can be exploited for the development of targeted cancer therapy (Figure 1.3). Two distinct hallmarks of cancer are promising for using AMPs/ACPs to selectively target their cell membrane over normal cells. One, is the reversal of the proton gradient rendering abnormal intracellular and the extracellular pH when compared with normal cells (48, 49). The other is that cancer cells lose the transmembrane lipid asymmetry, leading to the exposure of PE and the anionic PS in the outer leaflet (Figure 1.4). The display of phosphatidylserine along with sialic acid on glycoproteins (e.g. mucins) and heparan sulfate on proteoglycans on the outer membrane leaflet constitutes the main difference in membrane composition between normal and tumoral cells. Therefore, the same distinction in surface charge between bacterial and healthy eukaryotic cells, occurs between tumoral and normal cells. Thus, the action and specificity of cationic ACPs can be directed to the cancer cells carrying negative surface charge (50–53).

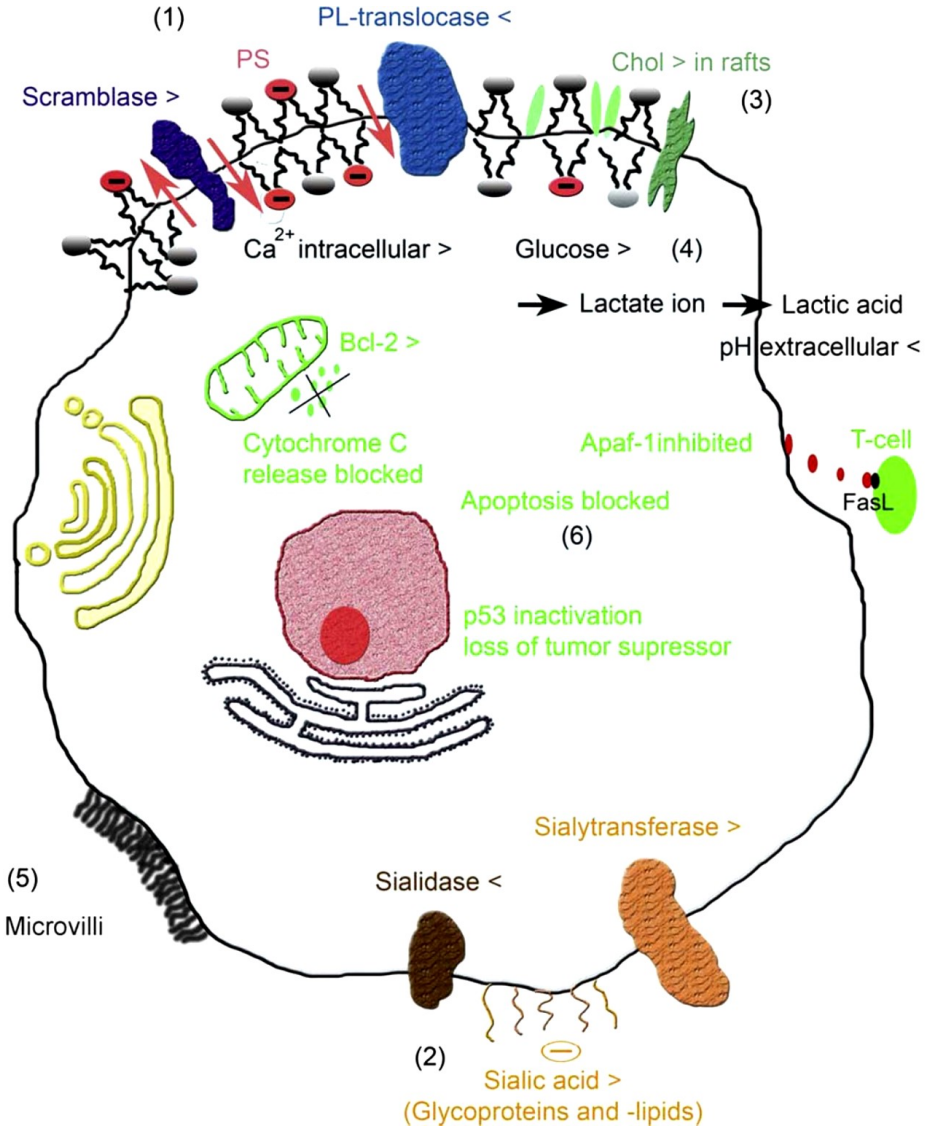

Figure 1.3. Representation of a cancer cell showing the targets and modifications that can drive the selective interaction of cationic ACPs with anionic molecules. (1) Exposure of PS due to inhibition of phospholipid–translocases. (2) Increased surface levels of sialic acid and glycolipids. (3) Changes in membrane fluidity, (4) lower extracellular pH, and (5) increased surface area (due to the presence of microvilli) may impact the susceptibility and activity of peptides. (6) Peptides that translocate into the cytosol can interact with anionic lipids of mitochondria triggering apoptosis, which is usually blocked in tumoral cells by mechanisms such as the inactivation of tumor suppressor p53 (54)**.**

PS not only serves as a target, but it also plays a physiological role (42). Additionally, PS can be used as a template for the recognition of cancer antigen 125 (CA 125) and has gained interest in the development of non-invasive imaging to support diagnosis and evaluation of treatment efficacy on cancer and cardiovascular disease (50–53, 55, 56). Other factors contributing to the selective

killing of cancer cells by ACPs include membrane fluidity and cell surface area. Though, there is conflicting evidence as to whether cancer cell membranes have a greater membrane fluidity or are less permeable than non-malignant cells (50–53, 55).

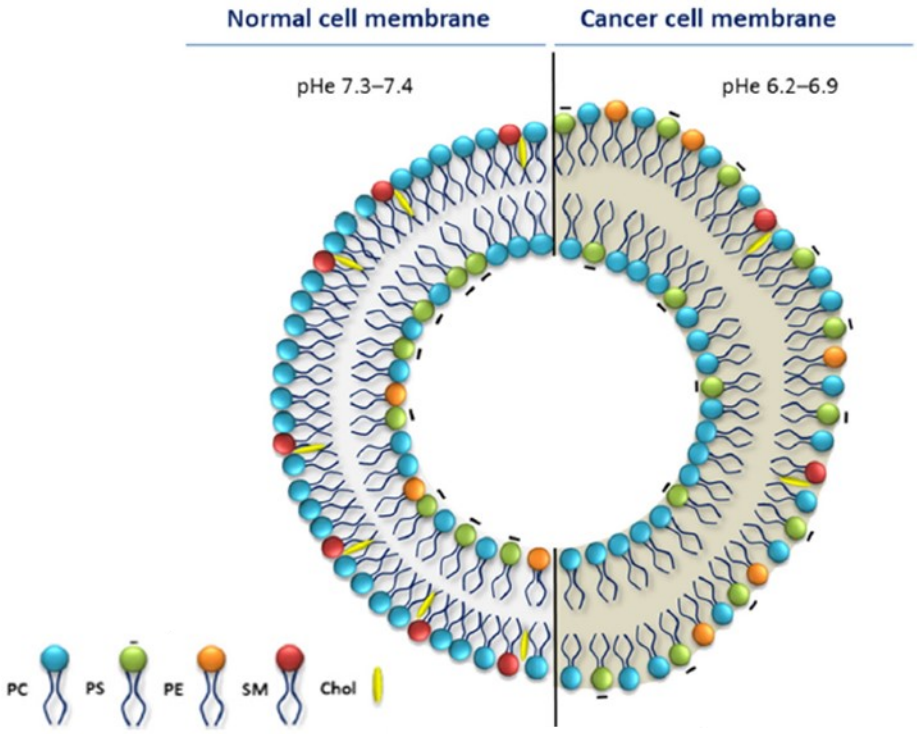

Figure 1.4. Representation of normal and cancer cell membranes illustrating the differential membrane composition extracellular pH (57)**. Exposure of anionic PS on the outer leaflet of cancer cells servers as a target for AMPs/ACP.**

Cancer membranes can present lipid domains such as caveolae and lipid rafts. The latter are planar formations in the nano to micro size range, richer in sphingolipids and cholesterol and can form in the outer leaflet. This lipid association can be dynamic and reversible, stabilized by hydrophobic entropic forces, van der Waals interactions and hydrogen bonding between cholesterol's hydroxyl groups and SM (58). The lipid domains form bilayers in the liquid ordered (Lo) phase, even though coexistence of Lo and Ld in these has been observed. Some multidrug resistant (MDR) cancer cell lines promote colocalization of cholesterol with other phospholipids (PC, PE, and others) and transmembrane proteins, favoring increased lipid packing and decreased permeability. This leads to greater membrane rigidity affecting the uptake and penetration of chemotherapeutic drugs in these cells (29, 43, 59–61).

1.2.3. Mechanisms of action for antibacterial and anticancer activities

Most experiments on the molecular mechanisms of membrane permeation/disruption have focused on the interaction of cationic peptides with model membrane systems. This platform has been used for the study of both AMPs and ACPs (16, 62–66). Therefore, for the purpose of being concise in this thesis, the following description of mechanisms is relevant for both AMPs and ACPs unless otherwise indicated (i.e. particular differences between the two will be highlighted when required). Complementary studies with whole microbial cells have also been employed for investigating the modes of action by using mostly microscopy, membrane potential sensitive dyes and fluorescently labeled peptides. However, the range of techniques available for using whole cells can be limited or be dependent on instrumental limitations (8, 67, 68).

The studies indicate that all AMPs/ACPs interact with membranes and divide peptides generally into two mechanistic groups: membranolytic (barrel stave, toroidal, carpet and micellar aggregate models) and non-membranolytic (when peptides have intracellular targets) (13, 64). AMPs/ACPs can exert their membranolytic function through several mechanisms of action, either by forming pores or through a non-pore former effect (Figure 1.4). Independent of their activity, AMPs must be adsorbed into the membrane, undergo a conformational change, and reach a certain threshold concentration to disrupt the membrane integrity (Figure 1.4). While many experimental observations are well described by one or more of the classical pore-forming models, no single mechanism can be defined for all peptides. Models for AMPs/ACPs membrane permeabilization have been proposed, however there is no universal consensus among researchers on this topic. (8, 26, 69).

The mechanisms of disruption of AMPs/ACPs depend on several parameters that affect their biological activity, such as the peptide charge, sequence, length, and secondary structure, amphipathicity, hydrophobicity, lipid membrane composition and peptide concentration. The peptide charge varies usually from +2 to +9 at neutral pH and charged residues are displayed on the hydrophilic face. The cationicity allows the initial adsorption *via* electrostatic interactions with the negatively charged phospholipids headgroups (Figure 1.4). The peptides accumulate locally and reach a threshold concentration (minimum peptide concentration required at the membrane

surface to perform the biological effects). The threshold concentration is usually denoted in experimental procedures as peptide-to-lipid ratio (P/L) (29). Other parameters can influence the threshold concentration, including the propensity of peptide self-assembly, and ability to partition, among others. However, in eukaryotic cells membrane fluidity and composition can play greater roles (57, 62, 70, 71), as illustrated in Figure 1.4.

A conformational change then occurs at the interface (Figure 1.5), usually a transition from an unstructured chain to an amphiphilic secondary structure, enhancing peptide insertion and membrane permeability. Hydrophobic amino acid residues permit hydrophobic interactions of AMPs/ACPs with the acyl chains facilitating the disruption or penetration to finally exert their membranolytic antibacterial or anticancer effect. Hydrophobic interactions play a major role in this step as the peptides must penetrate or be internalized in the lipid bilayer core. Whether it is for forming a pore, translocation to the cytoplasm or for a non-disruptive lipid-clustering effect, the length and hydrophobicity level of the peptides are crucial (8, 26, 72).

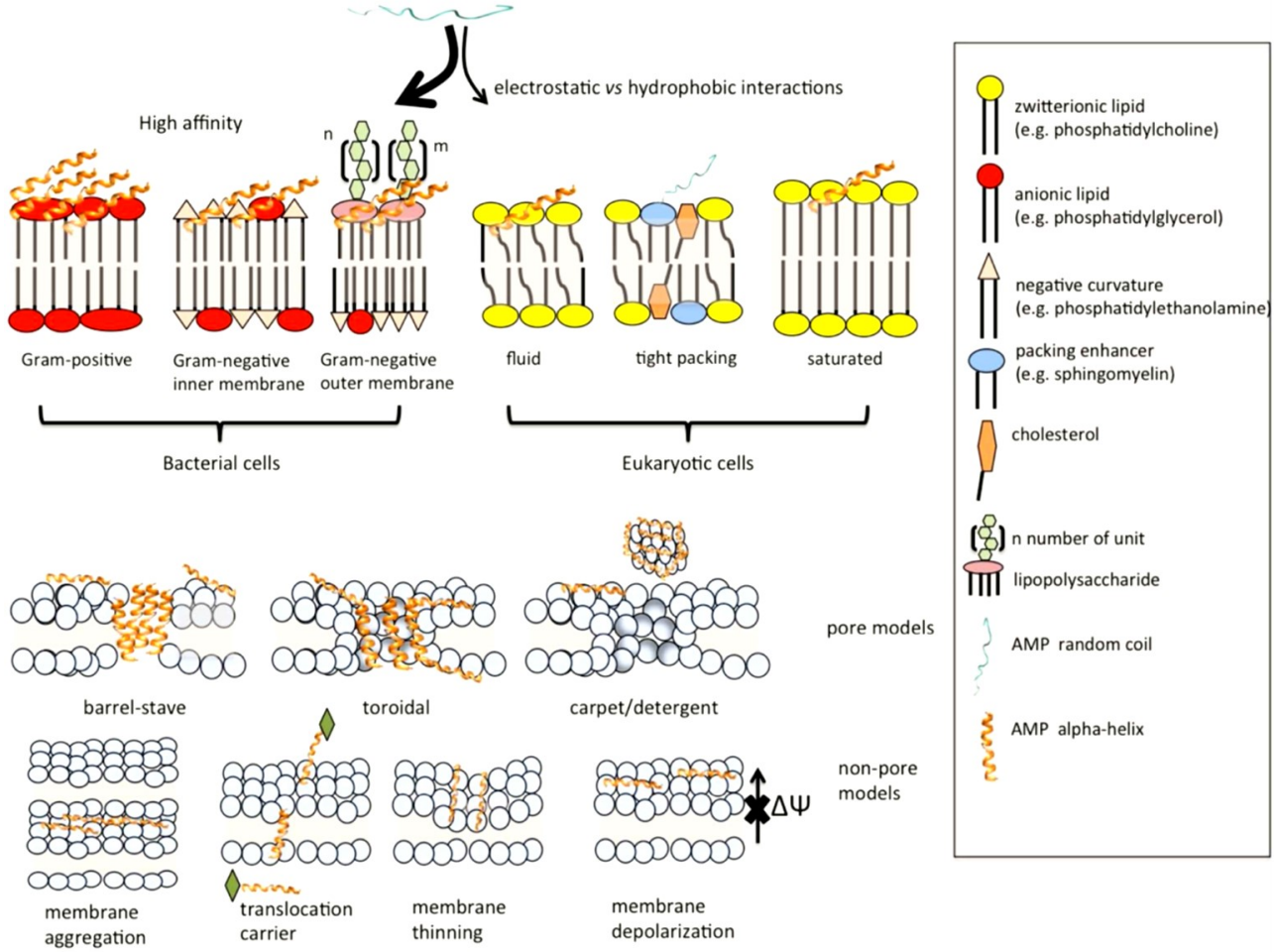

Figure 1.5. Interaction of AMPs/ACPs with biological membranes and mechanisms of disruption. Unstructured AMPs/ACPs are selective to negatively charged membranes. Upon interaction, they adopt a defined secondary structure to disrupt the bilayer. Proposed pore-forming and non-pore forming modes of action are shown. The mechanism of action is dependent on the peptide and the lipid membrane composition. Membrane perturbation varies with peptide concentration, temperature, and pH (73)**.**

Depending on both the specific AMPs/ACPs and the peptide concentration, the mode of action can be described by one or more models (Figure 1.5). Some AMPs/ACPs cause stable membrane pores (barrel stave or toroidal pore models), membrane thinning (molecular electroporation or sinking rafts models) or micellization in a detergent-like way (carpet/detergent model).

In the barrel-stave model, amphipathic peptide helices can form a pore in the membrane with the lipophilic side of the peptide facing the hydrophobic core of the membrane bilayer and the hydrophilic portion lining the pore. This resembles a barrel composed of helical peptides as the staves (Figure 1.5). This mechanism of action is primarily displayed by highly hydrophobic peptides. The barrel-stave model cannot account for cytolytic activity by AMPs/ACPs that are <23 amino acids since they are not long enough to span the lipid bilayer, thus demanding quite specific peptide properties that only occurs for a few peptides (74).

The toroidal pore model describes that AMPs/ACPs are inserted in lipid bilayer bending the outer leaflet through the pore so that the lumen of the pore is lined by both the inserted peptides and the lipid head groups. The model can be formed by a much greater variety of peptides compared to the barrel stave model, and it has been suggested that some AMPs/ACPs acting by this mechanism of action may cross through the membrane and act on intracellular targets (64).

The carpet/detergent model comprises AMPs/ACPs that bind to anionic cell membrane components and become aligned in parallel to the surface of the cells, thereby creating a carpet-like appearance. When the threshold concentration of the peptide is reached, the membrane will start to destabilize and collapse due to the curvature stress and internal osmotic pressure, ultimately leading to cellular lysis. In this model the peptides never enter into the hydrophobic core of the cellular membrane (29).

In addition to the membranolytic mechanisms of action, there are also several non-membranolytic effects exerted by AMPs/ACPs. In the molecular electroporation model pores can form in

membranes with AMPs/ACPs under the influence of an external electric field. The sinking raft model describes that due to an imbalance of a mass ratio between AMPs/ACPs binding to a particular lipid domain and an increase in membrane curvature, peptide translocation occurs (63, 75–78).

The focus herein is on modes of action that have a membrane-directed effect; the action of AMPs/ACPs on intracellular targets is beyond the scope of this work.

1.2.4. Structure-activity relationship (SAR) of AMPs/ACPs

AMPs/ACPs possess membrane lytic activities naturally designed to target the cellular membrane of pathogens. As AMPs/ACPs composition is so diverse and they often show specificity against particular pathogens, structure-activity relationship studies are addressed to identify or to predict the molecular features that allow specific biological functions. The structural and functional diversity of AMPs/ACPs makes it difficult to summarize the vast number of SAR studies conducted to date and this section will only provide an overview. Section 1.3 contains a deeper analysis for the peptides of interest.

Amino acid sequence, peptide secondary structure (or conformation), charge, hydrophobicity, amphipathicity or polar angle, and tacticity are among the main parameters contributing to the activity of a bioactive peptide. The activity and selectivity of bioactive peptides is dependent on a fragile interplay of these parameters. Commonly, the modification of one parameter renders a variation of the others in compensation (25, 79–82). Membrane fluidity, as an environmental parameter, is also deemed a major factor modulating the activity of cytolytic peptides. Cholesterol and other sterols can increase the lipid packing and induce higher order in cell membranes. Thus, binding and insertion of AMPs in cholesterol-rich domains is usually decreased (25).

According to the peptide secondary structure, most membranolytic activity has been attributed to α-helical peptides due to higher propensity to form pores (83). β-sheet forming AMPs/ACPs can also contain minor helical segments (80). However, many disrupting effects have been described for peptides adopting β-sheets. Linearization of the β-sheet tachyplesin rendered a reduced dye release from model membranes, and a reduction on the antimicrobial and antiviral activities (80).

In general, cytolytic peptides change from a random coil in solution to either α-helices or β-sheets secondary structures upon interaction with lipid membranes. The structural transition contributes on the stabilization of the rigid peptide backbone (N−Cα−CO) by hydrogen bonding between the amino (donor) and carbonyl (acceptor) groups. More stable peptide backbones increase the likelihood of a structural integrity within the bilayer core while creating membrane defects by disrupting the surface tension. Hence, the membranolytic activity can be affected by the peptide secondary structure formed, as the extent of the conformational change influences the backbone rigidity (73).

The distributions and placement of cationic residues also plays an important role as revealed by studies in peptide analogs with identical composition. One analog with the cationic groups clustered along one face of the secondary structure length (α/β-peptide I), and the other with the positive charges around the long axis of the helical peptide (α/β-peptide II), were assessed for their activity in bacterial membranes (84). The latter was better at separating charged lipids in the membrane environment compared to the α/β-peptide I, and it was more effective against *E. coli* (Gram-negative), but they both were equally toxic against *Bacillus subtilis* (another Gram-negative). The authors attributed the difference to a less rigid peptide structure on the α/β-peptide II when bound to membranes, and suggest that the amphipathic variant (α/β-peptide I) is less adaptable to targeting charged phospholipids in the membrane (84). These results differ from the more general remarks mentioned above.

A balanced hydrophobicity content is also required. When hydrophobicity is too low, AMPs/ACPs may present lower affinity to the membrane, but self-association (and even precipitation) may occur if hydrophobicity is too high (29). Natural α-helical forming peptides derived from frogs and toxins from bee and scorpion venom have been compared. These varied between 13 and 26 amino acids, with net charges between +1 to +8, and hydrophobicities from 51% to 68. NMR results showed that aurein and citropin had more rigid secondary structure whereas maculatin and caerin had bent structures. The authors identified that the prediction of bactericidal or hemolytic activities based on the hydrophobicity, charge, and secondary structure of AMPs and toxins was inconclusive, but that peptide activity is affected by both the thickness and fluidity of the membrane (73). Larger and less heterogeneous peptide pools should be considered for analyzing structure-function relationships, accounting for the least number of variables at a time.

Peptides that translocate through the membrane without compromising its integrity, also known as cell-penetrating peptides (CPPs), do not require specific secondary structures for translocating across the lipid bilayer. Most CPPs have a random coil conformation but it is known that peptides adopting either random coil, α-helical, and β-sheet structures can traverse membranes (73, 85). Though, α-helical or β-sheet CPPs need high content of anionic lipids in the membrane as they stay unstructured in neutral vesicles or in aqueous solutions. Moreover, it has been reported that peptide penetration may improve with higher helicity (86). Usually, random coil CPPs possess shorter primary sequences (<30 residues) and higher net charge than those with defined secondary structures. Many CPPs are rich in Lys, Arg or both. This common feature among CPPs can cause that their interaction with anionic lipid membranes be governed by electrostatic interactions. The order and number of the amino acids in the peptide sequence have been considered crucial for transport in cellular uptake studies. Nevertheless, many CPPs change their conformation from random to defined secondary structures upon interaction with polysaccharides or lipids, similarly to other AMPs (73). For this reason, along with the absence of distinctively defining features, and the fact that membrane translocation mechanisms of CPPs are yet unclear, the distinction between AMPs and CPPs remains ambiguous.

Cyclic peptides have also been proposed as a promising therapeutical alternative, with cell membrane-directed activities. Cyclotides have been used as structural frameworks and they can have applications on delivering other AMPs into cells, hence having also intracellular targets (87). Cyclotides are plant-derived peptides with a typical head-to-tail macrocyclic structure and three disulfide bonds derived from six conserved Cys residues forming a cyclic cystine knot arrangement. This topology grants them with resistance to chemical, thermal, or proteolytic degradation. Anti-HIV, antimicrobial, insecticidal, anticancer (*in vitro*) and anthelmintic activities have been reported for cyclotides (88). Linearization of the peptide backbone have caused the loss of anti-HIV, hemolytic, or insecticidal effects and membrane binding properties, highlighting the role of molecular topology in these activities (89). Cyclotides action is mostly specific to membranes containing phospholipids with PE headgroups. They can act as CPPs or lead to membrane disruption *via* a pore-forming mechanism after reaching the threshold concentration. However, it is been found that peptides targeting PE groups, such as cyclotides, cause hemolysis and cannot discriminate cancerous from non-cancerous cells or model membranes (88–92).

Experiments conducted with the D-enantiomer of cyclotide kB1 revealed lower hemolytic level due to reduced binding affinity for PE-containing membranes compared to the L-enantiomer. Noticeably, the D-kB1 cyclotide preserved the other bioactivities. This is an indication that the peptide activity is influenced by the chiral environment in phospholipid bilayers (89).

Studies for identifying molecular predictors of anticancer peptides have shown that the amino acid compositions were a distinct feature to distinguish anticancer peptides and non-anticancer peptides (93, 94). Results from benchmark datasets of ACPs and non-ACPs indicated that the amino acid compositions were different and that the most frequent lengths in anticancer peptides (~80%) were between 10-20 amino acids. One of these studies indicated that combined, the local amino acid compositions, variance of the average chemical shifts, and the reduced amino acid composition, were more effective for the prediction of anticancer peptides (93). The other study identified the pseudo amino acid composition accounting for local domains as the best predictive feature (94). Regarding the amino acid compositions, both studies found the prevalence of Ile, Lys and Gly as relevant for ACPs compared to non-ACPs using different approaches on the same dataset from the APD2 database (93, 94). It is interesting to notice that the abundance of Lys prevailed over Arg as the dominant cationic amino acid in ACPs whereas it was shown that Arginine's guanidino groups may increase the action of antimicrobial peptidomimetics against bacterial membranes (95).

In silico, the parameters with greatest importance for ACP classification and distinguishing them from inactive peptides were identified as those accounting for the frequency of amino acids with hydrogen-bond donor and acceptor groups. Moreover, global hydrophobicity, peptide hydrophobic moment (μ_H), peptide length, and the frequency of positively charged amino acid pairs separated by one residue were also important predictors for the classification of ACPs (79). Subsequent experiment-guided simulated molecular evolution showed that a moderate reduction of both the hydrophobic moment and the net positive charge (+7) rendered the more selective anticancer peptides in their generations (79). This increase in selectivity of the membranolytic ACPs resulted in a reduced anticancer activity, in agreement with other reports (62, 79, 96).

Arrangements of peptides of different lengths containing D, L and mixed D and L amino acid residues have been studied through an array of biological assays and biophysical techniques (97, 98). It is demonstrated that systemically intratumor injections of a short 15-mer D,L-amino acid

peptide (D-K_6L_9;LK*L*LK*K*L*L**K*KLL*K*LL-NH2, where italic letters are D-amino acids) selectively suppressed growth of human primary and metastatic tumors while being innocuous to neighbor normal cells. Studies on the mode of action suggested the peptide acts *via* a membrane-depolarizing lytic mechanism targeted to phosphatidylserine in the cellular membrane (99, 100). A consensus remains to be defined on whether distinct mechanisms of action for AMPs/ACPs take place in bacterial and cancer cells membranes.

1.3. GL13K structure and activity

GL13K is a thirteen-amino acid (GKIIKLKASLKLL-NH2) AMP with a +5 net charge at physiological pH, designed by introducing three lysine residues (positions 2, 5, and 11) in a peptide sequence derived from the human parotid secretory protein (101, 102). The four Lys residues and an amidated C-terminus provide the cationic charge, while two Ile and four Leu residues provide the hydrophobicity for the amphipathic amino acid distribution (Figure 1.6). C-terminal amidation of AMPs is a strategy that has been used to increase antimicrobial activity and stability. Studies on synthetic peptides show that this amidation enhances interactions with the membranes by modifying the hydrophobic moment (103, 104). The additional Lys residues in GL13K eliminated the bacteria agglutinating activity of the original peptide sequence. After an Ala-scanning with substituted peptides, the substitution of the Lys residue in position 2 seems to have been the most influential in losing the agglutinating ability (101).

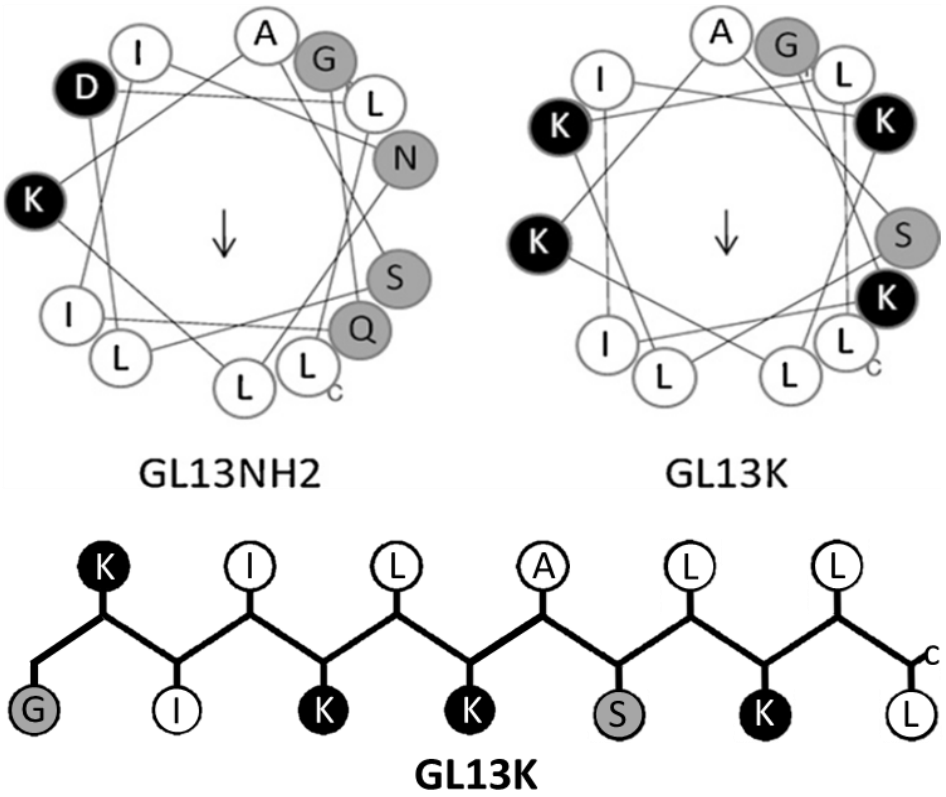

Figure 1.6. Helical wheel representation (top) of the original peptide sequence (GL13NH2) derived from the human parotid secretory protein and GL13K (101)**. β-strand representation of GL13K is depicted at the bottom. Open circles: hydrophobic residues. Black circles: charged residues; gray circles: hydrophilic residues and glycine. Glycine is the N-terminal residue, and the amidated C-terminal leucine residues are labeled (c).**

GL13K shows broad-spectrum antimicrobial (Table 1.1) and antibiofilm activity at low minimum inhibitory concentrations (MICs), and displays immunomodulatory activity *via* inhibition of the secretion of the proinflammatory cytokine TNF-α. The leucine at position 6 was an essential determinant for the antibiofilm effect against *Pseudomonas aeruginosa* PAO1. GL13K also displays anti-LPS activity, which was dependent on the serine residue at position 9. Replacing the Ser with Ala eliminated LPS binding, suggesting that the hydroxyl group in serine was critical for LPS-inhibitory activity. In addition, GL13K protects mice from LPS-induced sepsis and it is not hemotoxic in human red blood cells at high concentrations (~700 μM), making it a great candidate for therapeutic applications (101, 102, 105). An initial approach using a GL13K-biofunctionalized titanium surface coating proved to be successful as it conferred bactericidal activity, cytocompatibility and reduced bacterial biofilm growth in dental care applications (106).

It is therefore interesting to investigate how a peptide with biomedical potential like GL13K performs its biological function. A clearer notion of its mode of action can potentially lead to the design of more potent peptide-based antibiotics.

On this basis, biophysical studies in our group have been directed to explain GL13K peptides mechanism of disruption in bacteria using model membranes. The role of electrostatic and hydrophobic interactions was evaluated on the activity and specificity of GL13K against single-lipid negatively charged and zwitterionic liposomes (107). The study showed a strong binding affinity and lytic activity in presence of anionic dioleoyl-PG (DOPG, one of the phospholipids present in bacterial cell walls) liposomes using isothermal titration calorimetry (ITC) and CF (carboxyfluorescein) release. This occurred even at high salt concentrations, while there was no significant binding to zwitterionic dioleoyl-PC (DOPC) liposomes even in low salt conditions. This study suggested that the membranolytic effect of the peptide occurs by a carpet mechanism or by the formation of transient channels or both. In particular, the dye release experiments indicated that membrane disruption could be caused by peptide-induced micellization *via* lipid clustering or localized removal of phospholipids from the membrane (107).

Table 1.1.Minimum Inhibitory Concentrations (MIC) for antibacterial activity of GL13K enantiomers reported in the literature. The entries until the line represent Gram-negative bacteria, the rest are Gram-positives

Bacterial strains	L-GL13K		D-GL13K		References
	MIC (μg/mL)	MIC (μM)	MIC (μg/mL)	MIC (μM)	
P. aeruginosa PAO1	8	5.6			(101)
P. aeruginosa PAO1 Biofilms	100	70.2			(105)
P.aeruginosa Xen41	10.4	7.3	5.2	3.7	(108)
E. coli DH5-α	5	3.5			(101)
E. coli DH5-α incubated with 50% saliva	50	35.1			
Porphyromonas gingivalis W50	>100	>70.2			
Staphyloccocus aureus	41	28.8			(109)
S.aureus Xen36	83.3	58.5	2.6	1.8	(108)
S.aureus USA300 (MRSA)	>		5.2	3.7	
Vancomycin resistant *Streptococcus gordonii* DL1 (WT)	>200	>140	5	3.5	(110)
Vancomycin resistant *S. gordonii* DL1 *dltA*	11	7.7	4	2.8	
Vancomycin resistant *S. gordonii* DL1 *atlS*	63	44.2	4	2.8	
OG1RF *Enterococcus faecalis* (WT) resistant strain	>200	>140	13	9.1	
OG1RF (TX5427) *dltA* mutant	70	49.2	23	16.2	
OG1RF (TX5128) protease negative, autolysis impaired mutant (*gel*E$^-$, SprE$^-$)	>200	>140	11	7.7	
OG1RF *ebsG* mutant	>200	>140	7	4.9	
OG1RF::pMSP7551 mutant that overexpresses EbsG induced by nisin	>200	>140	10	7.0	
OG1RF::pMSP7551+nisin	>200	>140	11	7.7	
Vancomycin resistant *E. faecalis* V583	>200	>140	12	8.4	

>: implies higher than the maximum concentration tested in the assays.

In presence of anionic model membranes containing DOPG, GL13K adopts a β-sheet conformation (107). This is a conformational change required for its activity as an unfolded state is observed when GL13K is in solution or interacting with zwitterionic phospholipids (107). In

contrast, solid-state NMR studies showed that ^{2}H- and ^{15}N-labelled-GL13K has a low propensity to fold into α-helices between Lys residues 5-11 in zwitterionic dodecylphosphocholine (DPC) micelles (109). The binding concentrations were too low to be detected by circular dichroism. However, it confirmed the preferential folding into β-sheets in aligned anionic bicelles and liposomes containing ~25% of PG. Interestingly, GL13K displayed predominantly random-coils in presence of ~25% of anionic palmitoyl-PS vesicles (109).

More recently, the GL13K interfacial activity and its propensity to form amyloid fibrils has been investigated. Structural studies based on spectroscopic and X-ray scattering techniques demonstrated that GL13K forms preferentially antiparallel crystalline β-sheets at the air/buffer interface (111). The correlation lengths of the β-sheets were found to be greater at the interface with anionic lipid monolayers than those observed with zwitterionic phospholipids, or in absence of lipids. Therefore, electrostatic interactions between the lysine side chains and the phosphatidyl-glycerol headgroups stabilize GL13K's supramolecular organization, as observed by Youssef and DeWolf (112). The peptide does not self-assemble into fibrils at physiological pH nor in absence of anionic lipids, despite the crystallinity of its secondary structure. The authors suggest that fibril formation is likely prevented by the presence of a Lys residue on GL13K's hydrophobic face and the net charge (111). GL13K also inserts into both the headgroup and tail regions of phospholipid monolayers with methyl-branched lipid chains as a Gram-negative bacterial membrane model. In this model, lipid branching with a bulkier hydrophobic nature the did not prevent peptide penetration into the acyl chains (112).

Despite this work on deciphering the mode of action of GL13K, a fully descriptive and more comprehensive understanding of the mechanism of action for GL13K activity is yet to be defined and many open questions remain. For example, GL13K appears to form crystalline β-sheets only in one direction while other peptides have shown crystallinity on both the short and long axes of the strands. Previous results do not conclusively prove a direct correlation between the peptide crystallinity and activity as it is more crystalline when trapped among lipid headgroups (less insertion), while it is said the peptide is most active when it inserts into the acyl tail region (112). Despite this, GL13K can still effectively lyse membranes and inserts in both the headgroup and tail regions of branched-phospholipids monolayers.

Recent studies demonstrate that amphipathic peptides whose length is too short to span the hydrophobic lipid bilayer core do not form transmembrane pores. Such is the case of peptides shorter than the membrane thickness. Their interfacial behaviour is therefore determinant for the disruptive effect on bacterial or cancer membranes and other mechanisms of action are in place, depending of course, on phospholipid composition and peptide sequence (63, 113).

The biophysical studies on GL13K so far have been limited to single or binary phospholipid systems (107, 109, 111, 112). Although, model membranes are not full compositional representatives of the complexity of bacterial or eukaryotic membranes, more complex phospholipid compositions can better resemble the real membrane of cells. Ternary and quaternary lipid mixtures could potentially induce a different interaction behaviour with AMPs/ACPs, compared to simpler models. Packing and condensing effects derived from more complex mixtures could also affect the interaction, affinity of GL13K with the target membrane, as well as the penetration.

Some research groups have previously studied the interaction of AMPs with more complex bacterial membrane models including three and four phospholipid compositions and, even other components of bacterial cell walls such as LPS and LTA (28, 33, 114–119). Therefore, in this research we will build ternary model membranes that better represent the ratios of zwitterionic and negatively charged phospholipids of Gram-positive and Gram-negative bacterial membranes. Other mixtures using four or five phospholipids will also be used to mimic eukaryotic membranes to contrast.

1.3.1. GL13K enantiomers and the role of chirality in peptide activity

It is widely known that secreted proteases can cleavage unmodified AMPs/ACPs and mitigate their antibiotic effect (20, 23, 120). Substitution of L-amino acids with analogous D-amino acids has been employed in the rational design of peptide sequences to avoid or minimize proteolytic degradation of AMPs. The presence of D-amino acids improves peptide post-translational stability without affecting the biological function. D-enantiomers of peptides retain their antimicrobial or anticancer activity because the interactions between AMPs/ACPs and membranes are independent

of specific receptors (98, 121–123). The latter highlights the role of peptide chirality in peptide-based antimicrobials and as a new research niche.

Studies that have used all D-enantiomer versions of natural or synthetic ACPs and AMPs have reported enhanced bactericidal and anticancer activities showing for both significantly lower MICs and IC_{50} (concentration that results in 50% of dead cells compared to untreated controls), respectively (98, 100, 121, 123). These studies also demonstrated the resistance of D-enantiomers to be proteolytically degraded, while not toxic to normal cells. Preliminary biophysical approaches were included in some to try to explain the better activity of D-peptides, however in most cases it has been credited to the lack of affinity of proteases for D amino acid residues.

Interestingly, a recent review collected data from various studies and compared the bactericidal activity for natural AMPs and their all-D enantiomers for the first time. Based on their comparison, the authors ruled out the influence of chirality on the activity (124). Even though they mentioned that exceptions exist, these were attributed to potential mechanisms of action that do not involve a membranolytic effect. More comprehensive data reviews on peptide chirality are necessary along with experimental approaches that would allow clarifying this issue. Debate remains as to whether all-D enantiomers have enhanced activities compared to their natural versions.

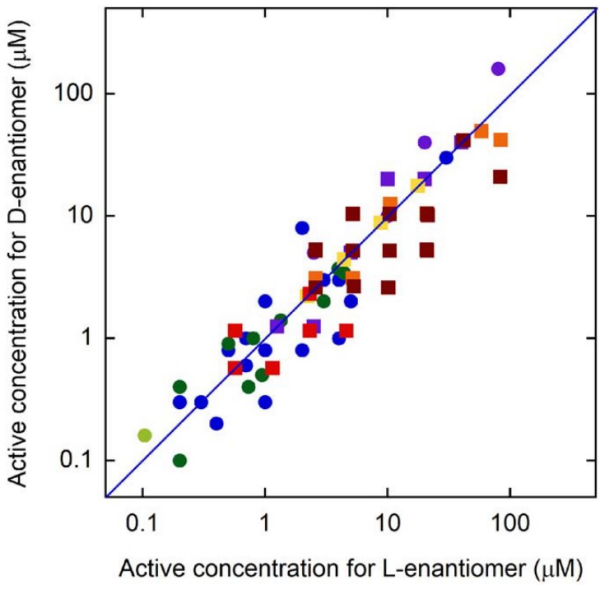

Figure 1.7. Comparison from literature data review of the antibacterial activity between D- and L-enantiomeric peptides in terms of Minimum bactericidal concentration (circles) and MIC values (squares). Graph taken from Savini *et al.* (124)**.**

The first report of differential activity of GL13K peptides came when Hirt *et al.* (2013) were assessing the stability of GL13K (hereafter referred to as L-GL13K) in *Pseudomonas aeruginosa* to evaluate if it was inactivated by soluble factors. A D-enantiomer (hereafter referred to as D-GL13K) was then synthetized (105). Refer to the structure in Figure 1.8. The all-D-amino-acid version of GL13K was not susceptible to protease degradation and remained active in both heat-inactivated and sterile filtered *P. aeruginosa* culture supernatant, while L-GL13K lost activity in sterile-filtered medium. The study also confirmed that the degradation of L-GL13K occurred due to the presence of metalloproteases produced by *P.aeruginosa* (105, 120). D-GL13K has shown to be more effective because is able to avoid proteolysis in *P. aeruginosa*, *Enterococcus faecalis* and *Streptococcus gordonii,* showing lower MICs (Table 1.1) and evading antimicrobial resistance mechanisms in the last two (105, 122)

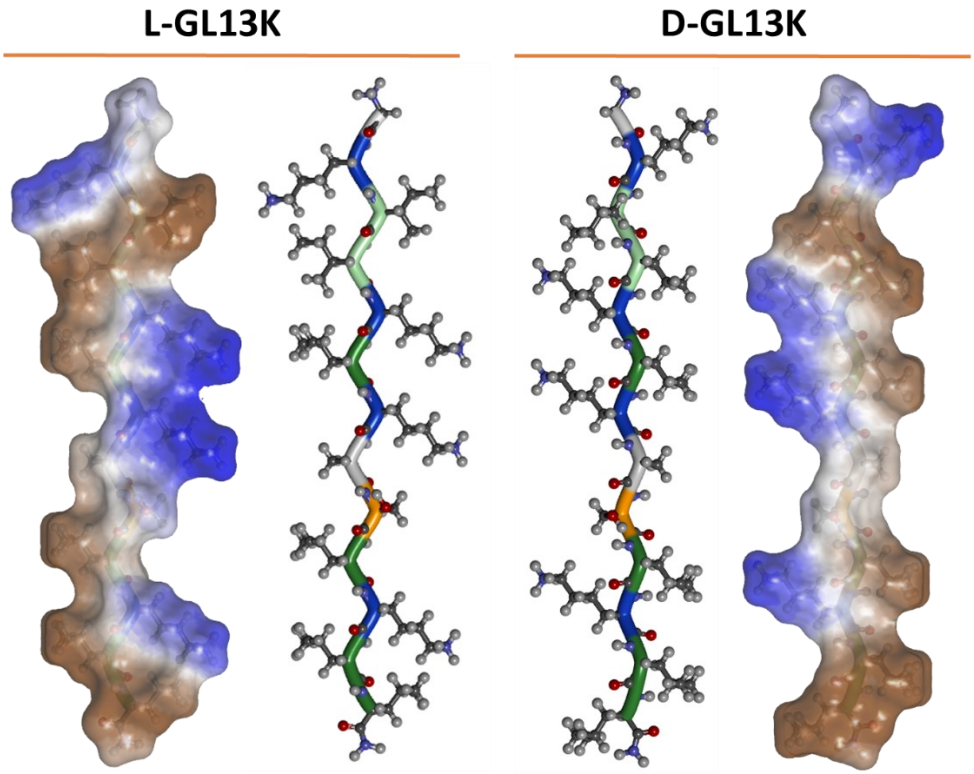

Figure 1.8. Surface representation of the GL28K peptide as β-strand constructed with Accelrys Discovery Studio software (v4.1). The backbone is colored by residue (centered structures). The hydrophobic surface is shown in brown, and the polar moieties in blue.

Recent results suggest that the difference in activity between L- and D- enantiomers is not caused solely by protease-resistance. Antibacterial assays with a protease-negative strain of *E. faecalis* (TX5128) showed that L-GL13K has lower activity than D-GL13K in absence of proteases (Table 1.1). Thus, other modifications may be occurring in Gram-positive bacteria to resist the action of D-AMPs (122).

D-alanylation of teichoic and lipoteichoic acids is another mechanism of resistance of Gram-positive bacteria against cationic AMPs. Bacteria can upregulate their *dlt*-operon to reduce negative surface charge of the cell wall by, for example, forming zwitterionic alanyl-PG (APG) (31, 122). Mutants that express the D-alanylation gene (*dltA*) are then less sensitive to AMPs.

The D-enantiomer was highly effective against both, mutants and WT of planktonic bacteria and biofilms of *S. gordonii* and *E. faecalis* (122). In contrast, L-GL13K was effective only against the *dltA* (Table 1.1). Differential antibiofilm activity was evaluated and L-GL13K was ineffective against wild-type *E. faecalis* biofilms, while the D-GL13K was highly effective against both, WT and *dltA* strains. The D-enantiomer also overcame the resistance mechanisms of the vancomycin resistant strain *E. faecalis* V583 and reduced considerably its biofilm counting (122).

Repetitive treatment of antibiotic resistant *S. gordonii* wild type (WT) and *dltA* mutant bacteria with sub-lethal concentrations of D-GL13K during days did not affect the MIC. The same procedure with L-GL13K caused a 6-fold and 16-fold increase of the MIC in those WT and the *dltA* mutant bacteria, respectively. This approach was used against *E. faecalis* WT and *dltA* mutant (TX5427) showing that D-GL13K did not substantially increase the MIC versus both strains. In contrast, L-GL13K increased by 8-fold the MIC vs the *dltA* mutant. Therefore, the *dltA* mutants were able to regain resistance to L-GL13K but not to D-GL13K (122). The latter highlights the relevance of the D-enantiomer of GL13K for potential clinical applications. A peptide that is not affected by the D-alanylation status of bacterial membranes proves its effectiveness in more challenging infective conditions.

Despite the tremendous potential of GL13K peptides, D-GL13K particularly, no studies have yet been addressed to their anticancer ability. This is tempting considering that of all peptides in the APD database, only 187 so far present both anticancer and antibacterial activities (of which 11 have the same length as GL13K with a positive net charge of 1 to 5). Moreover, the D-enantiomer

has not been studied using model membranes. Accumulated evidence on their differential activity suggests that D- and L-GL13K may have distinct mechanisms of membrane disruption. Thus, investigating the mode of action of these peptides and the role of chirality on its activity using complex model membranes is very appealing. This approach could potentially explain D-GL13K's enhanced potency relying only on the structural bases of the peptide and phospholipids (without considering the presence of proteases). On these bases, this research will build up.

1.3.2. New peptidomimetics

It is reported that SVS-1 (KVKVKVKVP$_D$P$_L$TKVKVKVK) is the first example of an anticancer β-hairpin that is dependent on membrane-induced folding for its action (123). This peptide and its D-enantiomer (^{D}SVS-1) show promising anticancer activity against several cancer cell lines at low IC_{50}, ranging from ~3-8 μM. However, there are no reports of their antibacterial action.

According to Sinthuvanich et al. design of SVS-1, the D-enantiomer of proline creates the β-turn in the secondary structure of the peptide. The SVS-1 peptide contains a D-Pro/L-Pro (P$_D$P$_L$) motif that folds into a structured Type II′ β-turn (123, 125). The alternating Val and Lys residues permit the amphiphilic structure and facilitate the aggregation and electrostatic interactions on the surface of anionic membranes. Similarly to GL13K (107), the SVS-1 peptide remains unfolded in solution or in presence of zwitterionic model membranes due to the positively charged Lysine residues. However, the turn is structured because of the D-Pro and L-Pro isomers. SVS-1 is hypothesized to fold once it binds to a charged membrane due to complementary electrostatic interactions (123, 126).

Thus, the VP$_D$PT turn motif could potentially be used between two peptides GL13K to increase the partition into the bacterial, cancerous, or model membranes. This could guarantee a faster or more uniform peptide lining on the target membrane. The same approach could follow for D-GL13K but using a proline motif of the opposite chirality P$_L$P$_D$. Following this line of analysis, the GL28K peptide was designed in our lab (GKIIKLKASLKLVP$_{(D)}$-PTKIIKLKASLKLL-amidated) as a promising potential antibacterial and anticancer peptide.

1.4. Objectives

Most biophysical studies have relied on single or two component model membranes to address their research question. This work comprises a detailed biophysical study on how the GL13K peptides interact with complex multicomponent models.

Two model membranes mimicking Gram-positive and Gram-negative bacterial membranes were used in liposomes and monolayers to determine if the membrane composition affects the mode of action and selectivity of GL13K in bacteria. Based on previous studies and the estimated lipid compositions *in vivo*, we chose the phospholipids DOPE, DOPG and CL at two different molar ratios as suitable model membrane systems, (28, 33, 114–118). Also, preliminary studies on the activity of the new peptide analog GL28K are performed as a proof of concept.

Additionally, we undertook to identify if GL13K enantiomers possess anticancer activity by screening the H1299 lung cancer cell line, using human fibroblasts as a toxicity control. The altered morphology and phospholipid distribution of cancer cells that express some negatively charged phospholipids in the outer membrane leaflet can be exploited here to evaluate their anticancer activity. To understand/assess how mechanistically different the peptides interact with eukaryotic cells with regard to bacteria we also included two model membranes mimicking the composition of erythrocytes and a consensus cancer cell membrane. To that end we utilized DOPC, DOPE, SM, Chol and DOPS lipids that are present in different proportions in mammalian cell membranes (42, 50, 52, 53, 127–130).

The role of chirality was investigated as well on the interfacial activity, disruptive effect, and preferential interaction of D- and L-GL13K enantiomers with all the models. The biophysical approach using model membranes might allow to elucidate if L-GL13K lower effectiveness compared to D-GL13K is limited only by the susceptibility to proteolysis, or if the chirality of the peptides can also affect their interaction with the membrane lipids in a protease free environment. Our results aim to provide a comprehensive insight on the mode the GL13K peptides interact with bacterial and eukaryotic membranes, and to do a preliminary assessment of their new potential for therapeutic applications.

Chapter 2. **Materials and experimental techniques**

2.1. Materials

2.1.1. Phospholipids and peptides

The following phospholipids were bought from Avanti Polar Lipids Inc.: 1,2-dioleoyl-sn-glycero-3-phosphoethanolamine (DOPE), 1,2-dioleoyl-sn-glycero-3-phospho-(1'-rac-glycerol) (DOPG), 1',3'-bis[1,2-dioleoyl-sn-glycero-3-phospho]-glycerol (Cardiolipin) 18:1, 1,2-dioleoyl-sn-glycero-3-phosphocholine (DOPC), 1,2-dioleoyl-sn-glycero-3-phospho-L-Serine (DOPS) 18:1 and Sphingomyelin from porcine brain (SM) 18:0. Cholesterol (Chol) 5-Cholesten-3β-ol was bought from SIGMA ALDRICH (Figure 2.1). The GL13K peptide enantiomers (GKIIKLKASLKLL-amidated) and GL28K (GKIIKLKASLKLVP$_{(D)}$-PTKIIKLKASLKLL-amidated) were ordered from Bio Basic Inc. (ON, Canada), all at ≥ 95% purity. L-GL13K refers to the sequence of natural amino acids while D-GL13K consists of dextrorotatory amino acid residues (except for Glycine). The peptide backbones were modeled as β-strands using Accelrys Discovery Studio software (v4.1) and PyMOL^{TM} (0.99rc6.).

2.2. Cell Culture and Cell Viability Assays

The lung cancer cell line H1299 (lung carcinoma) was cultured in RPMI-1640 medium supplemented with Cosmic calf serum (CCS). Triple negative breast cancer MDA-MB-231 (adenocarcinoma) and normal cell line from human foreskin fibroblasts HFF-1 were cultured in Dulbecco's modified Eagle's medium (DMEM) containing 10% (v/v) fetal bovine serum (FBS), 2 mM L-glutamine, 1 mM sodium pyruvate, 50 U/mL penicillin and 50 μg/mL streptomycin. All cell lines were provided by Dr. Alisa Piekny and her group. Cell cultures were maintained at 37 °C and 5% CO_2 in humidified incubators. The cell lines were plated in triplicate in the corresponding growth media at ~10 000 cells/100 μL/well, rendering monolayers of adherent cells after 12-24 hours of incubation. Peptide stocks were diluted in sterile PBS to treat the cells overnight with the same volume at final concentrations that ranged from 0.5 μM to 200 μM. Internal controls for a 100% cell viability (untreated cells) and 0% cell viability (treatment with 20% DMSO) were included.

The WST-8 Cell Proliferation Assay (Cayman Chemical, US) was employed to assess the anticancer activity of the peptides following manufacturer's indications. This is a quantitative colorimetric assay where cell survival is determined spectrophotometrically at 450 nm after 1-2 hours of adding the WST-8. The WST-8 reagent (2-(2-methoxy-4-nitrophenyl)-3-(4-nitrophenyl)-5-(2,4-disulfophenyl)-2H-tetrazolium) is reduced extracellularly by electron mediators of mitochondrial NADH forming a soluble formazan. Cell viability is proportional to the intensity of the orange color generated by WST-8-formazan formed in presence of the NADH release (131, 132). Absorbance readings at 450 nm were collected using the TECAN Infinite M200 plate reader. The IC_{50} was calculated from a Napoleon-Hill fit of the normalized data using GraphPad Prism software (V 5.03).

2.3. Model membranes

Four membrane models were used. DOPE/DOPG/Cardiolipin 75/20/5 (mol%) to mimic the phospholipid composition of Gram-positive and Gram-negative plasma/inner membranes, and DOPE/DOPG/Cardiolipin 15/80/5 to model the outer membrane of Gram-negative bacteria (28, 33, 114–118). To mimic eukaryotic cell membranes DOPC/DOPE/SM/Chol 25/25/37.5/12.5 (mol%) was used as a model for the lipid composition of erythrocytes (RBC), and DOPC/DOPE/SM/Chol/DOPS 20/20/30/10/20 as a cancer cell model membrane (42, 50, 52, 53, 127–130).

Table 2.1. Phospholipid composition of the model membranes utilized.

Model membranes	Phospholipids	Mol % ratios	Ratios
OM of Gram-negative bacteria	DOPE/DOPG$^-$/CL$^-$	75/20/5	15/4/1
PM of Gram-positives or IM of Gram-negatives	DOPE/DOPG$^-$/CL$^-$	15/80/5	3/16/1
RBC membrane	DOPC/DOPE/SM/Chol	25/25/37.5/12.5	2/2/3/1
Cancer cell membrane	DOPC/DOPE/SM/Chol/DOPS$^-$	20/20/30/10/20	2/2/3/1/2

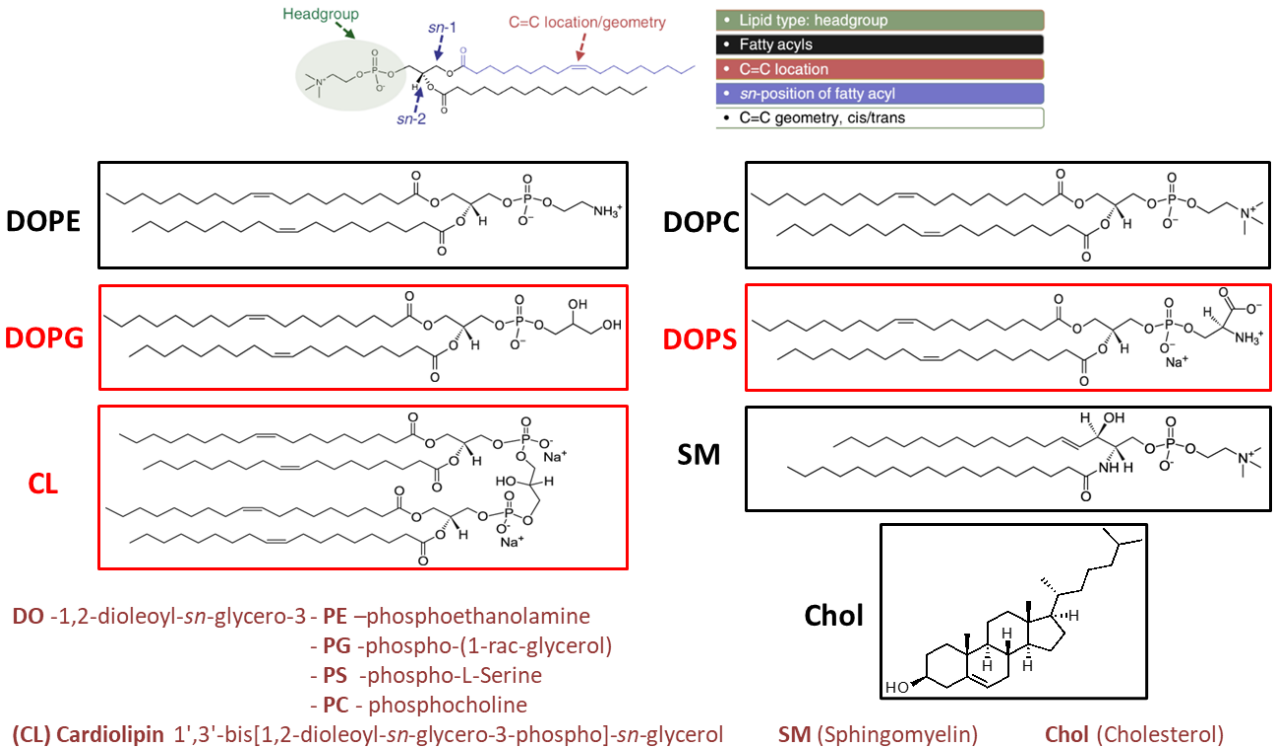

Figure 2.1. Structures of lipids used in bacterial and eukaryotic model membranes, and schematic (top) of phospholipid structural details (adapted from reference (133)**). All phospholipids are unsaturated. DOPE, DOPC and SM are zwitterionic while DOPG, CL and DOPS (colored) are negatively charged. Structures were retrieved from Avanti Lipids website and cholesterol was sketched in ChemDraw.**

2.4. Experimental techniques using monolayers

Monolayers of the model membranes were used to generate the isotherms and peptide insertion profiles and were characterized using x-ray scattering techniques and Polarization-Modulation Infrared Reflection Absorption Spectroscopy (PM-IRRAS). Circular Dichroism (CD), Carboxyfluorescein (CF) release assays and Localized Surface Plasmon Resonance (LSPR) were performed using Large Unilamellar Vesicles (LUVs) as bilayer model membranes. Each of the techniques will be described below.

2.4.1. Pressure-Area isotherms

Initial characterization of the surface behavior and organization of the phospholipids at the air/buffer interface were performed in a Langmuir film balance comprising a Teflon trough and two barriers used for a symmetrical lateral compression of the spread monolayers from an initial surface area of 80 cm^2. The lipids were dissolved in chloroform or chloroform/methanol 3/1 (v/v) solvent at concentrations of approximately 1 mM and spread on the PBS (pH 7.4) buffer subphase at ~22 °C temperature. After evaporation of the solvent, the lipid films were compressed at 5 cm^2/min, equivalent to approximately 8.3 - 9.4 $Å^2$/molecule/min in the case of the bacterial models, ~6.4 $Å^2$/molecule/min in the RBC model and ~9 $Å^2$/molecule/min in the cancer model. Upon compression, changes in surface pressure are monitored with a NIMA balance as the difference between the surface tension of the subphase in the absence and presence of the lipid film. Surface pressure-area isotherms can provide information on the phase transitions of pure phospholipids or lipid mixtures, which depends on the temperature or molecular characteristics of the lipids (134).

2.4.2. Surface-specific x-ray scattering techniques

The grazing incidence x-ray diffraction (GIXD) and x-ray reflectivity (XRR) experiments were done at beamline 15-ID-C ChemMatCARS at the Advanced Photon Source (APS) in the Argonne National Laboratory (Chicago, IL, USA). All experiments were performed at the air/buffer interface on a 57.8 cm^2 and 3.5 mm deep trough insert placed inside a sealed chamber. The phospholipids dissolved in chloroform were spread on PBS buffer subphase (pH 7.4) to reach a biologically relevant lateral surface pressure of 30 mN/m in the monolayer, which was monitored by a NIMA balance at 22 °C. The solvent evaporated and the chamber was flushed with helium to minimize the background scattering produced by oxygen. Once x-ray measurements of just the monolayer were taken, the GL13K peptides were injected (from a 4 mM stock solution) into the subphase at 5 μM, 10 μM or 20 μM final concentration. GIXD and XRR measurements were then carried out in presence of the peptides for comparison after ~20 minutes of equilibration (time needed to stabilize the surface pressure). Peptide injection occurs underneath the monolayer to resemble the approach of compounds coming from body fluids to the outer leaflet of cellular membranes (Figure 2.2).

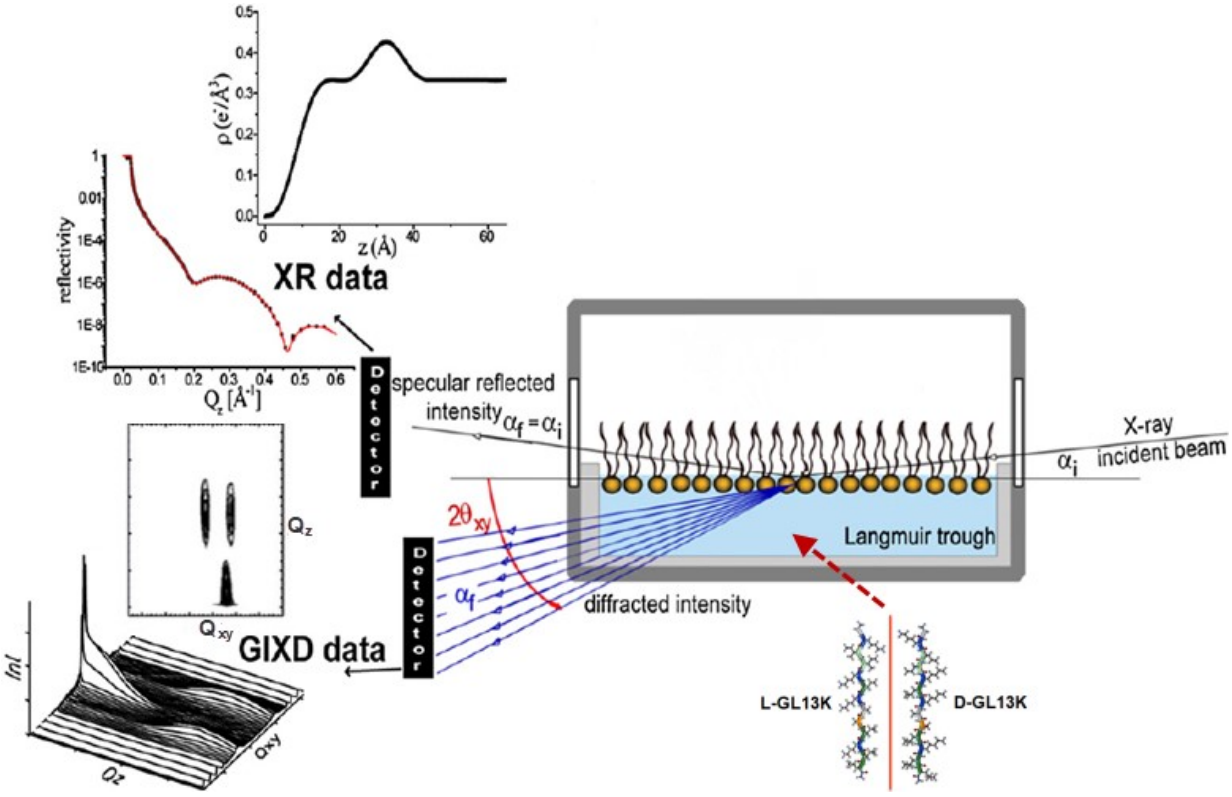

Figure 2.2. Schematic representation of the surface specific x-ray scattering techniques used for monolayers at the air/liquid interface. The peptides were injected under the monolayers. GIXD: grazing incidence x-ray diffraction, XR: x-ray reflectivity. Figure adapted from Stefaniu and Brezesinski (135)**.**

2.4.2.1. Grazing incidence x-ray diffraction (GIXD)

GIXD was performed to monitor the lateral organization of the peptides at the interface and their effect on the molecular packing of the lipid monolayers mimicking bacterial and eukaryotic membrane compositions. For GIXD experiments, the X-ray beam had a defined wavelength of 1.239 Å and struck the surface at an incident angle (α_i) of 0.09061°, lower than the critical angle (α_c) for total external reflection (Figure 2.2). The horizontal and vertical sizes produced a footprint of the beam of 20 µm by 7.6 cm and two sets of slits were used to minimize intense low-angle scattering. The incident beam was attenuated using absorbers to reduce radiation damage to the film and the Langmuir film balance was translated laterally to ensure measurements of non-radiated regions. The diffracted intensity was monitored using a 2D Swiss Light source PILATUS 100K detector set to single-photon counting mode, and it was measured as a function of vertical

scattering angle (α_f) and the horizontal scattering angle 2θ. GIXD measured data were represented as contour plots of the intensity as a function of both the in-plane (Q_{xy}) and the out-of-plane (Q_z) scattering vector components. The angular positions of the Bragg peaks (obtained by the integration of the scattering intensity over Q_z) in Q_{xy} yield the repeat distance spacing $d = 2\pi / Q_{xy}$ for the 2D structure.

$$d = 2\pi / Q_{xy} \qquad \text{Equation 1.}$$

The corrected full-width at half maximum ($FWHM_{xy}$) values of Bragg peaks were used as follows: $FWHM_{intr}(Q_{xy}) = [(FWHM_{meas})^2 - (FWHM_{resol})^2]^{\wedge 1/2}$, to calculate the in-plane coherence length L_{xy} with the Scherrer formula:

$$L_{xy} \approx 0.9 \times 2\pi / FWHM_{xy} \qquad \text{Equation 2.}$$

The FWHM of the Bragg rods ($FWHM_z$) can be used for estimating the thickness of the diffracting layer $L_z \approx 0.9 \times 2\pi / FWHM_z$ (95, 135, 136). Raw data were patched using software developed by scientist Wei Bu from the beamline at APS. The in-plane Bragg peaks and the out-of-plane Bragg rods in GIXD data were fit with Lorentzian and Gaussian functions respectively in OriginPro 2017 (OriginLab Corp. MA, USA).

2.4.2.2. X-ray reflectivity (XRR)

XRR provides information about the thickness and the vertical electron density gradient of a monolayer (Figure 2.2). The geometry of this technique involves that the X-ray incident angle matches the vertical scattering angle $\alpha_i = \alpha_f$ (135, 137). The measurements for XRR intensities were performed at Q_z angles that range from 0.01 $Å^{-1}$ to 0.7 $Å^{-1}$. The raw experimental intensities were analyzed and normalized using Fresnel reflectivity with software developed by APS scientist Wei Bu, which allows modelling the data to further generate the electron density profiles. The normalized reflectivity data are laterally averaged over both the ordered and disordered regions of the footprint covered by the beam along the normal to the monolayer surface. The XRR data were fit to slabs or box models that describe the interface as stacked slabs with distinct electron densities (ρ), thicknesses (l) and roughness (σ) in each system for obtaining the vertical electron density profiles. The fitting was optimized by minimizing the χ^2 value after introducing initial thickness, electron density and roughness values reported in previous studies for similar systems or pure phospholipids but considering that the parameters obtained were physically relevant (95, 135, 136).

2.4.3. Polarization-Modulation Infrared Reflection Absorption Spectroscopy (PM-IRRAS)

PM-IRRAS allows to study the conformation and orientation of peptides *in situ* at the interface, either air/aqueous or inserted into a lipid monolayer in Langmuir troughs (Figure 2.3). As in IR spectra in solution the amide I and amide II bands are used to determine the secondary structure of the peptides at the interface. Amide I is assigned mostly to C=O stretching vibration and its frequency is determined by the secondary structure of the polypeptide chain and hydrogen bonding. It occurs between 1600 and 1700 cm^{-1} and is the most intense band in proteins and peptides. Amide II band is also conformation sensitive and appears in the region around 1510 - 1580 cm^{-1}. Its interpretation can be complex, and the peptide bond modes are derived mainly from the in-plane N-H bending and, in lesser degree, from C-N stretching (138–141).

The CH_2 stretching bands are indicators of conformational order/disorder in chain amphiphiles such as the hydrocarbon chains of phospholipids. It has been described that CH_2 symmetrical stretching shifts from ~2855 to ~2849 cm^{-1}, and asymmetrical stretching from ~2924 cm^{-1} to ~2919 cm^{-1} occur upon transitions from a liquid to a condensed state. These frequencies are sensitive to formation of gauche rotamers in the chains, which are formed in the liquid phase. In the condensed phase, the acyl chains must be in all-trans conformation. Thus, a lipid in a more conformationally ordered state is characterized by a CH_2 stretching mode $\leq$2850 cm^{-1}, with conformational disorder leading to higher frequency positions (138, 139).

PM-IRRAS combines FT-IR reflection spectroscopy with fast polarization modulation of the incident beam between parallel (p) and perpendicular (s) polarization. The two-channel processing of the detected signal enables acquisition of the differential reflectivity spectrum. In PM-IRRAS the photoelastic modulator allows alternation of linear states of the polarized light, which reduces the interference of water vapor and CO_2. Therefore, the modulated reflectivity can be sometimes advantageous over conventional IRRAS modes (142, 143).

The experiments were performed at Pavillon Alexandre Vachon, Université Laval (Québec City, QC) using a 36 cm^2 and 5 mm deep Teflon trough insert coupled to a NIMA pressure sensor in a closed chamber. The procedure for injection was as detailed in section 2.4.2 but using final peptide concentrations of 12.5 μM instead, given that intensity signals produced at lower concentrations were not strong enough for data analysis. The set up and measurements were done as previously described (144, 145), with certain modifications. Briefly, the spectra were recorded at the

air/buffer interface using a Nicolet iS50 Fourier transform IR spectrometer (Thermo Scientific) coupled to a photovoltaic MCT detector (Kolmar Technologies). A photoelastic modulator PEM-90 (Hinds Instruments) was used for modulating beam polarization and set for optimum efficiency. Each spectrum resulted from the co-addition of 1024 interferograms to improve signal to noise ratio and was recorded at a scanning mirror velocity of 0.47 cm/s and 8 cm^{-1} resolution, resulting in an acquisition time of ~ 20 minutes each. The normalized PM-IRRAS spectra were obtained using:

$$\frac{\Delta S}{S} = \frac{[S(d) - S(0)]}{S(0)} \qquad \text{Equation 3}$$

where S(d) and S(0) are the PM-IRRAS signals of the sample (monolayer with or without peptide) and the subphase, respectively. The spectra were recorded along with their corresponding peptide insertion profiles by monitoring the changes in surface pressure for each system.

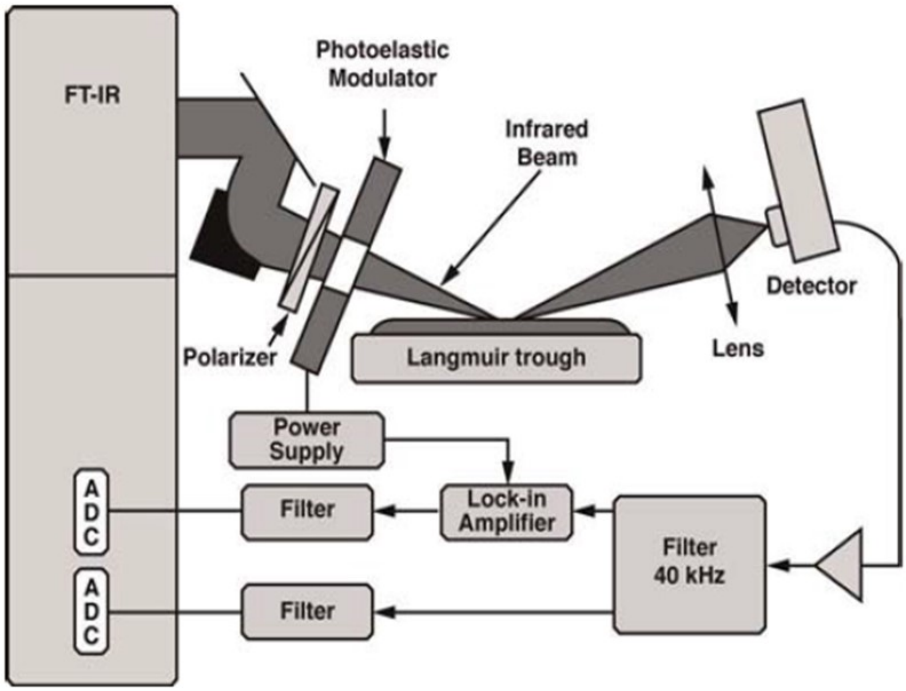

Figure 2.3. Schematic representation of PM-IRRAS setup at the air/aqueous interface (143)**.**

Spectra were analyzed using OMNIC™ Series Software (Thermo Scientific) correcting for baseline deviations with a spline function and water vapor contribution by subtracting a water vapor reference spectrum, in arbitrary intensity units. The ratios of peptide containing spectra with their respective lipid monolayers spectra were used for graphing the amide bands. The spectra obtained were used to estimate the orientation of the peptides at the interface by comparison to previously reported simulations by Blaudez et al. 2011 for ß-sheet forming peptides (143). The

buffer spectrum was subtracted from each spectrum of lipid films before and after peptide addition for the analysis of the CH_2 stretching.

2.4.4. Atomic Force Microscopy (AFM)

AFM was used for characterizing the molecular topography and morphology of the lipid monolayers deposited on mica with (sub)nanometer resolution. Monolayers of the eukaryotic models were spread on PBS buffer as described before and laterally compressed in a Langmuir trough until reaching a surface pressure of 30 mN/m. The films were then transferred to mica from the air/buffer interface using the Langmuir-Blodgett deposition method in which the solid support, previously inserted in the subphase, was withdrawn at controlled speed maintaining the desired surface pressure. The lipid monolayers adhered to the mica were then imaged with AFM.

This scanning probe technique records the interaction forces of a sharp cantilever tip as it scans the surface of a sample. A piezoelectric scanner adjusts the tridimensional positioning of the sample with high precision. For that, a photodiode collects the deflection of a laser beam aligned with the top of the flexible cantilever tip. The deflection signal resulting from the interaction forces between the tip and the surface is transformed into an image of the monolayer topology while the sample is moved by the scanner (146). AFM was performed in tapping mode in a Nanoscope IIIa (Digital Instruments, CA) instrument to scan the samples. In this mode we used etched silicon cantilevers with a tip radius of <10 nm oscillating at a frequency of ~300 kHz, and oscillation amplitude of 175 mV. The nominal spring constant was 20-80 N/m, scan rate 0.75-1 Hz, and a medium damping of ~25% was used. Height differences and sizes of the lipid domain could be determined from NanoScope Analysis software V1.5 (Bruker Co.).

2.5. Experimental techniques using liposomes

2.5.1. Vesicle preparation

Large unilamellar vesicles (LUVs) were prepared for the different model membranes as described previously (107), with some variations. The dried films (free of chloroform) containing the desired phospholipid composition were hydrated in PBS buffer (10 mM phosphate buffer, 2.7 mM potassium chloride, 137 mM NaCl, pH 7.4) for 1-2 hours and vortexed before extruding 41 times

through 100 nm pore polycarbonate filters. The size and stability of the LUVs was monitored by measuring the hydrodynamic radius using dynamic light scattering (Zetasizer Nano-S, Malvern Instruments, Ltd).

2.5.2. Circular dichroism (CD).

CD was used for the determination of the peptide secondary structure in bulk. The CD spectra for the peptides were recorded using a Jasco J-815 CD spectrometer at a concentration of 15 μM in presence and absence of liposomes to monitor the change in secondary structure. The phospholipid concentrations in liposome solutions varied to obtain peptide/lipid ratios (P/L) of 1/2.5, 1/20 and 1/50. All experiments were done in triplicate and the spectra corrected by subtracting the corresponding buffer or liposome spectrum. Spectra of the peptides were normalized for pathlength, number of residues and concentration to give the mean residue ellipticity. Each spectrum collected is the average of 5 scans obtained using a 0.1 cm pathlength quartz cuvette at 25 °C from 200 nm to 260 nm wavelength, with a data pitch of 0.2 nm, scan speed of 20 nm/min and a response time of 1 second. No measurements were recorded below 200 nm due to low signal to noise ratio for PBS buffer. CD data were analyzed and normalized with OriginPro 2017 (OriginLab Corp. MA, USA). BeStSel platform was used for peptide secondary structure determination from CD spectra (147, 148).

2.5.3. Carboxyfluorescein (CF) release assays

The procedure was as described in Rex, 1996 and Huang, et al., 2009 (128, 149), with minor modifications. Briefly, the lipid films were hydrated in 10 mM HEPES buffer, 10 mM NaCl, 1 mM Na_2EDTA and ~134 mM NaOH (pH 7.4) containing 50 mM of the fluorescent dye 5(6)-carboxyfluorescein (CF) mixed isomers (≥95%, SIGMA ALDRICH). Then they were vortexed and subjected to 4 freeze-thaw cycles in liquid nitrogen and water bath at 50 °C, respectively, before extruding through 100 nm pore polycarbonate filters. The free CF dye was separated from the liposomes by size exclusion chromatography using a Sephadex G-50 column in standard buffer (10 mM HEPES, 107 mM NaCl, 1 mM Na_2EDTA and ~5-6 mM NaOH for pH 7.4). Osmolarity measurements of the dye solution (inside the vesicles) and standard buffer (outside of the vesicles) were controlled to be isoosmolar with a μOsmette micro osmometer (Precision Systems Inc.). The

final phospholipid concentrations in CF encapsulated liposomes were determined using the Stewart method preparing standard curves for each phospholipid mixture (150).

The leakage of vesicle contents was performed in black 96-wells microplates (PerkinElmer OptiPlates) in a TECAN Infinite M200 microplate reader. The CF encapsulated liposomes were added to wells at final phospholipid concentration of 25 μM varying the peptide concentrations to render P/L ratios of 1/2.5, 1/20 and 1/50 (refer to a representation of the experimental approach in Figure 2.4). The fluorescence intensity of the released CF was monitored for 30 minutes upon excitation at λ_{ex} = 489 nm and emission at λ_{em} = 520 nm. All experiments were conducted in triplicates and intrinsic controls with standard buffer for spontaneous dye leakage were included. Triton X-100 at 1% (v/v) was added at the end to correct for complete lysis and full dye release. The normalized efflux ($E_{(t)}$) over the time of the experiment was calculated from equation 1:

$$E_{(t)} = \frac{F_\infty - F_{(t)}}{F_\infty - F_0} \qquad \text{Equation 4}$$

where F_o is the initial fluorescence before addition of peptides, $F_{(t)}$ is the fluorescence intensity at time t, and F_∞ is the final fluorescence after addition of Triton X-100 1% (v/v). The leakage of the dye is calculated by the relation (1 - $E_{(t)}$) × 100% and reported here as the percentage of CF leakage (149).

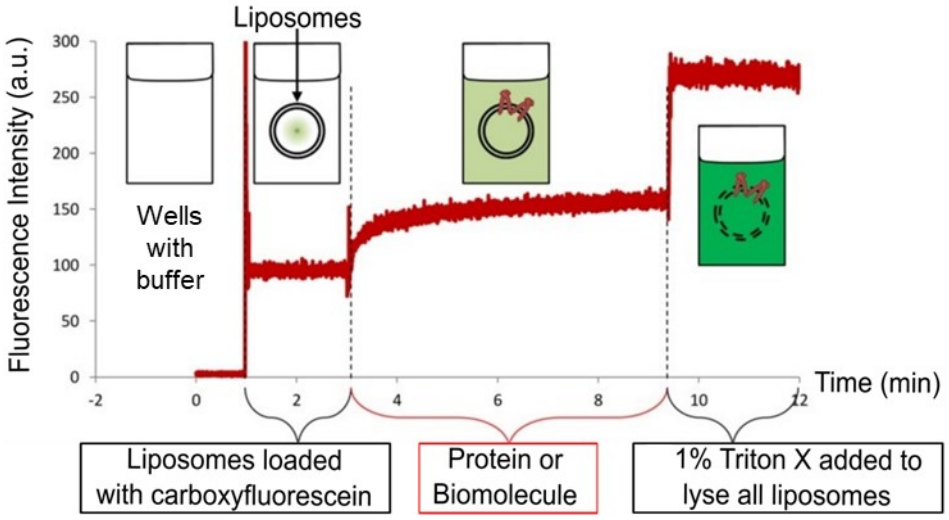

Figure 2.4. Representation of the assays to measure CF release upon liposome disruption. Image adapted from Jimah *et al* (151).

2.5.4. Localized Surface Plasmon Resonance (LSPR)

Surface plasmon resonance is a coherent oscillation induced by light or electromagnetic source of the conduction electrons in the surface of materials with a negative real and very low imaginary dielectric constant. Metal (usually gold) nanoparticles are used in the generation of LSPR in comparison to continuous thin gold films in conventional SPR. LSPR produces a strong resonance absorbance peak, which position is sensitive to the local refractive index around the nanoparticles (152). The instrument measures the wavelength shift of this peak in real-time upon ligand or analyte accumulation, rather than the variation of the resonance angle as in traditional SPR (https://nicoyalife.com/nicoya-surface-plasmon-resonance-resources/what-is-spr/lspr-vs-spr-2/).
The reduced electromagnetic field decay length in LSPR sensors offers smaller sensing volumes, making their response comparable to SPR when short-range changes of the refractive index are analyzed. However, this reduction makes LSPR less sensitive to bulk effects (152).

The kinetics of the peptides' interaction with the different liposome model membranes was investigated with LSPR analysis using the single channel OpenSPR (Nicoya LifeSciences, Waterloo, ON, Canada). The experiments were performed at 22 °C with an 80 μL loading loop following a kinetic titration approach, in which four concentrations of the peptides (1, 5, 10 and 25 μM) were flowed over the immobilized liposomes in a LIP-1 sensor chip (Nicoya Lifesciences). The binding affinities of the interactions were determined by fitting the sensograms to a 1 to 1 and a 1 to 1 two-state kinetic models in TraceDrawer (software V 1.8).

Chapter 3. **Results and Discussion for antibacterial activity**

3.1. Interaction of GL13K peptides with bacterial membranes

3.1.1. Role of membrane charge

Compression isotherms of the DOPE/DOPG/CL monolayers at 75/20/5 and 15/80/5 molar % ratios spread at the air-buffer interface are presented in Figure 3.1. Both phospholipid mixtures and pure PLs formed stable monolayers at the air/buffer interface, up to collapse surface pressures of nearly 45 mN/m. Critical areas and compression behaviour were similar for both bacterial models. The differences lie on the slightly closer lipid arrangement and lower collapse pressure of the inner membrane model with respect to the OM. Isotherms for pure lipids are included in the Supplementary Information.

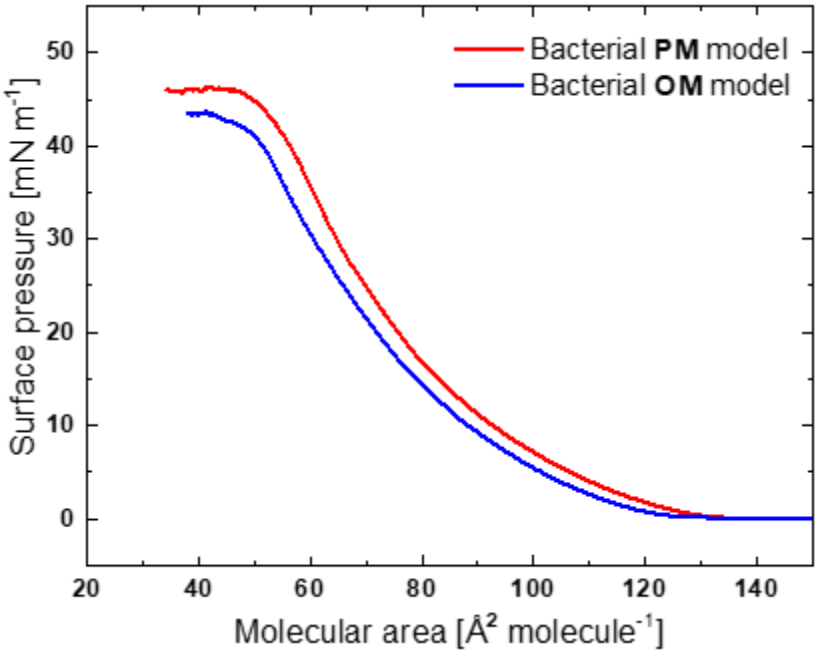

Figure 3.1. Surface pressure-area isotherms of the phospholipid mixtures mimicking bacterial plasma membranes (PM: DOPE/DOPG/CL 15/80/5) and outer membrane (OM: DOPE/DOPG/CL 75/20/5) of Gram-negatives, both in PBS buffer pH 7.4. Both monolayers show similar critical areas and surface area compression behaviour despite the great difference in charge (~85% anionic phospholipids in PM model vs ~25% in OM model).

All the phospholipids utilized for these bacterial model membranes were unsaturated and rendered fluid phases as supported by their isotherms and no Bragg peaks present in GIXD data at a biological pressure of 30 mN/m. In addition, previous studies have shown that POPE and POPG are ideally mixed and form stable monolayers at the air/buffer interface, supported by very low ΔG_{mix}, with only minor increments upon increasing surface pressure, and favored by the similar size and shape of both phospholipids (153). The POPE and POPG mixtures presented a fluid liquid expanded (LE, monolayer equivalent of liquid disordered phase of bilayers) state, whereas POPE and CL formed fluid but non-ideal mixtures in a LE state. Mixtures of POPE and CL have great deviations from ideality only above 20 % of CL at ≈ 33 mN/m (153). We therefore anticipate that 5 % of CL, as is our case, should not impact the interfacial behavior of the mixture as was reported for SOPE/SOPG/CL 15/80/5 (154). Notably, both of these reports comprised lipids with one saturated and one unsaturated chain, whereas our PLs contain unsaturations on both of their hydrocarbon chains which should increase their fluidity and miscibility. Moreover, AFM results for both POPE:POPG and POPE:CL mixtures show no phase separation (no lateral domains) at a surface pressure close to 30 mN/m (153).

We introduced the peptides into the subphase under the monolayers at 30 mN/m to relate membrane compositional differences to the peptide activities. The insertion profiles in Figure 3.2 revealed that the initial interaction driven by electrostatic forces is governed by the charge and composition of the membrane rather than by the peptide chirality as no considerable differences were observed between D-GL13K and L-GL13K. However, for both enantiomers the inner membrane model (DOPE/DOPG/CL 15/80/5) with higher content of anionic phospholipids revealed a sharper and greater initial change in surface pressure revealing higher affinity, which was reproducible at other peptide concentrations and experimental settings (including the setup for X-ray scattering experiments at the Synchrotron). The results indicate that the GL13K variants target and can partition into membranes of both Gram-positives and Gram-negatives, in agreement with their evidenced broad-spectrum antibacterial activity (refer to Table 1.1). The model with lower charge (OM) showed slower stabilization of the surface pressure upon insertion of both GL13K peptides. However, both model systems ultimately reached approximately the same equilibrium surface pressures after ~33 minutes.

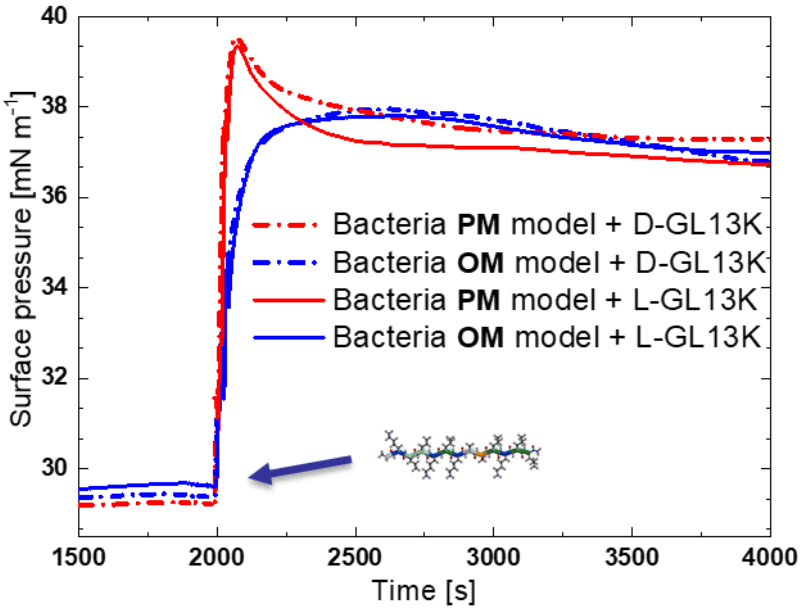

Figure 3.2. Interaction of GL13K enantiomers with bacterial monolayers. Red lines correspond to the PM model (DOPE/DOPG/CL 15/80/5) and blue lines to the OM model (DOPE/DOPG/CL 75/20/5). The monolayers were formed by spreading the lipid mixtures onto an PBS subphase to give an initial surface pressure of 30 mN/m, mimicking naturally occurring membranes. D-GL13K (dashed lines) and L-GL13K (solid lines) at 10 µM were then introduced into the subphase and changes in surface pressure monitored.

To assess if the partition to the membranes renders affinity differences as a function of membrane charge and peptide chirality, LSPR experiments were performed using liposomes. The data were fit using three different binding models: a 1-to-1 (describing a monovalent ligand-peptide interaction), a 1-to-1 two-state (considering 2 different binding states one after the other such as in a conformational change), and a 1-to-2 binding model (i.e. two independent binding events occur in parallel for the peptide in solution). It should be noted that none of these models truly represent the binding of a peptide to a liposome wherein there is not a specific binding site as one might find for a protein-ligand interaction. To this moment, it was determined that the 1-to-1 model provided the most reasonable K_D values based on the combination of two criteria, namely accuracy of the fit to the data and coherence of the affinity concentrations with known concentrations at which the peptides exhibit efficacy and interaction in other cell and model membrane experiments. However, the 1-to-1 two-state binding model should theoretically be more coherent according to the structural results further described in this thesis for GL13K peptides in presence of the bacterial model membranes. Within the 1-to-1 model, four different parameterizations were assessed

including Bmax perset, or global, and diffusion or depletion corrected fitting. The equilibrium dissociation constant (K_D) values for each of the parameterizations were usually of the same order of magnitude. For example, for the bacterial OM model with L-GL13K the values varied from 2.4 x 10^{-6} to 8.8 x 10^{-6} M using different parameters for several fits with the 1-to-1 binding model. In order to make direct comparisons between systems, only the data for the 1-to-1 model with diffusion correction is included in Table 3.1.

Table 3.1. K_D values for the interaction of GL13K enantiomers with liposomes of the bacterial model membranes.

Bacterial models (phospholipid compositions)	K_D (M)	
	D-GL13K	L-GL13K
(OM) DOPE/DOPG/CL 75/20/5	2.2 x 10^{-6}	2.4 x 10^{-6}
(PM) DOPE/DOPG/CL 15/80/5	8.6 0x 10^{-7}	2.0 x 10^{-7}

The PM model membranes exhibit K_D values one order of magnitude lower than those for the lower charge OM models, in agreement with the higher binding affinity observed with the surface pressure measurements. For both model membranes, the K_D values for the two enantiomers are similar (same order of magnitude) without considering the errors of the fits, also in agreement with the insertion data. Although it appears that the L-GL13K binds with higher affinity to the PM liposomes in both the data above as well as the evaluation of the sensorgrams, we cannot conclusively attribute higher affinity to one enantiomer over the other considering the variability of the data, the corresponding fits, and the instrument limitations. Further analysis of the LSPR data is required to accurately assess the influence of the peptide chirality on the binding affinity of GL13K enantiomers with the bacterial model membranes.

3.1.2. Peptide structural changes and role of peptide chirality

Circular dichroism provides us with the information of a conformational change in presence of vesicles with the PLs mixtures of interest. The CD spectra for GL13K enantiomers in presence and absence of the bacterial membrane models is presented in Figure 3.3. All experiments were

conducted at the same final concentration of 15 μM to avoid concentration effects. As observed for the peptide solutions in absence of liposomes, the ellipticity describes a distribution corresponding to a random coiled or unstructured conformation. When liposomes are added, we observed a minimum (or maximum considering inverted spectra for the D-enantiomer) forming at around 222-223 nm for the highest peptide to lipid ratio which was generated by the conformational change of the peptides in the presence of the bacterial PM model (~90 % anionic charge). The spectra for the bacterial OM model at the highest P/L ratio did not show this transition. As the P/L ratios decrease (with higher concentrations of the liposomes) the ellipticity minimum or maximum shifts to lower wavelengths of ~217 nm more typical of the β-sheet conformation (147, 148). This has been observed for other beta-sheet forming peptides at decreasing P/L ratios (123) and previous studies with GL13K (109) in model membranes containing anionic phospholipids. The shift toward a lower number occurred as well for random coiled/PPII peptides, such as SAP, with temperature increase or longer interactions (155). The higher peptide abundance can cause self-association or aggregation due to membrane coverage, which can hinder the folding process of the peptide population in solution.

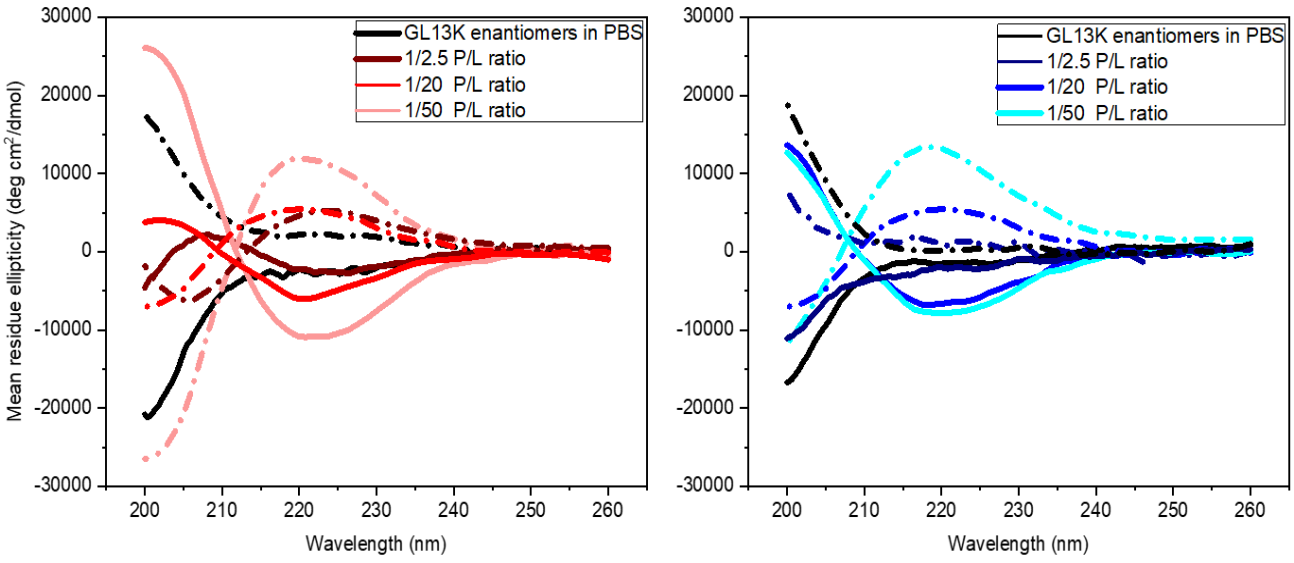

Figure 3.3. CD spectra of GL13K enantiomers in solution and in presence of bacterial membrane LUVs representing the mean residue ellipticity. Red toned lines correspond to the PM model (DOPE/DOPG/CL 15/80/5) and blue gradient lines to the OM model (DOPE/DOPG/CL 75/20/5) depending on the P/L ratios. D-

GL13K (dashed lines) and L-GL13K (solid lines) at 15 µM were added and mixed with the LUVs in the cuvettes after measurement of the buffer or LUVs baselines.

According to the estimations from BeStSel (147, 148), approximately 40 to 45 % of the peptide was present as antiparallel beta-sheets in presence of the bacterial model membranes. Another 17–22 % was estimated as turns, and the rest as unstructured. Even though prediction tools allow us to estimate the secondary structure, CD is not specific to interfaces.

GIXD is a surface sensitive technique producing Bragg peaks with distinctive Q_{xy} positions that correspond to the d-spacing (d) of the crystallites in the 2D lattice (135). Spacings of ~4.75 Å corresponding to Bragg peaks at ~1.32 in Q_{xy} are reported to define the inter β-strand distance that characterizes the H-bond network of the β-sheet conformation (156). All systems studied, except for L-GL13K interacting with the OM model, rendered Q_{xy} positions (Figure 3.4) and d-spacings in agreement with a crystalline β-sheet formation. When no Bragg peak is present, it could mean that there are no 2D crystalline peptide structures at the interface (or there are not enough crystalline peptide structures in the beam footprint to be measurable) or the crystalline structures that are present are weakly ordered with very low correlation lengths such that they cannot be distinguished from the background. Our resulting structural parameters for the peptide crystallized domains are presented in Table 3.2.

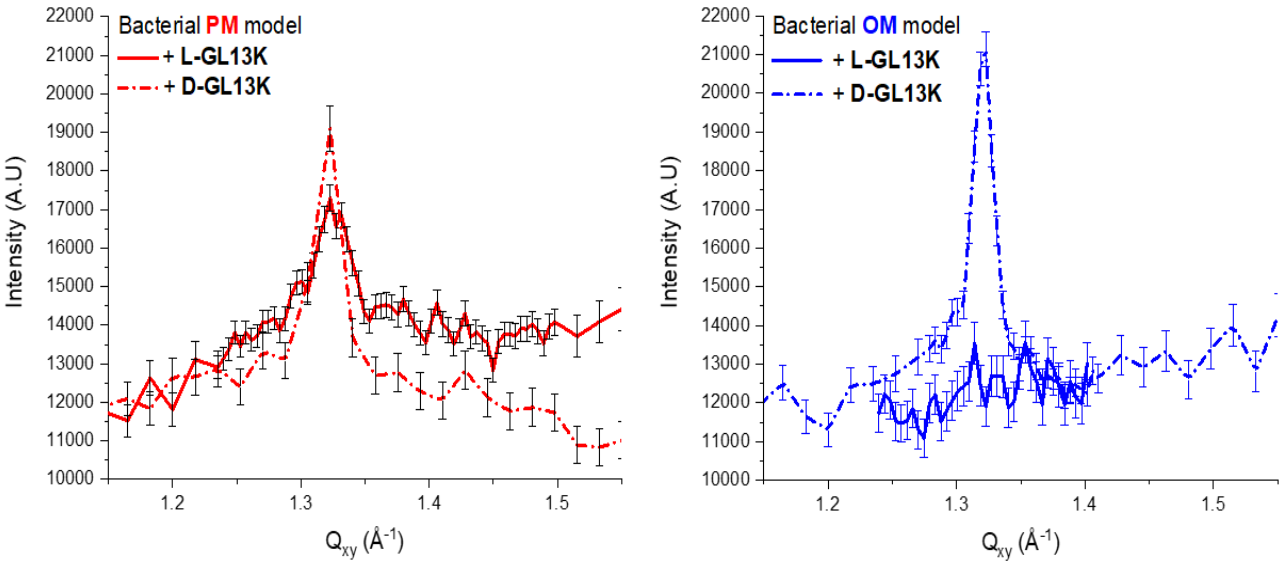

Figure 3.4. Bragg peaks obtained from GIXD for GL13K enantiomers in interaction with bacterial PM (left) and OM (right) monolayers at the air/buffer interface. The monolayers with the bacterial phospholipid mixtures were spread until reaching a surface pressure of 30 mN/m on PBS, pH 7.4. D-GL13K (dashed lines) and L-GL13K (solid lines) were inserted in the subphase underneath at 5 µM and 10 µM. Only the data of the peptides at 5 µM is represented.

The coherence or correlation length (L_{xy}), derived from the $FWHM_{int}$, is the distance in Q_{xy} over which the structure or domain is ordered. In presence of both bacterial models the D enantiomer showed Bragg peaks with L_{xy} in the order of ~300 Å corresponding to approximately 64 peptides. The Bragg peak observed for L-GL13K interacting with the PM model showed a correlation length that is approximately half of those for D-GL13K. Moreover, there was no Bragg peak formed by L-GL13K at 5 and 10 µM (in a new set of experiments) in presence of the lower charge OM model (DOPE/DOPG/CL 75/20/5). It is noteworthy that L-GL13K adopts a β conformation in presence of the OM model as observed by circular dichroism and PM-IRRAS experiments, but GIXD reveals that they are not crystalline at the conditions tested. A lower charge of PLs in interaction with L-GL13K may explain the disappearance of ordered peptide regions manifested as absent or reduced L_{xy} (95). However, given that the D-GL13K forms equally crystalline structures with either model, this suggests an important role of peptide chirality in the formation of a crystalline secondary structure. This indicates a mechanism independent of resistance to proteolytic cleavage underlying the differential antibacterial activity effectiveness of GL13K enantiomers.

Table 3.2. Fitting parameters calculated from Bragg peaks of GIXD data for GL13K enantiomers in interaction with bacterial monolayers at the air/buffer interface.

Peptide	Bacterial Models	Q_{xy} ($Å^{-1}$)	d-spacing (Å)	L_{xy} (Å)
D-GL13K	(**PM**) DOPE/DOPG/CL 15/80/5	1.321	4.75	~302
	(**OM**) DOPE/DOPG/CL75/20/5	1.321	4.75	~316
L-GL13K	(**PM**) DOPE/DOPG/CL 15/80/5	1.324	4.74	~169
	(**OM**) DOPE/DOPG/CL75/20/5	-	-	-

(-): indicates that no Bragg peaks were obtained (as observed in Figure 3.4).

A two-dimensional ordering of peptides at the interface has been observed by GIXD in other beta-sheet forming peptides, including Aβ amyloid monolayers. In these cases a second diffraction peak is present at much lower Q_{xy} values indicating a d-spacing that corresponds to the end-to-end distance of each peptide strand (156–158). Therefore, it would be possible to calculate the dimensions in both directions of the 2D crystalline order for the peptide films. For GL13K peptides, we obtained a 2D arrangement of β-sheet secondary structures that is only crystalline in one direction as the lower Q_{xy} diffraction peak for the end-to-end organization was not observed. This may be because of low signal to noise ratio at very low scattering angles or that the signal for the lower Q_{xy} peak was not differentiable from that of the striking beam signal.

GIXD results demonstrate a crystalline organization for the arrangement of β-sheets, but it does not provide information on the orientation of the peptides nor of its specific conformation at the interface. PM-IRRAS allows assessing the orientation at the air/water interface. The amide I (essentially C=O stretching) and the amide II (C-N stretching, C-N-H bending) vibrational modes in PM-IRRAS are indicative of the backbone secondary structure. PM-IRRAS spectra of the GL13K peptides inserted in the bacterial model monolayers at the air/buffer interface (Figure 3.5) displayed a split of the Amide I band with a very strong positive band around 1622 cm-1 (Amide BI) and another positive weaker one around 1693 cm^{-1} (Amide BI'). The Amide II band had a frequency of ~1536 cm^{1}. These frequencies are assigned to an extended β-sheet formation, for which Amide I bands are typically found at frequencies ~1624 cm^{-1}. However, this band has been shown to sharpen and shift to lower wavenumbers with increasing number of β-strands (143, 157). Additionally, the large splitting of the amide I band with the positive contribution at ~1693 cm^{1} characterizes the presence of antiparallel β-sheets structures (143, 159).

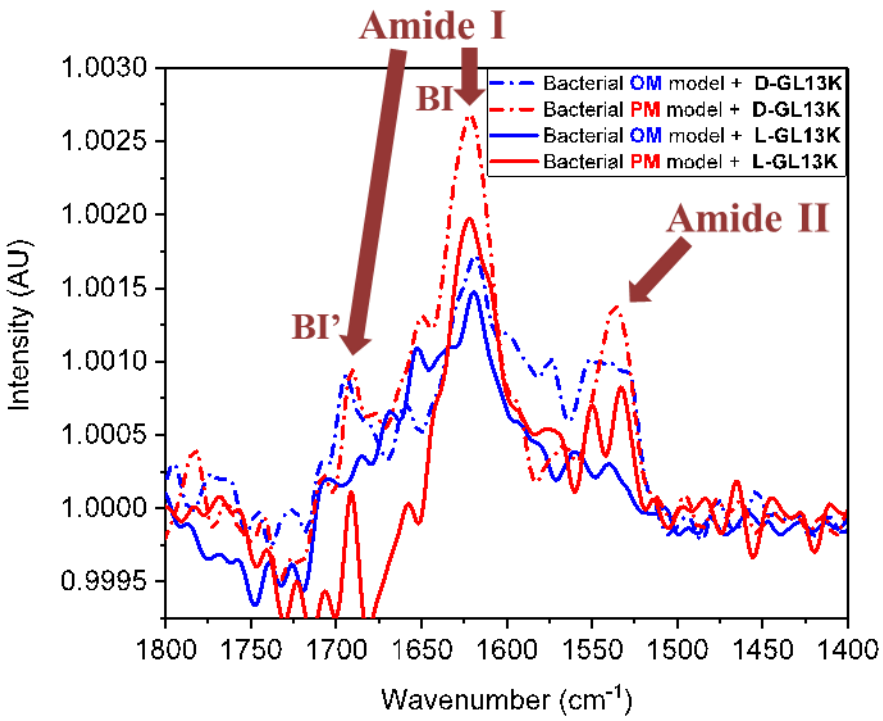

Figure 3.5. PM-IRRAS spectra of GL13K enantiomers inserted into bacterial model membranes at the air/buffer interface. The monolayers with bacterial phospholipid mixtures were spread until reaching a constant surface pressure of 30 mN/m on PBS, pH 7.4. D-GL13K (dashed lines) and L-GL13K (solid lines) were injected into the subphase at 12.5 µM.

The lower intensity of the amide I and II bands in the PM-IRRAS spectra for the L-enantiomers may indicate, in agreement with GIXD, that the D-enantiomers may be more structured at the interface. In particular, L-GL13K exhibits a low contribution of the amide BI' (if present) and amide II bands upon injection in the monolayer of the less charged bacterial OM model compared to the other systems. This, along with some contribution from random structures around 1654 cm^{-1}, reflects that L-GL13K is less structured at the interface when less charge is available. Since the amide BI' at ~1693 cm^{-1} is relatively undefined and the amide II is barely noticeable, a crystalline antiparallel β-sheet conformation for L-GL13K is unlike to occur in more zwitterionic models as observed in GIXD.

A weak band contribution around 1655 cm^{-1} emerges in the GL13K spectra. This frequency can be assigned to α-helices, but it is not separable from that of unstructured random coils. The latter can reflect a fraction of peptide residing at the interface but that has not undergone a transformation into beta-sheets. As PM-IRRAS is surface specific this fraction must be located within the lipid

monolayer or just below. This observation agrees in principle with results obtained by Harmouche et al. using NMR (109), in which a small portion of GL13K adopts an α-helical conformation upon interacting with membranes at very low peptide:detergent or peptide:lipid ratios before transitioning to the more abundant β-sheet arrangements. They attributed the high conformational plasticity of GL13K to its high charge and small hydrophobic face (109). Similarly, amphiphilic amyloidogenic peptides have been reported to go through an initial state with an α-helical conformation upon adsorption at hydrophilic-hydrophobic interfaces (160). In the amyloidogenic peptides the band intensities increased with higher lateral surface pressures, and greater ratios of amide B1 intensities (~ $I_{1625\ cm\text{-}1}$ / $I_{1655\ cm\text{-}1}$) indicated a transition from α-helices to β-sheets at 30 mN/m (160). However, it should be noted that the detection limit of IRRAS may not allow to detect this initial state of random coil/α-helix when their concentration at the interface is low (160).

Differential orientations of the peptides at the interface were observed according to their chirality (Table 3.3). Strong spectral bands pointing upwards are indicative of absorption transition moments oriented in the interface plane, while perpendicular transition moments render medium and/or downward-oriented bands (140). By comparison to PM-IRRAS simulations reported by Blaudez et al. (143) for β-sheet forming peptides, we estimated the orientation of GL13K enantiomers at the monolayer interface. L-GL13K presents a more planar orientation (Ψ≈0) at the interface when interacting with the bacterial models in contrast to the tilted orientation of D-GL13K (Ψ≈45°). The phospholipids charge also has an influence on the rotation of the L-GL13K strands on the monolayer plane (the θ angle). A study with similar β-stranded amphipathic peptides of 9-15 amino acids and containing the Lys-Leu (KL) repeating motif revealed comparable results at the air/water interface (140).

Table 3.3. Orientation angles estimated from simulations reported by Blaudez *et al.* (143) for GL13K enantiomers at the interface upon interaction with bacterial models.

Phospholipid composition in bacterial models	D-GL13K		L-GL13K	
	Ψ	**θ**	**Ψ**	**θ**
(OM) DOPE/DOPG/CL 75/20/5	**45°**	**~50°**	**0°**	**~50°**
(PM) DOPE/DOPG/CL 15/80/5	**45°**	**~55°**	**0°**	**~90°**

So far, we understand that the GL13K enantiomers form β-sheet crystalline arrangements that differ in orientation, affinity, and crystallinity according to the peptide chirality and the charge density of the bacterial membrane. However, it is not clear yet how far they initially penetrate the membrane or the peptide vertical localization in the plane of the monolayer. XRR was used to help address this question by analyzing the electron densities in the vertical plane of the monolayer.

The electron density profiles of the bacterial models at the interface before and after interaction with both GL13K enantiomers are presented in Figure 3.6. Attempts to fit with a two-box model for the phospholipid only mixtures resulted in poor fits with very large $\chi 2$ values. The XR data were best fit using three slabs (or three box models) with electron density (ρ), thickness (d) and roughness (σ) values that varied before and after peptide insertions (Table 3.4). The monolayer systems show a distinct lipid acyl chains region (slab 1), headgroup regions (slab 2), and a subphase layer higher in electron density than the bulk PBS subphase, associated with structure water and adsorbed counterions (161, 162) and/or peptides (slab 3). The data obtained from XRR is sensitive to crystalline and non-crystalline phases and the slabs represent an average configuration of the monolayer by considering both the ordered and disordered phases (163). XRR data in presence of GL13K peptides can also be fit with a four-box model, although its interpretation is theoretically more complex and renders increased thickness of the monolayer. The ordered phase here is attributed to the presence of GL13K peptides and a disordered phase is evident without the peptides in the bacterial model monolayers, as observed in GIXD.

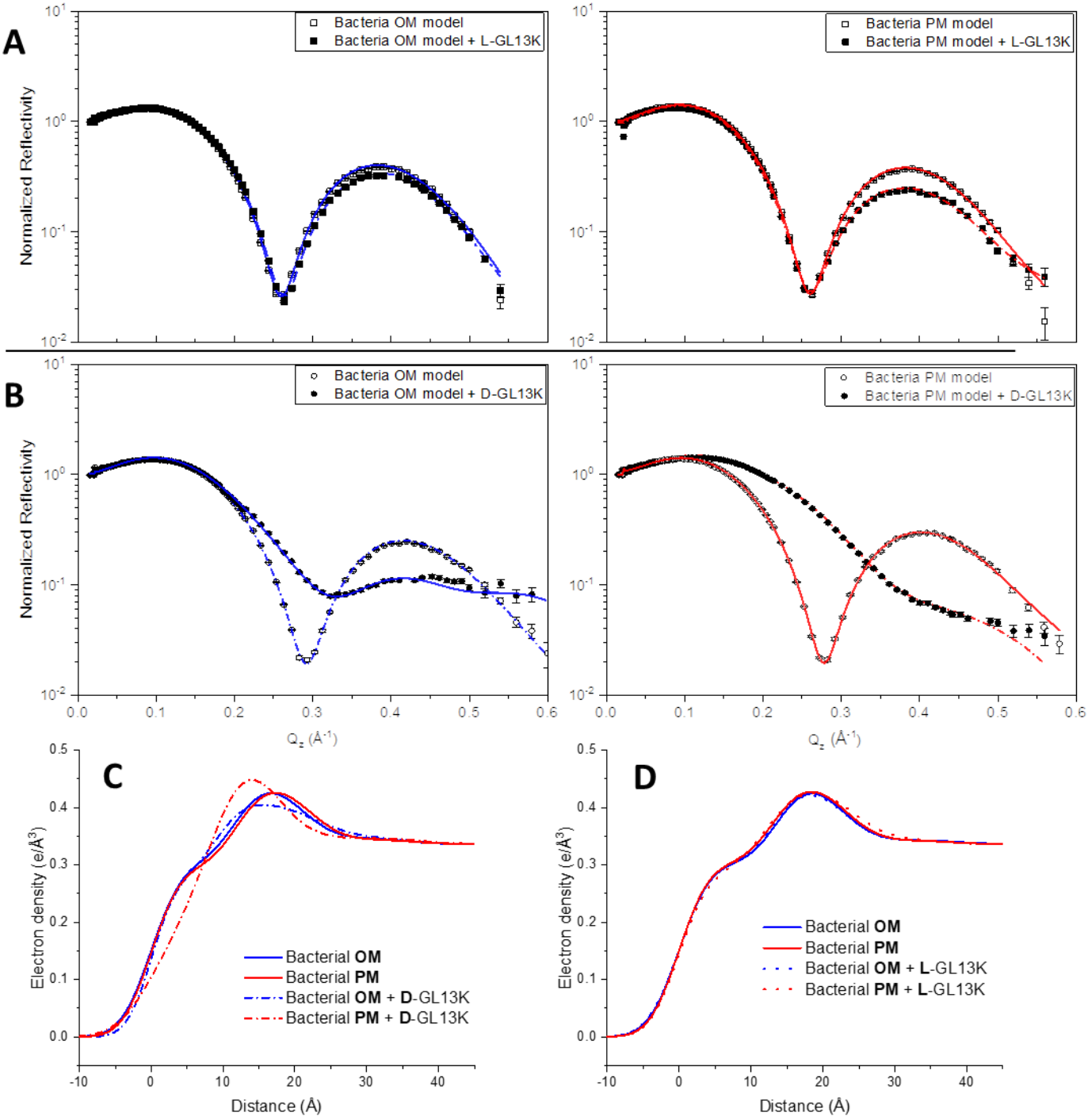

Figure 3.6. Reflectivity data (A and B) and electron density profiles (C and D) of bacterial model monolayers in the absence and presence of peptides at the interface. The monolayers were spread until reaching a constant surface pressure of 30 mN/m on PBS. GL13K enantiomers were injected into the subphase at 5 µM. Solid lines correspond to the fits of phospholipid monolayers (Blue and red for bacterial OM and PM respectively) whereas interrupted lines correspond to fits after the peptides were injected.

The electron density profiles, and fitting parameters showed that the electron density distribution of the model membranes varied most notably with the insertion of the D-GL13K enantiomer, whereas the profiles are similar before and after injection of L-GL13K. The lack of change for L-GL13K implies that either a diffuse layer or low concentration was adsorbed underneath the monolayers at 30 mN/m on PBS. These results further confirm that the chiral nature of the peptide is a determinant for the insertion or penetration of AMPs into bacterial membranes. From a biophysical and biochemical stand point, our results also juxtapose previous implications from data reviews that declare no evident antibacterial activity differences between all-D and all-L peptide enantiomers (124).

As observed in Table 3.4 for both models, the D enantiomer reduces the thickness of the acyl chain region (slab 1) in both membrane models, either by pulling the phospholipids down to the subphase or penetrating farther up into the monolayers. This occurs concurrently with an increase of the electron density in the case of the PM model (~90 mol % anionic) and decrease on the OM model (~25 mol % anionic), meaning that this peptide could penetrate deeper in more negatively charged membranes. Interdigitated peptide hydrophilic moieties between the phospholipids can cause the increase in the electron density.

Table 3.4. Parameters for fitting x-ray reflectivity data of bacterial models at the interface upon interaction with GL13K enantiomers. Electron density (ρ), thickness (d) and roughness (σ) values are presented for each layer/slab in all systems. Numbering of the slabs is made in the direction air to subphase (the electron density of the buffer subphase was 0.337 $e^-/Å^3$).

System	Slab 1			Slab 2			Slab 3			χ^2	Total thickness
	d (Å)	ρ ($e^-/Å^3$)	σ (Å)	d (Å)	ρ ($e^-/Å^3$)	σ (Å)	d (Å)	ρ ($e^-/Å^3$)	σ (Å)		
DOPE:DOPG:CL 75:20:5	12.5	0.314	3.32	7.2	0.472	4.04	16	0.347	4.1	15.8	35.7
DOPE:DOPG:CL 75:20:5 + 5 uM **D-GL13K**	8.9	0.273	3.23	14	0.412	4.91	13.9	0.346	2.4	19.8	36.8
DOPE:DOPG:CL 15:80:5	12.0	0.297	3.29	10.2	0.42	3.29	13.4	0.344	3.1	15.1	35.6
DOPE:DOPG:CL 15:80:5 **+ 5 uM D-GL13K**	9.0	0.21	4	7.4	0.54	4.3	21.3	0.343	2.73	24.6	37.8
DOPE:DOPG:CL 75:20:5	13.8	0.3	3.43	8.9	0.45	3.43	14.1	0.34	3.43	27	36.8
DOPE:DOPG:CL 75:20:5 **+ 5 uM L-GL13K**	13	0.306	2.9	10.1	0.434	3.35	15.1	0.343	2.7	19	38.2
DOPE:DOPG:CL 15:80:5	13.4	0.307	3.25	9.4	0.45	3.85	15.3	0.34	3.15	23	38.1
DOPE:DOPG:CL 15:80:5 **+ 5 uM L-GL13K**	13.1	0.31	2.93	9.8	0.45	4.9	18.1	0.34	2.8	46	41.0

In a broader consideration, we can state that most likely GL13K peptides do not form fibrils in presence of the model membranes. Evidence from studies on the architecture of cross-β amyloids (164), interfacial activity of GL13K (111), and PyMOL modelling of the peptide support this statement. β-strands that deviate from a perpendicular sheet orientation and present an axial twist even at short-range do not favor a regularly repeating pattern in a highly ordered arrangement such as fibrils (164). Experimental results from AFM do not support the β-sheet fibril formation (111), despite that D-GL13K showed self-assembled nanoribbons and nanofibrils by TEM imaging but only after 2 days in solution at pH 9.8 (165). Moreover, the GL13K peptide shows an axial twist when modelled as a extended β-strand in PyMOL (Refer to Figure 3.7). Therefore, formation of

fibrils in a physiological microenvironment does not seem likely for GL13K peptides despite the β-sheet crystallinity observed by GIXD in presence of bacterial model membranes.

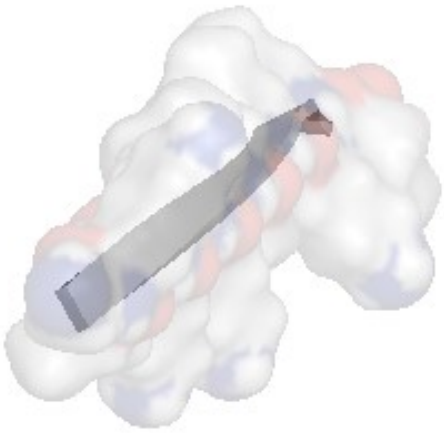

Figure 3.7. Cartoon and surface representation of a GL13K twisted β-strand conformation. Backbone shown as a ribbon in image created using PyMOL software (Copyright 2006 DeLano Scientific LLC)

However, the lack of nanofibril formation must not jeopardize GL13K peptides membranolytic effect given their broad-spectrum antimicrobial activity. Dye-encapsulating LUVs of the bacterial models were constructed to assess said lysing ability on both GL13K enantiomers at different peptide/lipid ratios. This was monitored by evaluating the release of CF over time upon addition of the peptides. Only the highest peptide to lipid ratio of 1/2.5 (or 0.4) led to the complete lysis of the vesicles, measured as the release of the CF dye from the liposomes in Figure 3.8. The other two P/L ratios, 1/20 (0.05) and 1/50 (0.02), caused low (~9-16 %) to none (~0 -1.4 %) membrane disrupting effect, which is indicative that GL13K peptides do not form membrane pores as supported by previous evidence (107).

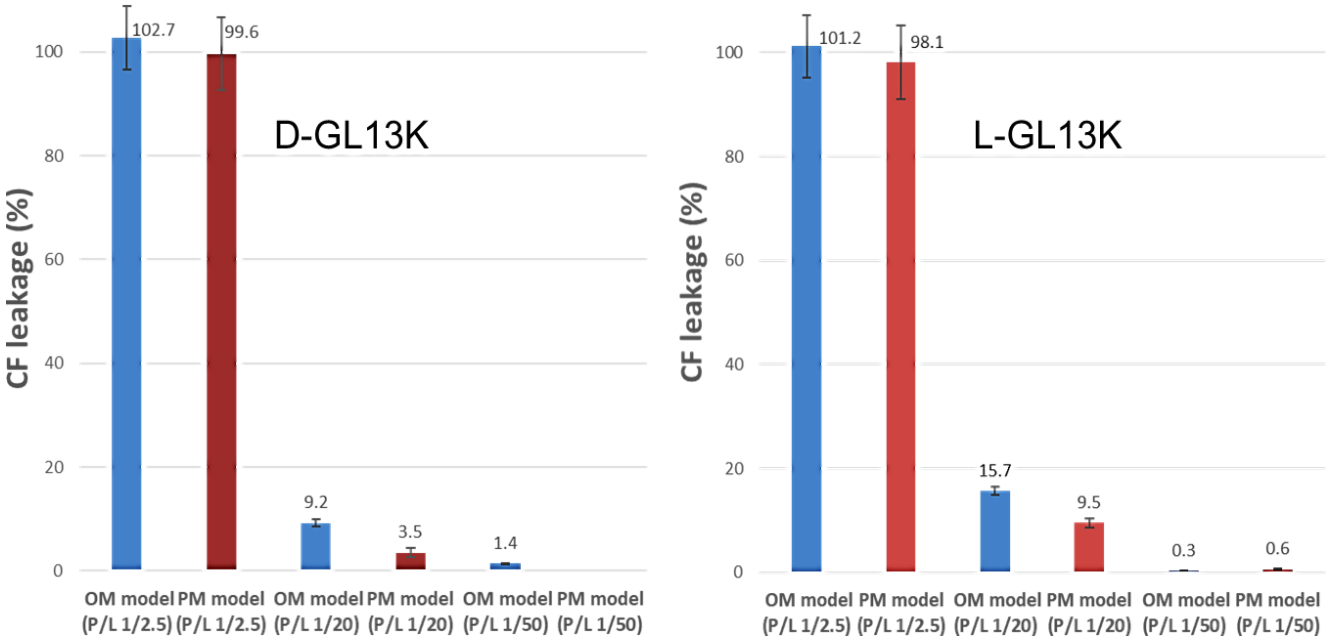

Figure 3.8. Disruption of the liposomes containing the bacterial membrane lipid compositions by GL13K enantiomers. The bacterial OM model (DOPE:DOPG:CL 75:20:5) is shown is blue and the PM model (DOPE:DOPG:CL 15:80:5) in blue. Lipid concentration of liposomes was kept as 25 µM.

Interestingly, the L-enantiomer of GL13LK led to higher disruption in the lower peptide to lipid ratios in presence of both models. This seems counterintuitive based on the results here presented and the much better bioactivity of the D-GL13K. However, in evaluations of the L to D amino acid conversion and deamidation of the antimicrobial peptide anoplin (GLKRIKTLL-NH2), similar results were found for bacterial model membrane compositions: DOPE/DOPG 80/20 mol, DOPG/CL 55/45 mol% and DOPE/DOPG/CL 12/84/4 mol%. Greater differences in membrane disruption were found at the lower peptide to lipid ratios, as it is our case. Won et al. considered that the lytic activity of anoplin peptides could be related with the content of CL in the membrane (166), which is not our case because both bacterial models contain the same ratio of CL. More importantly they noticed that the disruption of the anionic cell membrane models by anoplin is generally observed below certain concentration or P/L ratio. In comparison, we observed that the release only occurs at ≥1.25 µM or P/L ratio 1/20, below which the differences are negligible.

Considering that peptide chirality was not a determinant factor in the membrane disruption assays, we must account for other potential mechanisms that could explain the D-GL13K enantiomers better performance in their biological activity. As presented here, D-GL13K shows structural differences in comparison with the GL13K at the interface, that could be translated to the

biological context with an interfacial mechanism of action. Studies have shown that membrane-bound peptide to lipid ratios around 1/10 are necessary to permeabilize the membranes but this corresponds to practically full membrane coverage, leading to leakage by other factors not specific to direct membrane permeabilization. Normally, membrane disruption is evaluated with vesicle leakage experiments performed at peptide-to-lipid ratios that do not allow comparisons with those in biological assays and hardly explain the interaction (63, 64). Wimley (63) proposed the interfacial activity model that can be expressed through experimentally testable predictions:. This model will probably best characterize peptides such as D-GL13K and L-GL13K because some of the predicted features are already observed in them. GL13K enantiomers are interfacially active peptides, that can partition into the membrane interface and cause local perturbations of lipid moieties due to their particular amphipathic arrangement (63).

3.2. Preliminary characterization of GL28K peptidomimetic

The newly designed peptide GL28K (GKIIKLKASLKLV-$P_{(D)}$-PTKIIKLKASLKLL-NH_2) is represented in Figure 3.9, showing the proposed β-turn generated by the D-Pro/L-Pro (P_DP_L) motif. By creating a peptide that can create an intra- rather than intermolecular β-sheet, it was anticipated that the concentration of peptide required to generate antibacterial activity would be lowered. The antibacterial activity was evaluated as a proof of concept and performed with a microdilution antimicrobial assay against *E. coli* ATCC 25922 (167). The peptide rendered a suitable MIC of 12.5 μg/mL or 4.1 μM against this reference Gram-negative bacteria. GL28K shows therefore suitable antibacterial activity in the exploratory testing, with an MIC value in the range of those reported for GL13K against a variety of Gram-negative bacteria (Refer to Table 1.1). Clearly the MIC values are not comparable unless performed under standard testing conditions for the bacterial strains, but it is mentioned as a reference for context.

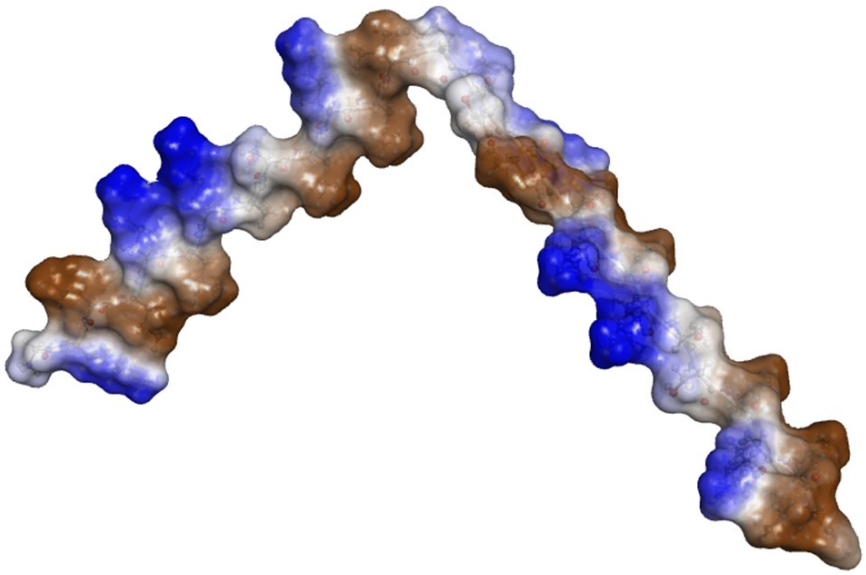

Figure 3.9. Surface representation of the GL28K peptide as β-strand constructed with Accelrys Discovery Studio software (v4.1). The hydrophobic surface is shown in brown whereas the hydrophilic moieties of polar sidechains are shown in blue.

We performed a preliminary biophysical evaluation of the peptides intended to identify similarities to GL13K or structural features that could render useful for further biological activity characterizations. Initially, the peptides were injected into the subphase under the monolayers at 30 mN/m to evaluate the peptide insertion based on membrane compositional differences (Figure 3.10). The insertion of the GL28K in the bacterial models occurs in similar fashion to the profiles of D- and L-GL13K, with the membrane having a higher negative charge yielding slightly sharper early surface pressure changes but stabilizing at longer timeframes at approximately the same level for both models. The sharper initial insertion in the more anionic model suggests that the initial binding step is analogous to that of GL13K, but no further structural assumption can be drawn.

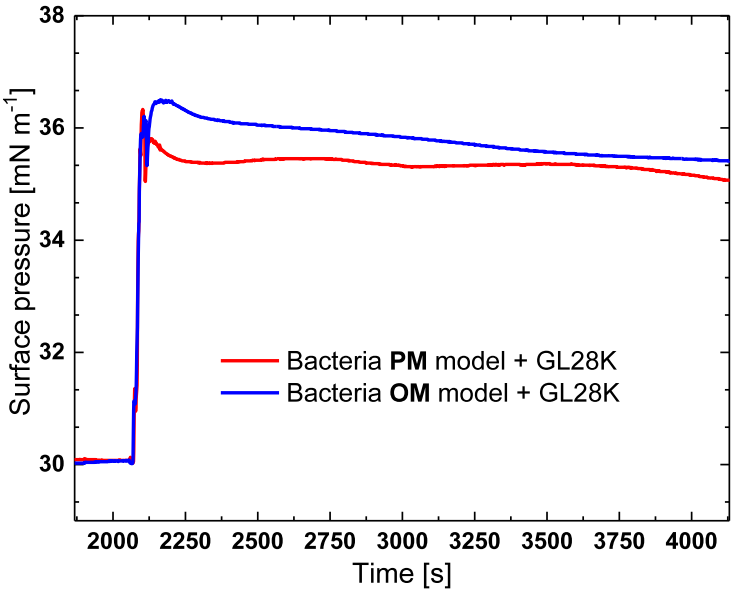

Figure 3.10. Insertion of GL28K enantiomers in monolayers of the bacterial models. Red lines correspond to the PM model (DOPE/DOPG/CL 15/80/5) and blue lines to the OM model (DOPE/DOPG/CL 75/20/5). The monolayers were formed by spreading the lipid mixtures on PBS subphase to render initial surface pressures of 30 mN/m, mimicking naturally occurring membranes. GL28K at 10.1 µM was introduced into the subphase and changes in surface pressure monitored.

Circular dichroism was performed to monitor the secondary structure in the presence and absence of the bacterial model membranes. The mean residue ellipticity for the GL28K peptide is presented in Figure 3.11, with the peptide interacting with the bacterial outer membrane model on the left and the plasma/inner membrane model on the right. Our results show the presence of the β-sheet conformation in a similar fashion to the reports of Sinthuvanich *et al.* and Reid *et al.* (123, 126) in presence of the bacterial model membranes. The mean residue ellipticity between minima at 218 – 222 nm at the different peptides to lipid ratios confirm the β-sheet structure. Even though, GL28K has a different sequence to SVS-1 (original peptide sequence reporting the role of the D-Pro/L-Pro motif), the spectra confirm that the secondary structure intended for activity is achieved. Additionally, the spectra indicate that GL28K remains unfolded or in random coil conformation in PBS solution. Therefore, the presence of the membrane environment is required for the conformational change and the putative activity.

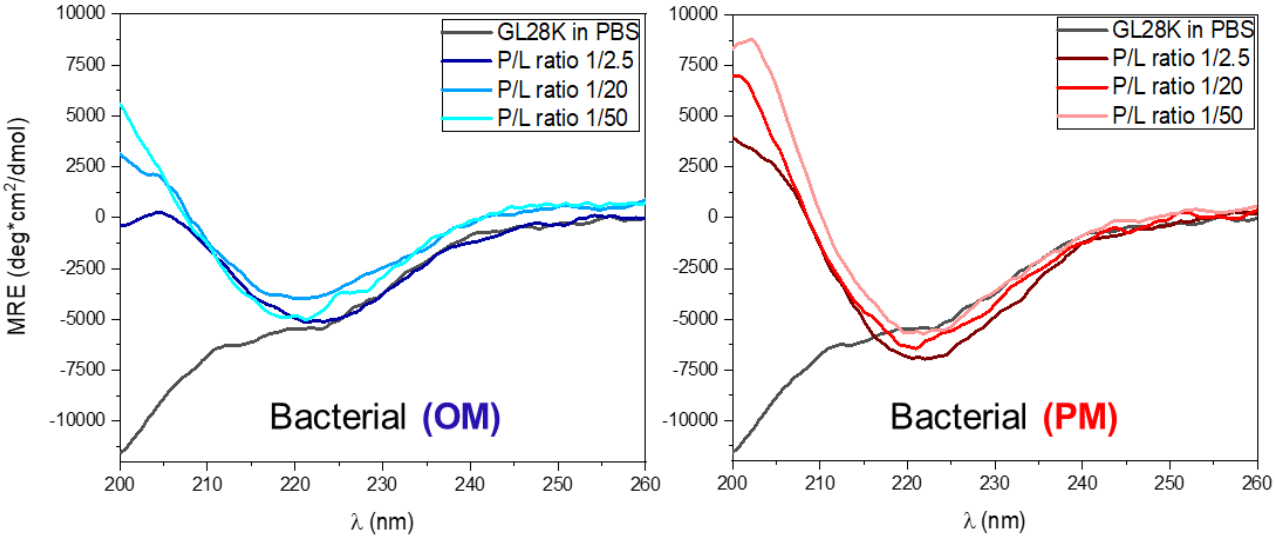

Figure 3.11. CD spectra of GL28K in presence of LUVs mimicking bacterial membranes at different P/L molar ratios. Left spectra correspond to the OM model (DOPE/DOPG/CL 75/20/5) and right to the PM model (DOPE/DOPG/CL 15/80/5). The experiments were performed at a peptide concentration of 15 µM in physiological conditions (PBS buffer, pH 7.4) in presence and absence of liposomes to monitor the change of secondary structure.

However, as observed for L-GL13K the presence of the secondary structure in these bulk studies does not confirm that it is present at the interface. Therefore, we performed PM-IRRAS studies with the GL28K in situ with the DOPE/DOPG/CL (75/20/5) and DOPE/DOPG/CL (15/80/5) models. The resulting spectra for GL28K are presented in Figure 3.12, displaying the Amide I band split into a very intense positive band at 1620 cm^{-1} (Amide BI) and a weak positive band ~1690 cm^{-1} (Amide BI'). This confirms, along with the marked amide II band absorbing at ~the 1540 cm^{1} frequency, the arrangements of an extended antiparallel β-sheet formation. Since the Amide I sharpens and shifts to lower wavenumbers with increasing β-strands at the interface (143, 157), comparing this spectra to that of the GL13K enantiomers would allow the consideration that the turn introduced in GL28K indeed facilitates the partition to membranes.

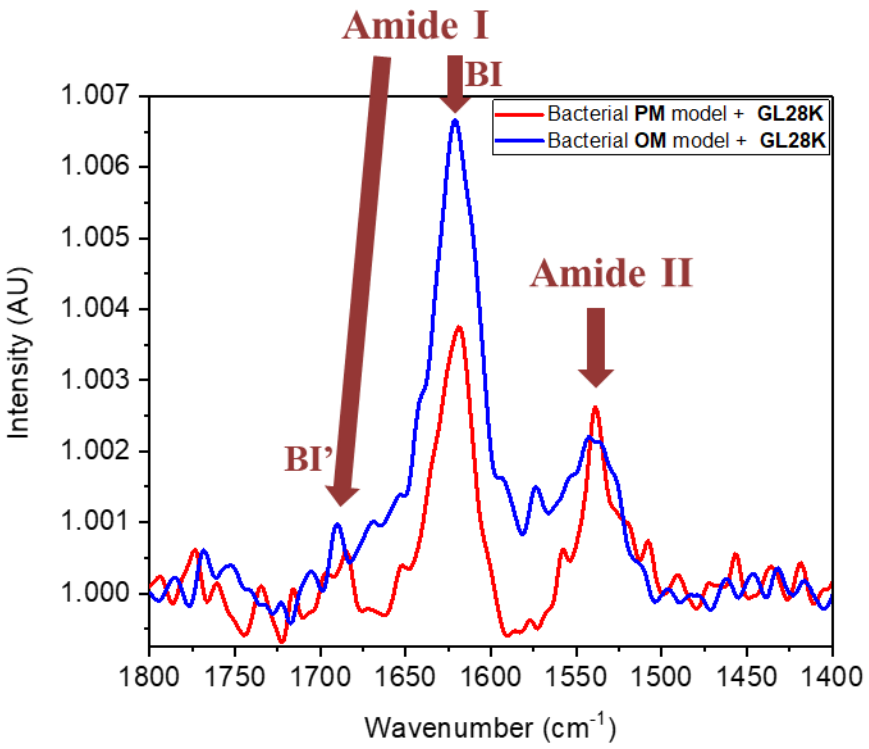

Figure 3.12. PM-IRRAS spectra of GL28K inserted into monolayers of bacterial model membranes at the air/buffer interface. The phospholipid mixtures were spread until reaching a monolayer lateral surface pressure of 30 mN/m on PBS, pH 7.4. GL28K at 10.1 µM was injected into the subphase and changes in surface pressure were monitored.

Considering the compositional differences between the models and analyzing the intensity of the amide I and II bands in the spectra for GL28K, it might seem that the peptide displays a folded state more stable (namely greater number of beta strands at the interface) in presence of the less charged model, however PM-IRRAs intensities are also highly dependent on orientation. Looking further to the intended purpose of GL28K (as an anticancer peptide), a stable secondary structure displayed at the interface is fundamental for interactions not driven solely by charge. However, further assessment must take place to determine the main structural parameters when the anticancer activity is evaluated.

Table 3.5. Orientation angles estimated from simulations reported by Blaudez *et al.* (143) for GL28K at the interface upon interaction with bacterial models.

Phospholipid composition in bacterial models	GL28K	
	Ψ	**θ**
(OM) DOPE/DOPG/CL 75/20/5	**45°**	**~40°**
(PM) DOPE/DOPG/CL 15/80/5	**0°**	**~70°**

As noted above, the orientation of the bands can provide information about the absorption transition moments that orient in the interface plane in PM-IRRAS. We estimated the orientation of GL28K peptide at the monolayer interface by comparing the intensity ratios to PM-IRRAS simulations reported by Blaudez et al. (140, 143) for β-sheet forming peptides. GL28K folds into a more planar orientation at the interface (Ψ≈0) when interacting with the membrane containing the higher proportion of negative phospholipids. In contrast, in presence of the less charged bacterial model the peptide adopts a slightly tilted orientation of (Ψ≈45°) with the carbonyls slightly tilted (θ angle ≈40°) above the interface plane. These minor orientational differences could play a role (the θ angle), as for example on the extent to which the defined folded structure of the peptide can be more stable. In this preliminary work, we show that GL28K presented antibacterial activity and a folded structure into β–sheets at the interface required for the activity as in the SVS-1 original sequence (123) . However, GL28K's full biological activity and the main structural parameters for the determined biological role must be further investigated.

Chapter 4. **Results and Discussion for anticancer activity**

4.1. Activity of GL13K peptidomimetics

Colorimetric viability assays were performed *in vitro* to evaluate the anticancer activity of GL13K peptides. The IC_{50} concentrations of the preliminary assessment for GL13K enantiomers against cancer cell lines and fibroblasts are represented in Table 4.1. Both D- and L-GL13K exhibited anticancer activity in H1299 human lung cancer cells and were unable to kill human fibroblasts. The results show therefore, that the action of the peptides is selective as neither enantiomer had an effect on the fibroblast cell line. Particularly D-GL13K showed greater effectiveness (lower IC_{50} values) at reducing the viability of cancer cells, in concordance with the results obtained against pathogenic bacteria (D-enantiomer presented lower MICs). The concentration at which this D-GL13K was innocuous towards the human fibroblasts was several times the MIC value required for its antibacterial activities *in vitro* (Refer to Table 4.1 and Table 1.1). Furthermore, only the D enantiomer presented selective toxicity against the triple negative MDA-MB-231 breast cancer line. These results represented a differential activity based on the peptide chirality.

Table 4.1. Concentration of GL13K peptides that killed or inhibited the growth of 50% of the cells (IC_{50})

Cell lines	IC_{50} (μM)	
	D-GL13K	**L-GL13K**
H1299 (human lung cancer)	36	112
MDA-MB-231 (human breast cancer)	90	>200
HFF (human fibroblasts)	>200	>200

Our results for the anticancer activity are higher that those reported for peptides of similar length and sequence as GL13K in MDA-MB-231 and other cell lines (123, 168), even though different assays and testing conditions are used. Analyzing the concentrations required for the biological action of GL13K enantiomers, the anticancer activity rendered IC_{50} values higher than the MICs required for the antibacterial function. The first one implying 50 percent lethality or inhibition of growth whereas the latter, full inhibition of growth. Experiment-guided *in silico* investigations

have shown that the increase in selectivity of membranolytic ACPs can come at the expense of a reduced anticancer activity (62, 79, 96). The low effective concentrations observed led to assess if factors such as the cell membrane environment and membrane composition are involved in these differences.

4.2. Interaction of GL13K peptidomimetics with eukaryotic model membranes

4.2.1. Role of membrane charge and packing

To start, the behaviour of the phospholipid compositions involved in the selected model membranes was analyzed. The surface pressure-area isotherms for the monolayers composed of phospholipid mixtures representing the outer leaflet of both RBC (DOPC/DOPE/SM/Chol 25/25/37.5/12.5) and cancer DOPC/DOPE/SM/Chol/DOPS 20/20/30/10/20 cell membranes are presented in Figure 4.1. The monolayers were stable and appear to comprise a liquid expanded phase or a coexistence of liquid expanded and condensed or liquid-ordered phases. The isotherms show smaller lateral molecular areas for the RBC mixtures compared to the cancer model in either water or PBS subphase, but the collapse pressures were similar for both films. The more expanded cancer cell membrane may be a result of the smaller proportion of cholesterol, greater charge repulsion with the anionic DOPS or through the alterations of lipid rafts. The greater ionic content of the PBS subphase led to greater molecular areas per lipid molecule in both systems, likely associated with intercalation of counterions in the headgroup region.

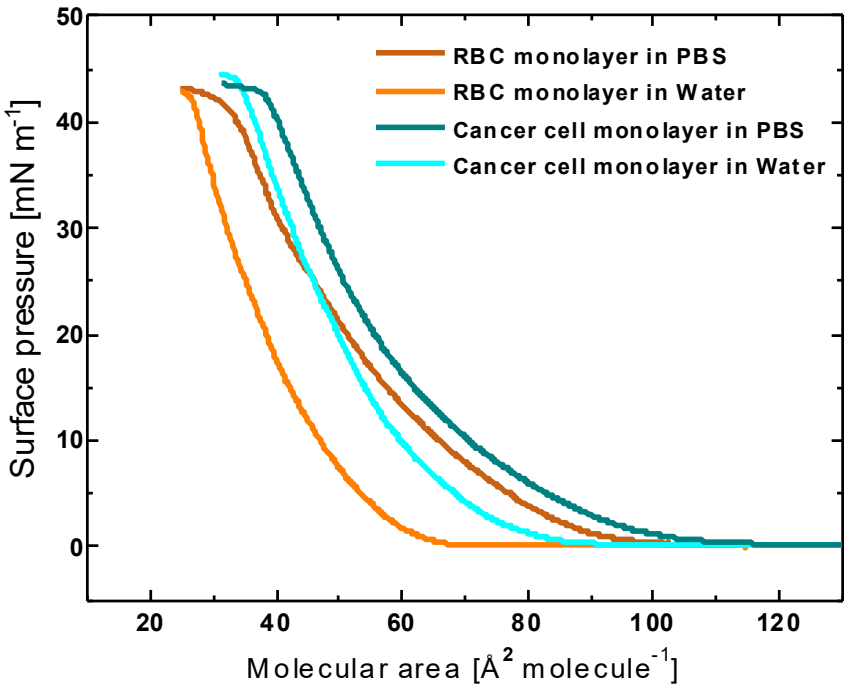

Figure 4.1. Surface pressure-area isotherms of the lipid mixtures representing the outer leaflet of both the RBC (DOPC/DOPE/SM/Chol 25/25/37.5/12.5) and the cancer (DOPC/DOPE/SM/Chol/DOPS 20/20/30/10/20) cell membranes in water and PBS buffer pH 7.4.

In order to evaluate the morphology of the monolayers, AFM imaging was performed on films deposited onto mica using a Langmuir-Blodgett deposition. The topology images (Figure 4.2) showed that the phospholipid mixtures representing both RBC and cancer membrane outer leaflets formed mixed-phase monolayers. Both eukaryotic membrane models formed domains of approximately 100 nm to 500 nm in diameter. However, the cancer cell model membrane also exhibited larger domains (~6 μm in diameter) that were not present in the RBC monolayers (the largest slightly greater than 1 μm). The average height differences between the fluid Ld phase (darker background in Figure 4.2 and the brighter Lo or condensed phase domains of the RBC and cancer models are 4.7 ± 0.3 Å and 7.4 ± 0.7 Å, respectively. The greater height difference in the cancer monolayer suggests that the domains correspond to condensed phase domains in which the phospholipids are highly ordered (untitled or tilted), whereas the lower values in the RBC model can be attributed to less packed domains in Lo phase. The range of height differences for Ld-Lo phases are typically between 0.8 - 1.0 nm (8 - 1.0 Å) for supported lipid bilayer of similar compositions (DOPC/SM/Chol) (169, 170). Considering that we are using monolayers, the difference should be then theoretically half, corresponding to approximately 4-5. Å. In general, the

height difference between Ld to Lo is lower than that of Ld-Condensed phase for similar systems. It was determined that the distance between Ld and the Ld-Condensed ordered phase is ≈ 8 Å and between 4 and 5 Å for Ld-Lo in studies with detergent resistant membranes or rafts of similar composition, (171). Our results match well with the values reported.

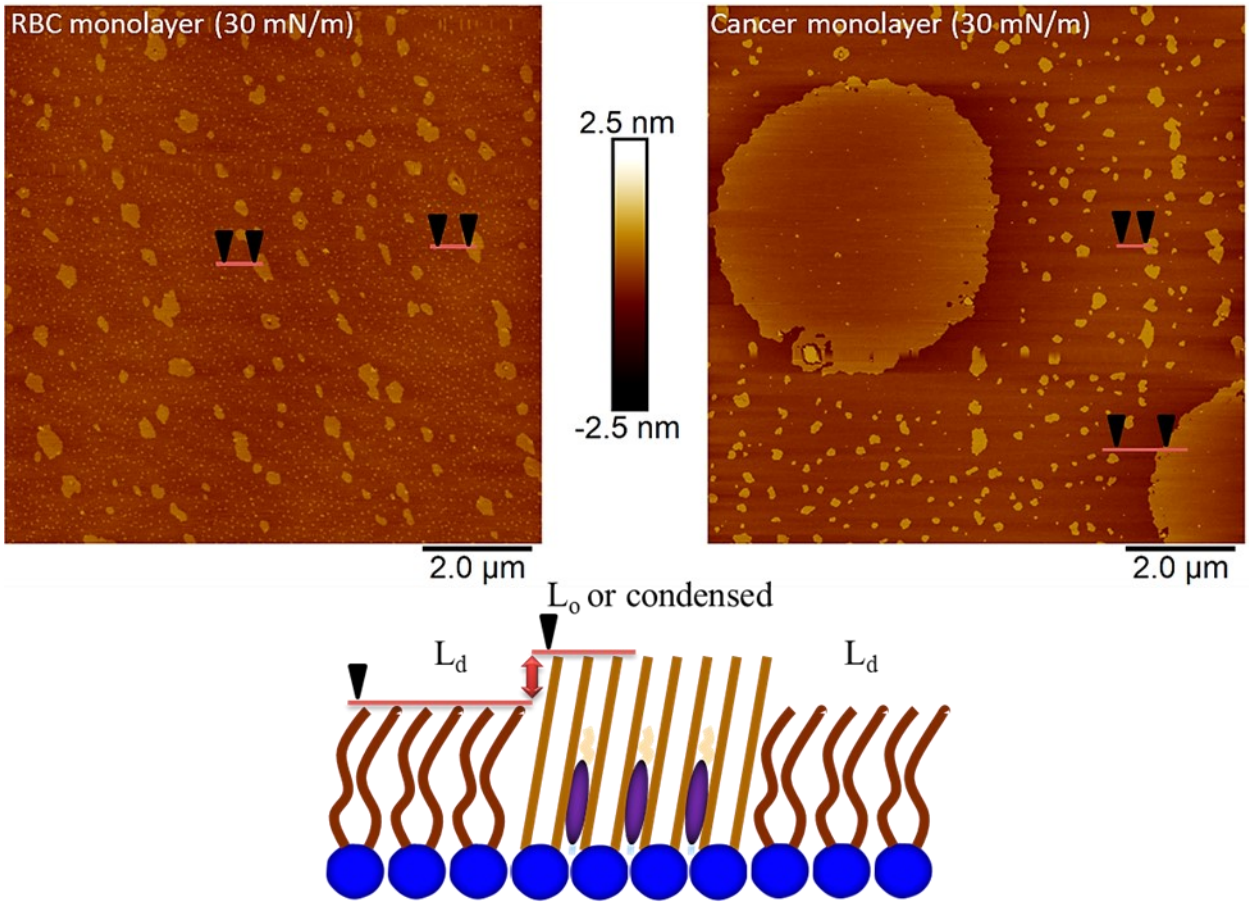

Figure 4.2. AFM images of monolayers mimicking outer leaflet of RBC and cancer cell membranes deposited on mica at 30 mN/m. A schematic with a molecular representation of the lines in the images is depicted on the bottom. The monolayers were formed by compressing the phospholipid mixtures spread on PBS in a Langmuir trough until reaching 30 mN/m of surface pressure. The hydrophilic mica insert was withdrawn keeping the polar headgroups attached while the acyl chains faced the air.

Phase diagram analysis for ternary mixtures of DOPC/SM/Chol show that the compositions employed are close to the phase boundaries between two coexisting liquid phases (Ld-Lo) and a coexisting Solid and Liquid phases (Ld-condensed) (172, 173). Considering that we have three dioleoyl-phospholipids in the mixtures and not purely DOPC in the model, the phase boundary

could be slightly shifted such that the change from the RBC (DO-phospholipids/SM/Chol 50/37.5/12.50) composition to the cancer model composition (DO-phospholipids/SM/Chol 60/30/10) could induce a transition from the Lo to condensed phase.

We should now consider the implications on the action of the GL13K enantiomers. The peptides were injected in the subphase after spreading the monolayers at biological surface pressures of 30 mN/m for an initial evaluation of the effect of peptide chirality and membrane charge on the membrane insertion. Both, membrane charge and GL13K chirality, affected the peptide insertion in the monolayers, as presented in Figure 4.3. Insertion into the cancer cell membrane was greater for both peptides, evidenced by the greater change in surface pressure. The cancer cell model membrane has a comparable anionic lipid content to the bacterial OM model membrane (20 and 25%, respectively) and both exhibit similar surface pressure changes and insertion profiles upon injection of the peptide (Figure 4.3 and Figure 3.2), highlighting the importance of charge as a driving force component for the insertion. In contrast to the bacterial model membranes, a distinct impact of chirality is observed with these insertion experiments, namely greater insertion was always observed with D-GL13K for both model membranes (to be discussed later). These results are impactful considering that no proteases or external factors other than the molecules of interest were included in the study.

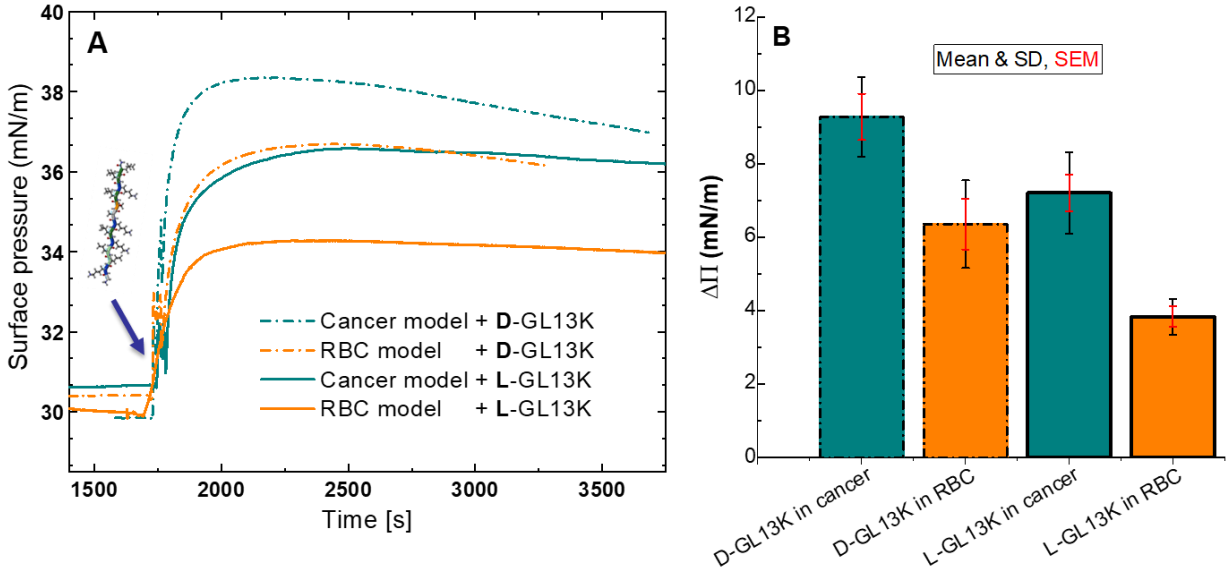

Figure 4.3. Interaction of GL13K enantiomers with monolayers of erythrocytes (orange) and cancer cells (dark cyan) model membranes. In all cases, the monolayers were formed by spreading the phospholipid mixtures onto an aqueous subphase to give an initial surface pressure of 30 mN/m, mimicking naturally occurring

membranes. D-GL13K (dashed lines) and L-GL13K (solid lines) at 10 μM were then introduced into the subphase: (A) changes in surface pressure monitored as a function of time where the arrow indicates injection for the peptide under a stable monolayer and (B) mean change in surface pressure (ΔΠ) at 8 min after insertion of the peptides (n=3-5) where black bars represent the standard deviation (SD) and red bars the standard error of the mean (SEM).

The results of the membrane permeability experiment as a measurement of the dye release are included in the figure below (Figure 4.4). They are no clear differences of the effect of the peptides but the D-GL13K leads to greater membrane disruption of the cancer model vesicles at the two highest P/L ratios (left). This could be due to an effective peptide concentration level at the liposome surface considering that the lowest P to L ratio had the opposite outcome.

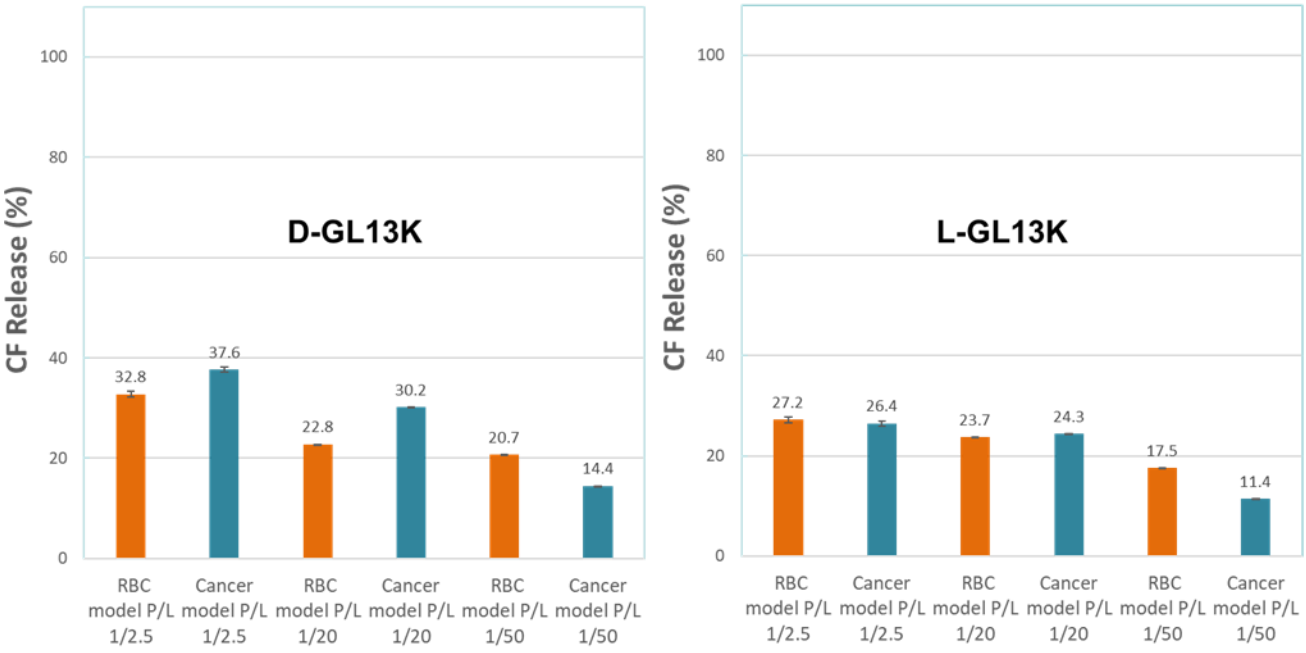

Figure 4.4. Disruption of the liposomes containing human cell model membranes by GL13K enantiomers at three peptide/lipid ratios (D-GL13K on the left and L-GL13K on the right). RBC model (DOPC/DOPE/SM/Chol 25/25/37.5/12.5) is shown in orange and the cancer model (DOPC/DOPE/SM/Chol 20/20/30/10/20) in aqua.

4.2.2. Peptide structural changes and role of peptide chirality

The structural transition was first evaluated with circular dichroism (CD). The mean residue ellipticities obtained from circular dichroism for GL13K enantiomers in solution (PBS) and with liposomes of RBC and cancer model membranes is displayed in Figure 4.5.

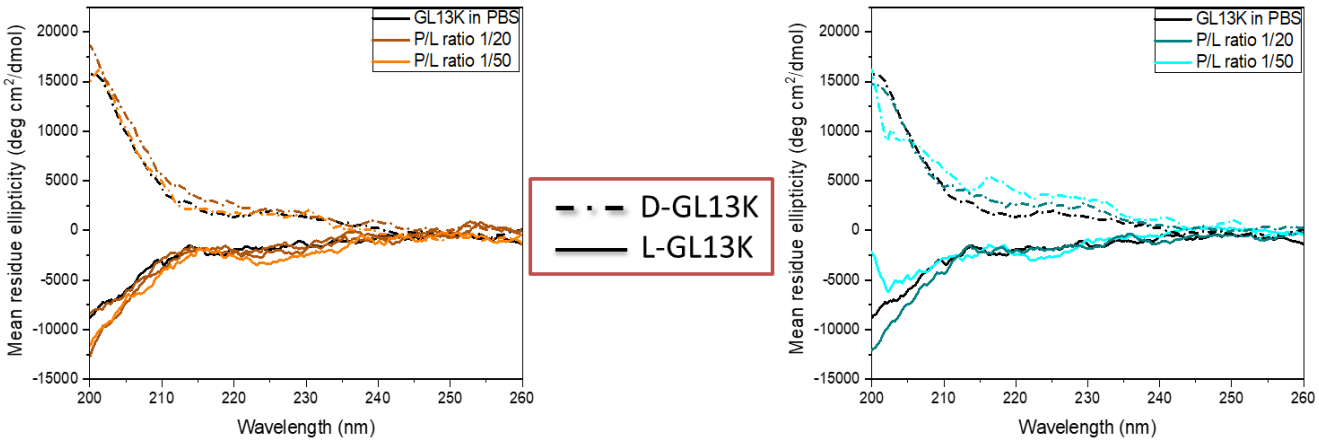

Figure 4.5. CD spectra of GL13K enantiomers in presence of liposomes representing erythrocytes (left) and cancer cells (right) model membranes at two P/L molar ratios. The experiments were performed in physiological conditions (PBS: 10 mM phosphate, 137 mM NaCl, pH 7.4) in presence and absence of liposomes to monitor the change of secondary structure. Both, D-GL13K (dashed lines) and L-GL13K (solid lines), at 15 µM displayed random coil conformations.

As observed, there were no clear ellipticity differences between the peptide in solution and the peptide in presence of the model membranes from the mammalian cells. Interestingly, if a conformational change occurs, CD as a bulk technique was not able to detect it. CD titrations of 60 µM GL13K have been reported to show a gradual shift from random coil to more β-sheet secondary structures with increasing pH 8.5 - 10.6 in 10 mM Tris-HCl buffer solutions in the absence of the lipid membrane(109). Similarly, this transition was observed for both enantiomers at 100 µM with increasing time in borax-NaOH buffer between pH values of 9.6 - 10.4, again in the absence of a lipid membrane (165). It is notable that despite showing comparable insertion profiles to the bacterial OM model (Chapter 3.2.2), there is no evidence of a secondary structure transformation under these physiological conditions.

Considering the higher concentrations required for activity against cancer cells compared to bacteria, it may be that the proportion of GL13K which partitions to the membrane is smaller. As

CD spectra are bulk measurements the signal may be dominated by the free peptide rather than the membrane bound peptide. PM-IRRAS is a surface sensitive technique which only reports on the secondary structure of peptide present at the membrane interface. Figure 4.6 shows the amide region of the spectra obtained for D- and L-GL13K in the presence of the cancer cell model membrane and RBC membranes, respectively.

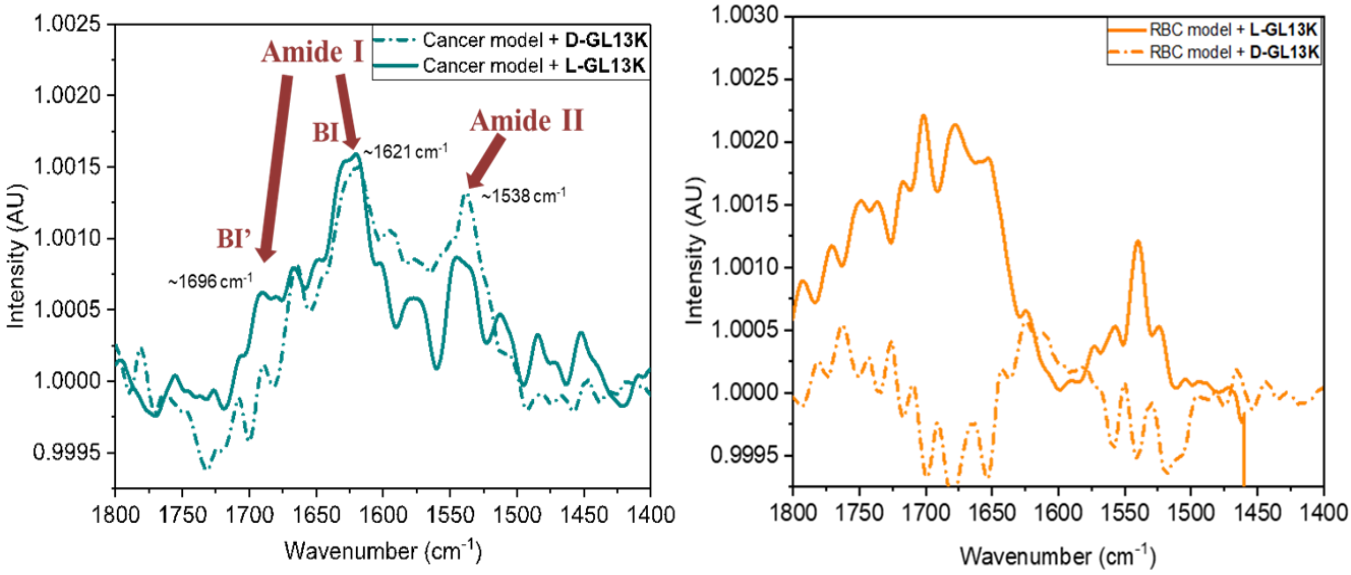

Figure 4.6. PM-IRRAS spectra for the amide regions upon insertion of GL13K enantiomers into monolayers of the cancer (left) and RBC membrane models (right) at a surface pressure of 30 mN/m.

For both enantiomers in the cancer model, the peptides adopt the typical antiparallel beta sheet conformation observed in bacterial models but with more background contribution. The spectra were characterized by the split in the amide I band frequencies and the positive band at ~1540 of the amide II vibration. Insertion of the peptides in the RBC model under the same conditions does not show the typical amide bands corresponding to the β-sheet conformation. The D-enantiomer in the RBC model presents very weak contributions of the amide I at ~1623 cm^{-1} and the amide II at ~1532 cm^{-1} and at the moment a coherent interpretation of this spectrum cannot be provided. However, L-GL13K could be either transitioning to a beta sheet structure or folding into a different structure such as β–turns or α-helix because other positive bands formed between 1650 and 1690 cm^{-1} and the contribution of the amide II at ~1540 cm^{-1} (174). The orientation of the peptides in situ at the with the cancer monolayer is presented in Table 4.2 and obtained comparing

the intensity ratios of the spectra to PM-IRRAS simulations reported by Blaudez et al. (140, 143). The enantiomers present no clear differences in their orientations at the interface.

The takeaway from these results is that the peptides interact differently at the interface depending on the target membrane composition as observed between the normal cell and the cancer cell model membranes.

Table 4.2.Orientation angles estimated from simulations reported by Blaudez *et al.* (143) for GL13K enantiomers at the interface with the cancer model.

Phospholipid composition in bacterial models	D-GL13K		L-GL13K	
	Ψ	θ	Ψ	θ
DOPC/DOPE/SM/Chol/DOPS 20/20/30/10/20	45°	~35°	45°	~50°

Using GIXD to assess the crystallinity of the peptides or the lipid ordering, revealed interesting results. No Bragg peaks (Figure 4.7) corresponding to a β-sheet conformation (at ~1.32 in Q_{xy}) were observed before or after peptide upon insertion at 5 μM in the mammalian monolayers, in contrast to the crystalline beta-sheet structures occurring in presence of the bacterial models with defining Bragg peaks. This could occur due to a more ordered or condensed phase domain of the lipids in the mammalian models, as observed in AFM results. Notably, Bragg peaks consistent with lipid crystallites were not observed for the cancer model. Transient peaks descriptive of this crystalline structure appeared in frames of the contour plots for both the RBC and cancer model membranes. Most probably the distinct beta-sheet conformation observed at the interface with PM-IRRAS is not crystalline or abundant enough to produce a Bragg peak. Higher concentration of the peptides may be needed for the formation of a β-sheet crystalline conformation attending to higher IC_{50} values. In more recent GIXD experiments, D-GL13K at 20 μM seems to generate Bragg peaks corresponding to crystalline β-sheets but only in the presence of the cancer model. Further analysis is required to be conclusive.

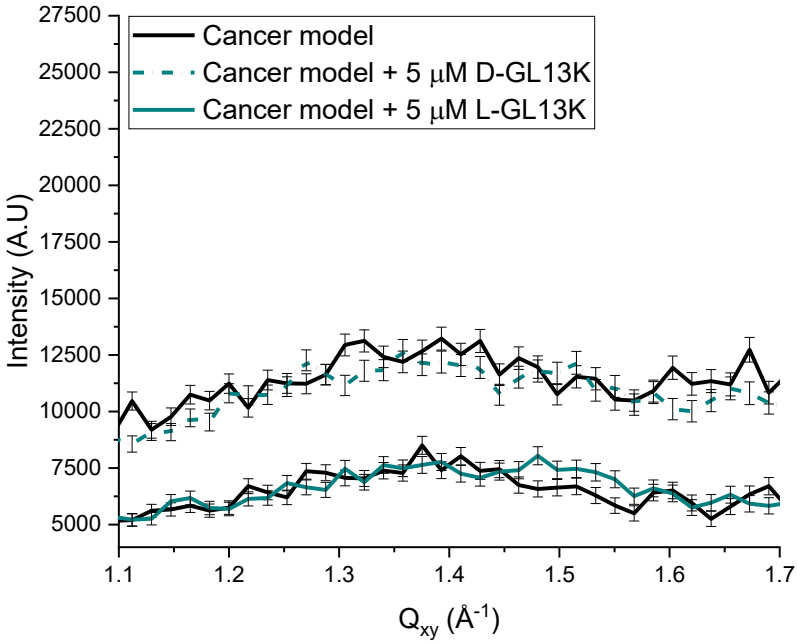

Figure 4.7. Bragg peaks curves obtained from GIXD for GL13K enantiomers in interaction with cancer model monolayers at the air/buffer interface, before and after peptide injection. The monolayers with the lipid mixtures were spread until reaching a surface pressure of 30 mN/m on PBS, pH 7.4. D-GL13K (dashed lines) and L-GL13K (solid lines) were inserted in the subphase underneath at 5 µM and 10 µM. Only the data of the peptides at 5 µM is represented.

Further to the secondary structure and orientation of the GL13K enantiomers in eukaryotic models, we analyzed the electron densities normal to the surface through fitting the XRR data. The data for the models in absence and presence of the peptides is shown in Figure 4.8, with the fits and raw normalized reflectivity in parts A and B, and the corresponding electron density profiles in part C and D. Table 4.3 shows the fitting parameters for the electron density profiles of these models.

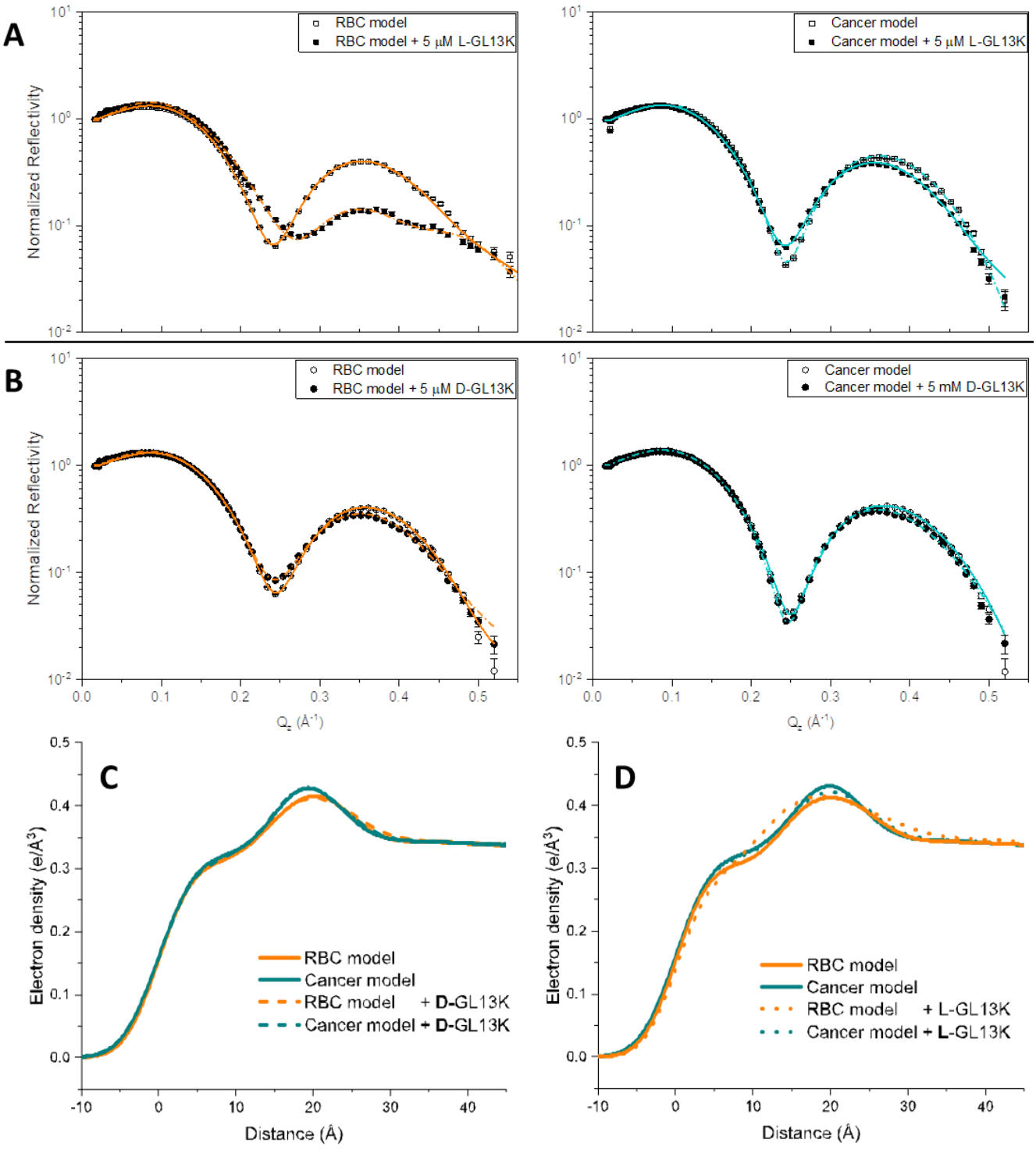

Figure 4.8. Reflectivity data (A and B) and electron density profiles (C and D) of eukaryotic monolayer models in the absence and presence of the peptides at the interface. The monolayers were spread until reaching a constant surface pressure of 30 mN/m on PBS. GL13K enantiomers were injected into the subphase at 5 μM. Solid lines correspond to the fits of phospholipid monolayers (Orange and cyan for RBC and cancer models respectively) whereas interrupted lines correspond to fits after the peptide injection.

For most eukaryotic systems, there was no considerable change in the reflectivity data nor in the electron density profiles upon the injection of the peptides, when compared to the clear differences presented with the bacterial models. In the case of the RBC model with L-GL13K, an artifact may have occurred considering that the reflectivity data did not patch well; probably the monolayer burnt upon prolonged XR exposure or the distribution of the peptide in the footprint was not homogeneous at 5 μM. This system (RBC model with the L-GL13K) could not be repeated in other experiments at the Synchrotron.It has been reported that cholesterol causes minor elongations of the region corresponding to the acyl chain of the monolayer and a broadening of the headgroup region. It also lowers the electron density of the headgroup region while increasing the electron density of the chains (175).

Attending to the thickness of the films (Table 4.3), we obtained values comparable to lipid microdomains on top of lipid raft patches and nearly half of the thickness of membranes patches of lipid rafts isolated from MDA-MB-231 human breast cancer cells (same cell line used for anticancer activity evaluation) (176). This supports the selection of our cancer model and our fitting parameters in terms of the vertical distances obtained.

Table 4.3. Fitting parameters for x-ray reflectivity data of eukaryotic models at the interface upon interaction with GL13K enantiomers. Electron density (ρ), thickness (d) and roughness (σ) values are presented for each layer/slab in all systems. Numbering of the slabs is made in the direction air to subphase.

System	Slab 1			Slab 2			Slab 3			χ^2	Film thickness (d_{Slab1} + d_{Slab2})
	d (Å)	ρ ($e^-/Å^3$)	σ (Å)	d (Å)	ρ ($e^-/Å^3$)	σ (Å)	d (Å)	ρ ($e^-/Å^3$)	σ (Å)		
RBC (DOPC/DOPE/SM/Chol 25/25/37.5/12.5)	14.2	0.31	3.55	10.9	0.42	2.9	14.0	0.34	2.99	15	25.1
RBC (DOPC/DOPE/SM/Chol 25/25/37.5/12.5) + **5 uM D-GL13K**	14.3	0.313	3.78	10.9	0.427	3.86	15.4	3.344	3.471	22	25.2
Cancer DOPC/DOPE/SM/Chol/DOPS 20/20/30/10/20)	15.5	0.317	3.54	7.2	0.475	3.9	17.3	0.344	3.37	13.6	22.7
Cancer DOPC/DOPE/SM/Chol/DOPS 20/20/30/10/20) **+ 5 uM D-GL13K**	15.3	0.315	3.65	7.6	0.468	4.14	17.0	0.339	4.14	14	22.9
RBC (DOPC/DOPE/SM/Chol 25/25/37.5/12.5)	13.8	0.302	3.32	12	0.42	3.56	16.9	0.342	2.47	25	25.8
RBC (DOPC/DOPE/SM/Chol 25/25/37.5/12.5) **+ 5 uM L-GL13K**	11.4	0.305	3.28	14.6	0.416	5	15.8	0.347	2.98	44	25.9
Cancer DOPC/DOPE/SM/Chol/DOPS 20/20/30/10/20)	14.7	0.314	3.42	9.4	0.448	3.74	17.3	0.343	3.36	35	24.1
Cancer DOPC/DOPE/SM/Chol/DOPS 20/20/30/10/20) **+ 5 uM L-GL13K**	15.1	0.313	3.88	8.8	0.454	4.44	17.0	0.343	3.05	23	23.9

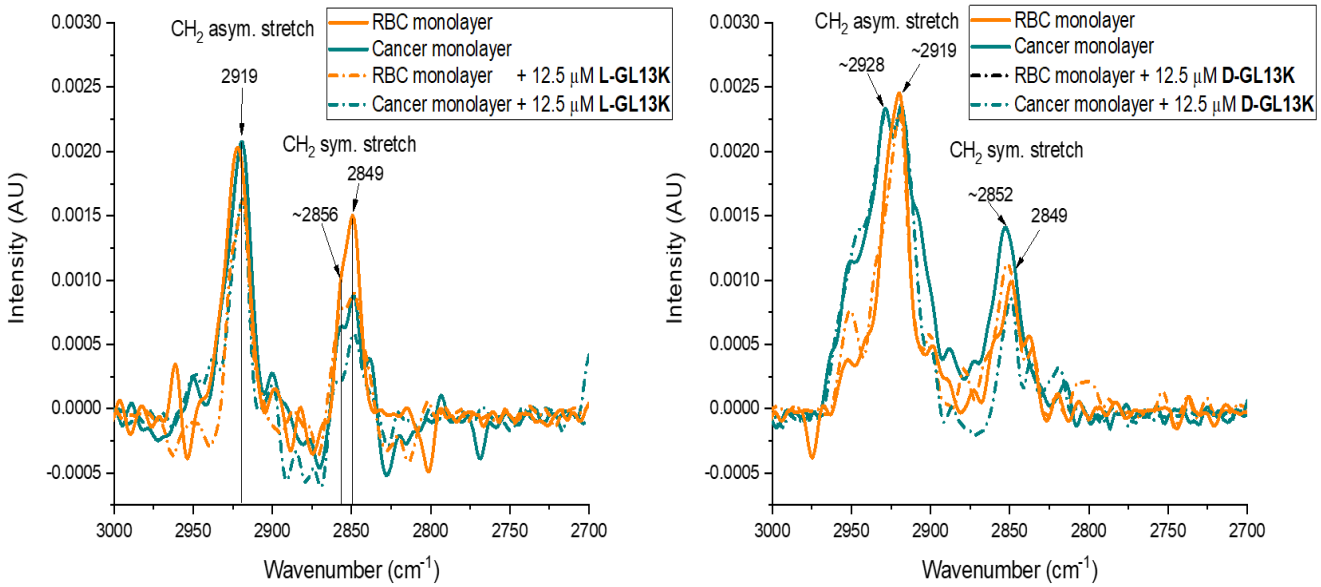

Figure 4.9. PM-IRRAS spectra for the asymmetric and symmetric CH_2 stretching upon insertion of GL13K enantiomers into monolayers of the RBC and cancer membrane models at a surface pressure of 30 mN/m. Left spectra correspond L-GL13K and right spectra to D- GL13K.

The lipid acyl chain region of the phospholipid mixtures in the PM-IRRAS spectra can be used to probe any differences in lipid ordering at the interface (Figure 4.9). The frequencies of the methylene stretching vibrations are used to characterize the conformational order or disorder in chain amphiphiles. The asymmetrical stretching band for the lipid chains of the RBC model before and after the peptide insertion of both enantiomers remains at a frequency of 2919 cm^{-1}, indicative of a liquid ordered or condensed phase. When looking at the CH_2 symmetrical stretching, the wavenumber remained at ~2849 cm^{-1} for RBC model but the presence of the D-GL13K caused a small shift ~2851 cm^{-1} generating perhaps a transient liquid ordered state. In the case of the cancer monolayer, the CH_2 asymmetrical and symmetrical stretching peaks were mostly at ~2819 $cm^{-1}$and ~2849 cm^{-1}, respectively, confirming the liquid ordered phase. However, the presence of shoulders and second peaks at higher wavenumbers could indicate coexistence with a less ordered liquid phase or a transition states or loss (temporary) of the liquid ordered phases. Additionally, the effect of the peptides on the loss of intensity was more pronounced in the cancer model. The interpretation of these results can be complex and lead to speculations on the effect of the peptides on the lipid chains but the in general confirms the presence of the Lo and/or condensed phase in our models

It is known that greater packing of membrane phospholipids hinders the insertion and penetration of AMPs/ACPs. As mentioned before, other membrane components can increase the compacting of the cellular surface creating denser lipid rafts. AMPs/ACPs may require higher concentrations to be effective in the actual cellular environment of tumoral cells to disrupt a more compact barrier compared to bacterial cell walls. In agreement, the lytic effect in eukaryotic cell-model membranes has been previously attributed to the exclusion of the peptides from ordered rafts (Lo regions) instead of specific peptide-lipid interactions (75). For similar systems, based of POPC, SM and Chol, increasing amounts of SM and Chol caused a phase boundary cross in the system leading to a Lo phase. After that, the δ-lysin peptides concentrated in the Ld phase domains, and self-associate, binding poorly or being excluded from Lo regions. The permeabilization of SM/Chol/POPC lipid vesicles with ≤ 60 mol % POPC by δ-lysin, was faster than the other compositions, though the full fractional dye release was reach at compositions of ≥ 40 mol % POPC (75). It is indicated that peptide exclusion from Lo regions is important for antimicrobial and cytolytic peptides that require self-association as it promotes peptide concentration in other membrane regions (75). The same principle applied to a 36-residue peptide from bacteriorhodopsin that partitions preferentially into the DOPC Ld phase relative to SM/Chol 50/50 % Lo phase (171).

On the other hand, mechanisms driven by the reduction of the line tension have been described for other AMPs/ACPs (protegrin-1, aurein- 1.1, dermaseptin-1, human b-defensin-1, histatin-2, indolicidin, magainin-1, caerin-1.3, citropin-1.1, kalata-B3, and pardaxin-1) that seem to present line-active behavior not driven by the overall membrane charge (177). In these mechanisms, the peptides preferentially accumulate at phase boundaries where there is an excess free energy (line tension). The excess free energy or line tension will be greater at the boundary of the liquid expanded-condensed phases which present significantly different order parameters and height difference compared to the liquid expanded – liquid ordered phases. Independently of the charge, interfacial line activity responds to the peptide concentration and the phase of the membrane domains. This may also contribute to the difference in insertion observed for the RBC and cancer cell models. Moreover, cholesterol content in the mixtures is important in this transitions when present between 10 -16 %, leading to transient or sensible zones of phase coexistence between the two liquid (ordered and disordered) phases and the solid ordered phase (46, 172, 173). This leads to variability of the line tension (height differences), which can help understanding or explaining

the preferential insertion and slightly higher dye release of the beta-sheet-structured D-GL13K in the cancer model membrane over the RBC model.

Chapter 5. **Conclusions and Future Work**

This thesis builds on prior work on the mechanism of action of GL13K with model membranes by introducing more complexity into the composition of the model membranes. This enables a better assessment of the role of membrane surface charge density and specific lipid chemical structures. Beyond improving the model membranes to better reflect the compositional differences between different cells and membrane (inner and outer) types, this thesis revolves around three central themes: the anticancer potential of GL13K peptides and the mechanistic differences between their mode of action on bacterial and cancer cell membranes; the influence of peptide chirality on peptide activity and interaction; and the preliminary assessment of a new peptide based on the original GL13K sequence.

The membranes of both bacterial cells and some cancer cells are rich in anionic lipids which are long thought to be a major target for AMPs and ACPs. Yet simple charge effects alone cannot account for the activity of these peptides. Moreover, their mechanism of action differs as a function of peptide chemical structure (in this thesis, chirality) and specific membrane composition. In this work, we have demonstrated that there are different mechanisms at play upon interaction of GL13K enantiomers with either bacterial or eukaryotic membranes, supported by both our model membrane results and differential potency. The major driving force for interaction of GL13K with the bacterial model membranes does appear to be membrane charge, as a higher surface charge changes the insertion profile and increases the kinetics of interaction. On the other hand, the specific lipids carrying that charge also appear to play a role, since both the bacterial outer membrane and cancer cell models, with comparable surface charges, result in different interactions with the peptides. Specifically, in the case of bacterial membranes, despite the slightly lower charge, a conformational change to beta-sheets has been observed, while no significant beta-sheet formation is observed for the cancer cell model membranes. The latter correlates well with the higher concentrations needed for achieving a selective anticancer activity, i.e., a higher concentration of peptide is needed to observe similar results with the cancer cell model membranes. Concentration effects with the cancer cell membranes should be investigated further. Concentration drives adsorption to the cell surface but also peptide aggregation which is a key event in the membrane disruption process. It was this concept that led to our group's specific design for GL28K. By connecting two GL13K strands, theoretically, the concentration at which

the two could begin the transformation to crystalline beta-sheets should be lowered. This remains to be proven and will be assessed in future work. So far, our preliminary approach demonstrated that GL28K exhibits antibacterial activity against a Gram-negative bacterial strain at the level of that shown by D- GL13K.

In the case of the eukaryotic model membranes, a differential in interaction with the D- and L-enantiomers can be observed for eukaryotic membrane models which was not observed for bacterial membrane models. While this could be attributed to specific lipid interactions which are chiral dependent, as has been reported for kinase activity (178) and blood coagulation (179), it appears that lipid ordering and phase separation plays a role. It has been suggested that AMPs penetrate less into the membrane when lipids are more ordered and that this may be a function of cholesterol content. As was discussed in chapter 4, the content of cholesterol and sphingomyelin is extremely important in determining which and how many lipid phases are formed. The presence of domains adds another component governing the mechanism of interaction of the ACPs, namely a line-tension driven interaction wherein peptides preferentially bind or accumulate at domain boundaries. This property is highly dependent on the nature of the phases present, and the free energy (or line tension) at those boundaries. A better understanding of the phase diagrams for these complex systems and how those phases govern peptide-lipid interactions should be assessed in future studies.

GL13K enantiomers show a differential potency in their biological activity that is also reflected in the biophysical characterization of their interaction with relevant model membranes. The latter is supported by the IC_{50} values and preferential interaction of D-GL13K with the cancer model membrane over the RBC model (used as control and containing no anionic lipids). Beyond resistance mechanisms, the chiral nature of the peptide and molecular bases of phospholipids also influence the effectiveness in activity, something that has not been explored in depth in previous studies. Thus, an important outcome of this thesis is the finding that this difference in activity for the two peptide enantiomers cannot be solely attributed to peptide degradation and clearance since no proteases nor other mechanism of resistance towards cationic AMPs/ACPs were included. A full mechanistic interpretation of this intrinsic chiral specificity will require further investigation. However, by comparison to the bacterial model, it seems that the line tension factor may be more implicated in the chiral specificity than charge, which is non-specific. This may be due to the

chirality of the lipids themselves as either peptide enantiomer can interact with the lipids, hence further investigation will be needed (180).

We should also consider that PS phospholipid has a role in coagulation that is stereospecific in protein−lipid interactions and has implications in other steps of the cascade (179). Thus, further analysis should be performed on the interactions of DOPS and GL13K enantiomers to study if there is any modulation of the activity based on the chiral centers of DOPS or the presence of D- and L-amino acids in GL13K. Experiments using the non-natural enantiomer of DOPS may provide a means to test hypotheses on the relevance of the lipid chiral specificity. This would shed light on a clearer understanding of the chiral role of AMPs/ACPs-lipids binding interactions at a molecular level. Even though D-GL13K can overcome proteolytic degradation, other issues like poor bioavailability could potentially obstruct its progress and development as a novel anticancer or antibacterial agent, as has been shown for other AMPs/ACPs. None or very few membrane-active peptides have made it into the 'anticancer' pharmaceutical market so far. Therefore, a targeted drug delivery strategy is necessary to enhance its stability and half-life *in vivo*, and consequently its market potential. A prospective approach to answer the market needs could be the conjugation of GL13K enantiomers with chitosan polymers. Chitosan is bioavailable, pH-responsive and has evidenced antibacterial effects per se (181), which makes it even more suitable for a conjugated peptide-based antibiotic alternative. In addition, chitosan possesses an inherent cationic nature below its p*Ka* which facilitates targeting anionic surface molecules in bacteria and cancer cells. Grafting AMPs (e.g. dodecapeptide anoplin) to chitosan polymers has proved to minimize hemolysis while decreasing the MICs against Gram-positive and Gram-negative bacteria, therefore increasing the peptide selectivity (182). Considering the lower extracellular pH (~6.2-6.9) microenvironment of cancer cells (48, 49, 183, 184), an acid-cleavable hydrazone linkage between GL13K peptides and the chitosan skeleton could be used as a pH sensitive targeted delivery to further improve the selectivity and bioavailability of GL13K against tumors or malignant cells (185).

Contemplating as well the inversion of the proton gradient and hence, the intra and extracellular pH in cancer cells with respect to normal cells (49, 57, 183, 184), the change in GL13K secondary structure with a decrease in pH (~6.2-6.9) should be evaluated to better resemble the surrounding conditions of cancer and understand how it may affect the peptide folding. No previous study has

been performed for GL13K at pH below 7.4 neither in the absence or presence of model membranes.

In conclusion, in this work we have further investigated the mechanisms at play in the antimicrobial activity of GL13K and demonstrated its potential as an anticancer peptide. We have demonstrated a specific role, beyond resistance to proteolytic cleavage for peptide chirality and provided evidence that the GL13K motif can be used to design future AMPs/ACPs.

References

1. L. Howell, Ed., “Global risks 2013,” 8th Ed. (2014).

2. C. L. Ventola, The antibiotic resistance crisis: part 1: causes and threats. *P T* **40**, 277–283 (2015).

3. R. W. Steele, Managing infection in cancer patients and other immunocompromised children. *Ochsner J.* **12**, 202–210 (2012).

4. A. P. Johnson, Surveillance of antibiotic resistance. *Philos. Trans. R. Soc. B Biol. Sci.* **370**, 20140080 (2015).

5. J. O’Neill, Antimicrobial Resistance: Tackling a crisis for the health and wealth of nations. *Rev. Antimicrob. Resist.*, 1–16 (2016).

6. T. P. Van Boeckel, *et al.*, Global trends in antimicrobial use in food animals. *Proc. Natl. Acad. Sci.* **112**, 5649–5654 (2015).

7. M. Zasloff, Antimicrobial peptides of multicellular organisms. *Nature* **415**, 389–395 (2002).

8. K. A. Brogden, Antimicrobial peptides: Pore formers or metabolic inhibitors in bacteria? *Nat. Rev. Microbiol.* **3**, 238–250 (2005).

9. N. B. da Cunha, *et al.*, The next generation of antimicrobial peptides (AMPs) as molecular therapeutic tools for the treatment of diseases with social and economic impacts. *Drug Discov. Today* **22**, 234–248 (2017).

10. A. C. Engler, *et al.*, Emerging trends in macromolecular antimicrobials to fight multi-drug-resistant infections. *Nano Today* **7**, 201–222 (2012).

11. S. Zhu, Evidence for myxobacterial origin of eukaryotic defensins. *Immunogenetics* **59**, 949–954 (2007).

12. M. Mahlapuu, J. Håkansson, L. Ringstad, C. Björn, Antimicrobial Peptides: An Emerging Category of Therapeutic Agents. *Front. Cell. Infect. Microbiol.* **6**, 194 (2016).

13. A. Giuliani, G. Pirri, S. F. Nicoletto, Antimicrobial peptides: An overview of a promising class of therapeutics. *Cent. Eur. J. Biol.* (2007) https:/doi.org/10.2478/s11535-007-0010-5.

14. P. Kumar, J. N. Kizhakkedathu, S. K. Straus, Antimicrobial Peptides: Diversity, Mechanism of Action and Strategies to Improve the Activity and Biocompatibility In Vivo. *Biomolecules* **8** (2018).

15. F. Schweizer, Cationic amphiphilic peptides with cancer-selective toxicity. *Eur J Pharmacol* **625**, 190–194 (2009).

16. D. Gaspar, A. S. Veiga, M. A. Castanho, From antimicrobial to anticancer peptides. A

review. *Front Microbiol* **4**, 294 (2013).

17. M. R. Felicio, O. N. Silva, S. Goncalves, N. C. Santos, O. L. Franco, Peptides with Dual Antimicrobial and Anticancer Activities. *Front Chem* **5**, 5 (2017).

18. P. Kosikowska, A. Lesner, Antimicrobial peptides (AMPs) as drug candidates: a patent review (2003–2015). *Expert Opin. Ther. Pat.* **26**, 689–702 (2016).

19. E. S. Olson, *et al.*, In vivo characterization of activatable cell penetrating peptides for targeting protease activity in cancer. *Integr. Biol. (Camb).* **1**, 382–393 (2009).

20. A. Peschel, H.-G. Sahl, The co-evolution of host cationic antimicrobial peptides and microbial resistance. *Nat. Rev. Microbiol.* **4**, 529 (2006).

21. J. M. A. Blair, M. A. Webber, A. J. Baylay, D. O. Ogbolu, L. J. V Piddock, Molecular mechanisms of antibiotic resistance. **13**, 42 (2014).

22. S. Sachdeva, R. V Palur, K. U. Sudhakar, T. Rathinavelan, E. coli Group 1 Capsular Polysaccharide Exportation Nanomachinary as a Plausible Antivirulence Target in the Perspective of Emerging Antimicrobial Resistance. *Front. Microbiol.* **8** (2017).

23. C. G. Starr, W. C. Wimley, Antimicrobial peptides are degraded by the cytosolic proteases of human erythrocytes. *Biochim Biophys Acta Biomembr* **1859**, 2319–2326 (2017).

24. G. Wang, X. Li, Z. Wang, APD3: the antimicrobial peptide database as a tool for research and education. *Nucleic Acids Res.* **44**, D1087–D1093 (2016).

25. G. Gabernet, A. T. Müller, J. A. Hiss, G. Schneider, Membranolytic anticancer peptides. *Medchemcomm* **7**, 2232–2245 (2016).

26. A. Giuliani, *et al.*, Antimicrobial peptides: natural templates for synthetic membrane-active compounds. *Cell Mol Life Sci* **65**, 2450–2460 (2008).

27. D. Tang, R. Kang, C. B. Coyne, H. J. Zeh, M. T. Lotze, PAMPs and DAMPs: Signal 0s that Spur Autophagy and Immunity. *Immunol Rev* **249**, 158–175 (2012).

28. N. Malanovic, K. Lohner, Gram-positive bacterial cell envelopes: The impact on the activity of antimicrobial peptides. *Biochim Biophys Acta* **1858**, 936–946 (2016).

29. D. Ciumac, H. Gong, X. Hu, J. R. Lu, Membrane targeting cationic antimicrobial peptides. *J. Colloid Interface Sci.* **537**, 163–185 (2019).

30. W. Dowhan, M. Bogdanov, E. Mileykovskaya, "Functional Roles of Lipids in Membranes" in *Biochemistry of Lipids, Lipoproteins and Membranes*, 6th Ed., N. D. Ridgway, R. S. McLeod, Eds. (Elsevier, 2016), pp. 1–40.

31. C. Sohlenkamp, O. Geiger, Bacterial membrane lipids: Diversity in structures and pathways. *FEMS Microbiol. Rev.* **40**, 133–159 (2016).

32. R. F. Epand, P. B. Savage, R. M. Epand, Bacterial lipid composition and the antimicrobial efficacy of cationic steroid compounds (Ceragenins). *Biochim Biophys Acta* **1768**, 2500–2509 (2007).

33. R. M. Epand, R. F. Epand, Bacterial membrane lipids in the action of antimicrobial agents. *J Pept Sci* **17**, 298–305 (2011).

34. S. Zalba, T. L. Ten Hagen, Cell membrane modulation as adjuvant in cancer therapy. *Cancer Treat Rev* **52**, 48–57 (2017).

35. N. Malanovic, K. Lohner, Antimicrobial peptides targeting Gram-positive bacteria. *Pharmaceuticals* **9**, 59 (2016).

36. R. M. Epand, R. F. Epand, Lipid domains in bacterial membranes and the action of antimicrobial agents. *Biochim. Biophys. Acta - Biomembr.* **1788**, 289–294 (2009).

37. R. N. A. H. Lewis, R. N. McElhaney, The physicochemical properties of cardiolipin bilayers and cardiolipin-containing lipid membranes. *Biochim. Biophys. Acta - Biomembr.* **1788**, 2069–2079 (2009).

38. N. J. Mitchell, P. Seaton, A. Pokorny, Branched phospholipids render lipid vesicles more susceptible to membrane-active peptides. *Biochim Biophys Acta* **1858**, 988–994 (2016).

39. P. Demchick, A. L. Koch, The permeability of the wall fabric of Escherichia coli and Bacillus subtilis. *J Bacteriol* **178**, 768–773 (1996).

40. G. van Meer, A. I. de Kroon, Lipid map of the mammalian cell. *J Cell Sci* **124**, 5–8 (2011).

41. G. van Meer, D. R. Voelker, G. W. Feigenson, Membrane lipids: where they are and how they behave. *Nat Rev Mol Cell Biol* **9**, 112–124 (2008).

42. P. A. Leventis, S. Grinstein, The distribution and function of phosphatidylserine in cellular membranes. *Annu Rev Biophys* **39**, 407–427 (2010).

43. E. London, How principles of domain formation in model membranes may explain ambiguities concerning lipid raft formation in cells. *Biochim. Biophys. Acta - Mol. Cell Res.* (2005) https:/doi.org/10.1016/j.bbamcr.2005.09.002.

44. S. Semrau, T. Schmidt, Membrane heterogeneity - From lipid domains to curvature effects. *Soft Matter* **5**, 3174–3186 (2009).

45. G. M'Baye, Y. Mély, G. Duportail, A. S. Klymchenko, Liquid Ordered and Gel Phases of Lipid Bilayers: Fluorescent Probes Reveal Close Fluidity but Different Hydration. *Biophys. J.* **95**, 1217 (2008).

46. G. W. Feigenson, Phase Boundaries and Biological Membranes. *Annu. Rev. Biophys. Biomol. Struct.* **36**, 63–77 (2007).

47. D. Lingwood, K. Simons, Lipid rafts as a membrane-organizing principle. *Science (80-.).* **327**, 46–50 (2010).

48. S. K. Parks, J. Chiche, J. Pouysségur, Disrupting proton dynamics and energy metabolism for cancer therapy. *Nat. Rev. Cancer* **13**, 611–623 (2013).

49. T. Koltai, S. J. Reshkin, S. Harguindey, "The pH-centered paradigm in cancer" in *An Innovative Approach to Understanding and Treating Cancer: Targeting PH: From Etiopathogenesis to New Therapeutic Avenues*, T. Koltai, S. J. Reshkin, S. B. T.-A. I. A. to U. and T. C. T. pH Harguindey, Eds. (Academic Press, 2020), pp. 53–97.

50. S. Riedl, *et al.*, In search of a novel target - phosphatidylserine exposed by non-apoptotic tumor cells and metastases of malignancies with poor treatment efficacy. *Biochim Biophys Acta* **1808**, 2638–2645 (2011).

51. S. Riedl, *et al.*, Human lactoferricin derived di-peptides deploying loop structures induce apoptosis specifically in cancer cells through targeting membranous phosphatidylserine. *Biochim Biophys Acta* **1848**, 2918–2931 (2015).

52. B. Sharma, S. S. Kanwar, Phosphatidylserine: A cancer cell targeting biomarker. *Semin Cancer Biol* (2017) https:/doi.org/10.1016/j.semcancer.2017.08.012.

53. R. F. Zwaal, P. Comfurius, E. M. Bevers, Surface exposure of phosphatidylserine in pathological cells. *Cell Mol Life Sci* **62**, 971–988 (2005).

54. S. Riedl, D. Zweytick, K. Lohner, Membrane-active host defense peptides--challenges and perspectives for the development of novel anticancer drugs. *Chem Phys Lipids* **164**, 766–781 (2011).

55. L. T. Tan, *et al.*, Targeting Membrane Lipid a Potential Cancer Cure? *Front Pharmacol* **8**, 12 (2017).

56. S. Büyüktiryaki, R. Say, A. Denizli, A. Ersöz, Phosphoserine imprinted nanosensor for detection of Cancer Antigen 125. *Talanta* **167**, 172–180 (2017).

57. A. C. Alves, D. Ribeiro, C. Nunes, S. Reis, Biophysics in cancer: The relevance of drug-membrane interaction studies. *Biochim Biophys Acta* **1858**, 2231–2244 (2016).

58. G. Staneva, C. Chachaty, C. Wolf, K. Koumanov, P. J. Quinn, The role of sphingomyelin in regulating phase coexistence in complex lipid model membranes: Competition between ceramide and cholesterol. *Biochim. Biophys. Acta - Biomembr.* **1778**, 2727–2739 (2008).

59. P. J. Quinn, C. Wolf, The liquid-ordered phase in membranes. *Biochim. Biophys. Acta - Biomembr.* **1788**, 33–46 (2009).

60. Z. Huang, E. London, Cholesterol lipids and cholesterol-containing lipid rafts in bacteria. *Chem Phys Lipids* **199**, 11–16 (2016).

61. A. V. Krylov, P. Pohl, M. L. Zeidel, W. G. Hill, Water permeability of asymmetric planar lipid bilayers: Leaflets of different composition offer independent and additive resistances to permeation. *J. Gen. Physiol.* **118**, 333–339 (2001).

62. F. Harris, S. R. Dennison, J. Singh, D. A. Phoenix, On the selectivity and efficacy of defense peptides with respect to cancer cells. *Med Res Rev* **33**, 190–234 (2013).

63. W. C. Wimley, Describing the mechanism of antimicrobial peptide action with the interfacial activity model. *ACS Chem Biol* **5**, 905–917 (2010).

64. W. C. Wimley, K. Hristova, Antimicrobial peptides: successes, challenges and unanswered questions. *J Membr Biol* **239**, 27–34 (2011).

65. K. A. Camilio, "Short Lytic Anticancer Peptides as a Novel Therapy against Cancer A dissertation for the degree of Philosophiae Doctor," University of Tromsø, Tromsø. (2013).

66. D. W. Hoskin, A. Ramamoorthy, Studies on anticancer activities of antimicrobial peptides. *Biochim. Biophys. Acta - Biomembr.* **1778**, 357–375 (2008).

67. R. Bilginer, A. Arslan Yildiz, "Biomimetic Model Membranes as Drug Screening Platform" in (2019), pp. 225–247.

68. J. T. Marquês, C. A. C. Antunes, F. C. Santos, R. F. M. de Almeida, "Biomembrane Organization and Function: The Decisive Role of Ordered Lipid Domains" in *Advances in Planar Lipid Bilayers and Liposomes*, A. Iglič, C. V Kulkarni, M. Rappolt, Eds. (Academic Press, 2015), pp. 65–96.

69. L. T. Nguyen, E. F. Haney, H. J. Vogel, The expanding scope of antimicrobial peptide structures and their modes of action. *Trends Biotechnol* **29**, 464–472 (2011).

70. S. R. Dennison, M. Whittaker, F. Harris, D. A. Phoenix, Anticancer alpha-helical peptides and structure/function relationships underpinning their interactions with tumour cell membranes. *Curr. Protein Pept. Sci.* **7**, 487–499 (2006).

71. S. R. Dennison, F. Harris, T. Bhatt, J. Singh, D. A. Phoenix, *A theoretical analysis of secondary structural characteristics of anticancer peptides* (2010).

72. E. Cox, A. Michalak, S. Pagentine, P. Seaton, A. Pokorny, Lysylated phospholipids stabilize models of bacterial lipid bilayers and protect against antimicrobial peptides. *Biochim Biophys Acta* **1838**, 2198–2204 (2014).

73. M. A. Sani, F. Separovic, How Membrane-Active Peptides Get into Lipid Membranes. *Acc Chem Res* **49**, 1130–1138 (2016).

74. M. Pasupuleti, A. Schmidtchen, M. Malmsten, Antimicrobial peptides: key components of the innate immune system. *Crit Rev Biotechnol* **32**, 143–171 (2012).

75. A. Pokorny, P. F. F. Almeida, Permeabilization of Raft-Containing Lipid Vesicles by δ-

Lysin: A Mechanism for Cell Sensitivity to Cytotoxic Peptides. *Biochemistry* **44**, 9538–9544 (2005).

76. V. Teixeira, M. J. Feio, M. Bastos, Role of lipids in the interaction of antimicrobial peptides with membranes. *Prog Lipid Res* **51**, 149–177 (2012).

77. M. R. Yeaman, N. Y. Yount, Mechanisms of antimicrobial peptide action and resistance. *Pharmacol. Rev.* **55**, 27–55 (2003).

78. N. Y. Yount, M. R. Yeaman, Emerging Themes and Therapeutic Prospects for Anti-Infective Peptides. *Annu. Rev. Pharmacol. Toxicol.* **52**, 337–360 (2012).

79. G. Gabernet, *et al.*, In silico design and optimization of selective membranolytic anticancer peptides. *Sci Rep* **9**, 1–11 (2019).

80. J. P. S. Powers, R. E. W. Hancock, The relationship between peptide structure and antibacterial activity. *Peptides* **24**, 1681–1691 (2003).

81. P. K. Hazam, G. Jerath, A. Kumar, N. Chaudhary, V. Ramakrishnan, Effect of tacticity-derived topological constraints in bactericidal peptides. *Biochim Biophys Acta Biomembr* **1859**, 1388–1395 (2017).

82. B. Bechinger, Structure and Function of Membrane-Lytic Peptides. *CRC. Crit. Rev. Plant Sci.* **23**, 271–292 (2004).

83. Y. B. Huang, L. Y. He, H. Y. Jiang, Y. X. Chen, Role of helicity on the anticancer mechanism of action of cationic-helical peptides. *Int J Mol Sci* **13**, 6849–6862 (2012).

84. R. M. Epand, R. F. Epand, Lipid domains in bacterial membranes and the action of antimicrobial agents. *Biochim. Biophys. Acta - Biomembr.* **1788**, 289–294 (2009).

85. F. G. Avci, B. S. Akbulut, E. Ozkirimli, Membrane Active Peptides and Their Biophysical Characterization. *Biomolecules* **8** (2018).

86. E. Eiríksdóttir, K. Konate, Ü. Langel, G. Divita, S. Deshayes, Secondary structure of cell-penetrating peptides controls membrane interaction and insertion. *Biochim Biophys Acta Biomembr.* **1798**, 1119–1128 (2010).

87. Y. H. Huang, S. Chaousis, O. Cheneval, D. J. Craik, S. T. Henriques, Optimization of the cyclotide framework to improve cell penetration properties. *Front Pharmacol* **6**, 17 (2015).

88. S. T. Henriques, D. J. Craik, Importance of the cell membrane on the mechanism of action of cyclotides. *ACS Chem Biol* **7**, 626–636 (2012).

89. S. Troeira Henriques, D. J. Craik, Cyclotide Structure and Function: The Role of Membrane Binding and Permeation. *Biochemistry* **56**, 669–682 (2017).

90. S. T. Henriques, *et al.*, Phosphatidylethanolamine binding is a conserved feature of

cyclotide-membrane interactions. *J Biol Chem* **287**, 33629–33643 (2012).

91. C. G. Cranfield, *et al.*, Kalata B1 and Kalata B2 Have a Surfactant-Like Activity in Phosphatidylethanolomine-Containing Lipid Membranes. *Langmuir* **33**, 6630–6637 (2017).

92. S. T. Henriques, *et al.*, The Prototypic Cyclotide Kalata B1 Has a Unique Mechanism of Entering Cells. *Chem Biol* **22**, 1087–1097 (2015).

93. F. M. Li, X. Q. Wang, Identifying anticancer peptides by using improved hybrid compositions. *Sci Rep* **6**, 33910 (2016).

94. W. Chen, H. Ding, P. Feng, H. Lin, K.-C. Chou, iACP: a sequence-based tool for identifying anticancer peptides. *Oncotarget* **7**, 16895–16909 (2016).

95. K. Andreev, *et al.*, Guanidino groups greatly enhance the action of antimicrobial peptidomimetics against bacterial cytoplasmic membranes. *Biochim Biophys Acta* **1838**, 2492–2502 (2014).

96. Y. B. Huang, X. F. Wang, H. Y. Wang, Y. Liu, Y. Chen, Studies on mechanism of action of anticancer peptides by modulation of hydrophobicity within a defined structural framework. *Mol Cancer Ther* **10**, 416–426 (2011).

97. N. Papo, New Lytic Peptides Based on the D,L-Amphipathic Helix Motif Preferentially KillTumor Cells Compared to Normal Cells. *Biochemistry* **42** (2003).

98. Z. Y. Ong, *et al.*, Effect of stereochemistry, chain length and sequence pattern on antimicrobial properties of short synthetic β-sheet forming peptide amphiphiles. *Biomaterials* **35**, 1315–1325 (2014).

99. N. Papo, A. Braunstein, Z. Eshhar, Y. Shai, Suppression of human prostate tumor growth in mice by a cytolytic D-, L-amino acid peptide: Membrane lysis, increased necrosis, and inhibition of prostate-specific antigen secretion. *Cancer Res.* **64**, 5779–5786 (2004).

100. N. Papo, *et al.*, Inhibition of Tumor Growth and Elimination of Multiple Metastases in Human Prostate and Breast Xenografts by Systemic Inoculation of a Host Defense–Like Lytic Peptide. *Cancer Res.* **66**, 5371–5378 (2006).

101. M. Abdolhosseini, S. R. Nandula, J. Song, H. Hirt, S.-U. Gorr, Lysine substitutions convert a bacterial-agglutinating peptide into a bactericidal peptide that retains anti-lipopolysaccharide activity and low hemolytic activity. *Peptides* **35**, 231–238 (2012).

102. M. Abdolhosseini, J. B. Sotsky, A. P. Shelar, P. B. Joyce, S. U. Gorr, Human parotid secretory protein is a lipopolysaccharide-binding protein: identification of an anti-inflammatory peptide domain. *Mol Cell Biochem* **359**, 1–8 (2012).

103. A. V. R. da Silva, *et al.*, The effects of the C-terminal amidation of mastoparans on their biological actions and interactions with membrane-mimetic systems. *Biochim. Biophys. Acta - Biomembr.* **1838**, 2357–2368 (2014).

104. S. R. Dennison, D. A. Phoenix, Influence of C-Terminal Amidation on the Efficacy of Modelin-5. *Biochemistry* **50**, 1514–1523 (2011).

105. H. Hirt, S. U. Gorr, Antimicrobial peptide GL13K is effective in reducing biofilms of Pseudomonas aeruginosa. *Antimicrob Agents Chemother* **57**, 4903–4910 (2013).

106. K. V. Holmberg, *et al.*, Bio-inspired stable antimicrobial peptide coatings for dental applications. *Acta Biomater.* **9**, 8224–8231 (2013).

107. V. Balhara, R. Schmidt, S. U. Gorr, C. Dewolf, Membrane selectivity and biophysical studies of the antimicrobial peptide GL13K. *Biochim Biophys Acta* **1828**, 2193–2203 (2013).

108. S.-U. Gorr, C. M. Flory, R. J. Schumacher, In vivo activity and low toxicity of the second-generation antimicrobial peptide DGL13K. *PLoS One* **14**, e0216669 (2019).

109. N. Harmouche, *et al.*, Solution and Solid-State Nuclear Magnetic Resonance Structural Investigations of the Antimicrobial Designer Peptide GL13K in Membranes. *Biochemistry* **56**, 4269–4278 (2017).

110. X. Chen, H. Hirt, Y. Li, S. U. Gorr, C. Aparicio, Antimicrobial GL13K peptide coatings killed and ruptured the wall of *Streptococcus gordonii* and prevented formation and growth of biofilms. *PLoS One* **9**, e111579 (2014).

111. H. Youssef, C. E. DeWolf, Interfacial Self-Assembly of Antimicrobial Peptide GL13K into Non-Fibril Crystalline β-Sheets. *Langmuir* **36**, 660–665 (2020).

112. H. Youssef, "Interfacial behaviour of β-sheet forming antimicrobial peptide GL13K," Concordia University. (2019).

113. A. Grau-Campistany, *et al.*, Hydrophobic mismatch demonstrated for membranolytic peptides, and their use as molecular rulers to measure bilayer thickness in native cells. *Sci Rep* **5**, 9388 (2015).

114. K. Murzyn, T. Rog, M. Pasenkiewicz-Gierula, Phosphatidylethanolamine-phosphatidylglycerol bilayer as a model of the inner bacterial membrane. *Biophys J* **88**, 1091–1103 (2005).

115. A.-B. Hachmann, *et al.*, Reduction in Membrane Phosphatidylglycerol Content Leads to Daptomycin Resistance in Bacillus subtilis. *Antimicrob. Agents Chemother.* **55**, 4326–4337 (2011).

116. G. Wang, B. Mishra, R. F. Epand, R. M. Epand, High-quality 3D structures shine light on antibacterial, anti-biofilm and antiviral activities of human cathelicidin LL-37 and its fragments. *Biochim. Biophys. Acta - Biomembr.* **1838**, 2160–2172 (2014).

117. J. P. Michel, *et al.*, Charge and aggregation pattern govern the interaction of plasticins with LPS monolayers mimicking the external leaflet of the outer membrane of Gram-negative

bacteria. *Biochim Biophys Acta* **1848**, 2967–2979 (2015).

118. F. Graef, *et al.*, The bacterial cell envelope as delimiter of anti-infective bioavailability - An in vitro permeation model of the Gram-negative bacterial inner membrane. *J Control Release* **243**, 214–224 (2016).

119. N. Malanovic, *et al.*, Phospholipid-driven differences determine the action of the synthetic antimicrobial peptide OP-145 on Gram-positive bacterial and mammalian membrane model systems. *Biochim Biophys Acta* **1848**, 2437–2447 (2015).

120. A. Schmidtchen, I. M. Frick, E. Andersson, H. Tapper, L. Björck, Proteinases of common pathogenic bacteria degrade and inactivate the antibacterial peptide LL-37. *Mol. Microbiol.* **46**, 157–168 (2002).

121. C. de la Fuente-Nunez, *et al.*, D-enantiomeric peptides that eradicate wild-type and multidrug-resistant biofilms and protect against lethal Pseudomonas aeruginosa infections. *Chem Biol* **22**, 196–205 (2015).

122. H. Hirt, J. W. Hall, E. Larson, S. U. Gorr, A D-enantiomer of the antimicrobial peptide GL13K evades antimicrobial resistance in the Gram positive bacteria Enterococcus faecalis and Streptococcus gordonii. *PLoS One* **13**, e0194900 (2018).

123. C. Sinthuvanich, *et al.*, Anticancer beta-hairpin peptides: membrane-induced folding triggers activity. *J Am Chem Soc* **134**, 6210–6217 (2012).

124. F. Savini, S. Bobone, D. Roversi, M. L. Mangoni, L. Stella, From liposomes to cells: Filling the gap between physicochemical and microbiological studies of the activity and selectivity of host-defense peptides. *Pept. Sci.* **110**, e24041 (2018).

125. C. M. Nair, M. Vijayan, Y. V. Venkatachalapathi, P. Balaram, X-ray crystal structure of pivaloyl-D-Pro-L-Pro-L-Ala-N-methylamide; observation of a consecutive β-turn conformation. *J. Chem. Soc. Chem. Commun.* (1979) https:/doi.org/10.1039/C39790001183.

126. K. A. Reid, C. M. Davis, R. B. Dyer, J. T. Kindt, Binding, folding and insertion of a beta-hairpin peptide at a lipid bilayer surface: Influence of electrostatics and lipid tail packing. *Biochim Biophys Acta Biomembr* **1860**, 792–800 (2018).

127. S. Ran, P. E. Thorpe, Phosphatidylserine is a marker of tumor vasculature and a potential target for cancer imaging and therapy. *Int. J. Radiat. Oncol.* **54**, 1479–1484 (2002).

128. Y. H. Huang, *et al.*, The biological activity of the prototypic cyclotide kalata b1 is modulated by the formation of multimeric pores. *J Biol Chem* **284**, 20699–20707 (2009).

129. J. H. Stafford, P. E. Thorpe, Increased exposure of phosphatidylethanolamine on the surface of tumor vascular endothelium. *Neoplasia* **13**, 299–308 (2011).

130. B. Almarwani, *et al.*, Vesicles mimicking normal and cancer cell membranes exhibit differential responses to the cell-penetrating peptide Pep-1. *Biochim Biophys Acta*

Biomembr **1860**, 1394–1402 (2018).

131. H. Tominaga, *et al.*, A water-soluble tetrazolium salt useful for colorimetric cell viability assay. *Anal. Commun.* **36**, 47–50 (1999).

132. T. Tsukatani, *et al.*, Colorimetric microbial viability assay based on reduction of water-soluble tetrazolium salts for antimicrobial susceptibility testing and screening of antimicrobial substances. *Anal. Biochem.* **393**, 117–125 (2009).

133. W. Cao, *et al.*, Large-scale lipid analysis with C=C location and sn-position isomer resolving power. *Nat. Commun.* **11**, 1–11 (2020).

134. H. Mohwald, Phospholipid And Phospholipid-Protein Monolayers At The Air/Water Interface. *Annu. Rev. Phys. Chem.* (1990) https:/doi.org/10.1146/annurev.physchem.41.1.441.

135. C. Stefaniu, G. Brezesinski, X-ray investigation of monolayers formed at the soft air/water interface. *Curr. Opin. Colloid Interface Sci.* **19**, 216–227 (2014).

136. S. Behyan, *et al.*, Nanoparticle-induced structural changes in lung surfactant membranes: an X-ray scattering study. *Environ. Sci. Nano* **5**, 1218–1230 (2018).

137. T. R. Jensen, K. Balashev, T. Bjørnholm, K. Kjaer, Novel methods for studying lipids and lipases and their mutual interaction at interfaces. Part II. Surface sensitive synchrotron X-ray scattering. *Biochimie* **83**, 399–408 (2001).

138. R. Mendelsohn, C. R. Flach, "Infrared Reflection – Absorption Spectrometry of Monolayer Films at the Air – Water Interface" in *Handbook of Vibrational Spectroscopy*, (2002) https:/doi.org/doi:10.1002/0470027320.s2205.

139. E. Maltseva, "Model membrane interactions with ions and peptides at the air/water interface Dissertation," Universität Potsdam. (2005).

140. S. Castano, B. Desbat, J. Dufourcq, Ideally amphipathic β-sheeted peptides at interfaces: structure, orientation, affinities for lipids and hemolytic activity of (KL)mK peptides. *Biochim. Biophys. Acta - Biomembr.* **1463**, 65–80 (2000).

141. S. Castano, B. Desbat, M. Laguerre, J. Dufourcq, Structure, orientation and affinity for interfaces and lipids of ideally amphipathic lytic LiKj(i=2j) peptides. *Biochim. Biophys. Acta - Biomembr.* **1416**, 176–194 (1999).

142. R. Mendelsohn, G. Mao, C. R. Flach, Infrared reflection–absorption spectroscopy: Principles and applications to lipid–protein interaction in Langmuir films. *Biochim. Biophys. Acta - Biomembr.* **1798**, 788–800 (2010).

143. D. Blaudez, S. Castano, B. Desbat, "PM-IRRAS at liquid interfaces" in *Biointerface Characterization by Advanced IR Spectroscopy*, 1st Ed., C. M. Pradier, Y. J. Chabal, Eds. (2011) https:/doi.org/10.1016/B978-0-444-53558-0.00002-3.

144. H. Bourque, *et al.*, Investigation of the poly(L-lactide)/poly(D-lactide) stereocomplex at the air-water interface by polarization modulation infrared reflection absorption spectroscopy. *Langmuir* **17**, 5842–5849 (2001).

145. A. Renault, *et al.*, Surface properties and conformation of Nephila clavipes spider recombinant silk proteins at the air-water interface. *Langmuir* **25**, 8170–8180 (2009).

146. S. Morandat, S. Azouzi, E. Beauvais, A. Mastouri, K. El Kirat, Atomic force microscopy of model lipid membranes. *Anal. Bioanal. Chem.* **405**, 1445–1461 (2013).

147. A. Micsonai, *et al.*, Accurate secondary structure prediction and fold recognition for circular dichroism spectroscopy. *Proc Natl Acad Sci U S A* **112**, E3095-103 (2015).

148. A. Micsonai, *et al.*, BeStSel: a web server for accurate protein secondary structure prediction and fold recognition from the circular dichroism spectra. *Nucleic Acids Res* **46**, W315–W322 (2018).

149. S. Rex, Pore formation induced by the peptide melittin in different lipid vesicle membranes. *Biophys. Chem.* **58**, 75–85 (1996).

150. J. C. Stewart, Colorimetric determination of phospholipids with ammonium ferrothiocyanate. *Anal Biochem* **104**, 10–14 (1980).

151. J. Jimah, P. Schlesinger, N. Tolia, Liposome Disruption Assay to Examine Lytic Properties of Biomolecules. *Bio-Protocol* **7**, 1–12 (2017).

152. K. A. Willets, R. P. Van Duyne, Localized surface plasmon resonance spectroscopy and sensing. *Annu Rev Phys Chem* **58**, 267–297 (2007).

153. J. Hoyo, J. Torrent-Burgués, T. Tzanov, Physical states and thermodynamic properties of model gram-negative bacterial inner membranes. *Chem. Phys. Lipids* **218**, 57–64 (2019).

154. J. P. Michel, Y. X. Wang, I. Kiesel, Y. Gerelli, V. Rosilio, Disruption of Asymmetric Lipid Bilayer Models Mimicking the Outer Membrane of Gram-Negative Bacteria by an Active Plasticin. *Langmuir* **33**, 11028–11039 (2017).

155. S. Afonin, V. Kubyshkin, P. K. Mykhailiuk, I. V. Komarov, A. S. Ulrich, Conformational Plasticity of the Cell-Penetrating Peptide SAP As Revealed by Solid-State 19 F-NMR and Circular Dichroism Spectroscopies. *J. Phys. Chem. B* **121**, 6479–6491 (2017).

156. R. Sneer, M. J. Weygand, K. Kjaer, D. A. Tirrell, H. Rapaport, Parallel beta-sheet assemblies at interfaces. *Chemphyschem* **5**, 747–750 (2004).

157. M. Lepère, A. H. Muenter, C. Chevallard, P. Guenoun, G. Brezesinski, Comparative IR and X-ray studies of natural and model amyloid peptides at the air/water interface. *Colloids Surfaces A Physicochem. Eng. Asp.* **303**, 73–78 (2007).

158. E. Y. Chi, *et al.*, Lipid membrane templates the ordering and induces the fibrillogenesis of

Alzheimer's disease amyloid-β peptide. *Proteins* **72**, 1–24 (2008).

159. A. Barth, Infrared spectroscopy of proteins. *Biochim. Biophys. Acta - Bioenerg.* **1767**, 1073–1101 (2007).

160. M. Hoernke, J. A. Falenski, C. Schwieger, B. Koksch, G. Brezesinski, Triggers for beta-sheet formation at the hydrophobic-hydrophilic interface: high concentration, in-plane orientational order, and metal ion complexation. *Langmuir* **27**, 14218–14231 (2011).

161. H. Lavoie, *et al.*, Spectroscopic and structural properties of valine gramicidin A in monolayers at the air-water interface. *Biophys. J.* **83**, 3558–3569 (2002).

162. W. Dowhan, M. Bogdanov, E. Mileykovskaya, "Functional Roles of Lipids in Membranes" in *Biochemistry of Lipids, Lipoproteins and Membranes*, (Elsevier, 2016), pp. 1–40.

163. K. Y. C. Lee, *et al.*, Synchrotron x-ray study of lung surfactant-specific protein SP-B in lipid monolayers. *Biophys. J.* (2001) https:/doi.org/10.1016/S0006-3495(01)75724-4.

164. T. R. Jahn, *et al.*, The Common Architecture of Cross-β Amyloid. *J. Mol. Biol.* **395**, 717–727 (2010).

165. Z. Ye, *et al.*, Self-assembly dynamics and antimicrobial activity of all l- and d-amino acid enantiomers of a designer peptide. *Nanoscale* **11**, 266–275 (2019).

166. A. Won, *et al.*, Investigating the effects of L- to D-amino acid substitution and deamidation on the activity and membrane interactions of antimicrobial peptide anoplin. *Biochim. Biophys. Acta - Biomembr.* **1808**, 1592–1600 (2011).

167. I. Wiegand, K. Hilpert, R. E. W. Hancock, Agar and broth dilution methods to determine the minimal inhibitory concentration (MIC) of antimicrobial substances. *Nat. Protoc. 2008 32* **3**, 163–175 (2008).

168. H. Zhao, *et al.*, The development of activatable lytic peptides for targeting triple negative breast cancer. *Cell Death Discov.* **3**, 17037 (2017).

169. H. A. Rinia, M. M. E. Snel, J. P. J. M. van der Eerden, B. De Kruijff, Imaging domains in model membranes with atomic force microscopy. *FEBS Lett.* **504**, 194–199 (2001).

170. A. Won, A. Ruscito, A. Ianoul, Imaging the membrane lytic activity of bioactive peptide latarcin 2a. *Biochim. Biophys. Acta - Biomembr.* **1818**, 3072–3080 (2012).

171. M. Gandhavadi, D. Allende, A. Vidal, S. A. Simon, T. J. McIntosh, Structure, Composition, and Peptide Binding Properties of Detergent Soluble Bilayers and Detergent Resistant Rafts. *Biophys. J.* **82**, 1469–1482 (2002).

172. S. L. Veatch, S. L. Keller, Miscibility phase diagrams of giant vesicles containing sphingomyelin. *Phys. Rev. Lett.* **94**, 3–6 (2005).

173. R. S. Petruzielo, F. A. Heberle, P. Drazba, J. Katsaras, G. W. Feigenson, Phase behavior and domain size in sphingomyelin-containing lipid bilayers. *Biochim. Biophys. Acta - Biomembr.* **1828**, 1302–1313 (2013).

174. E. Bellet-Amalric, *et al.*, Interaction of the third helix of Antennapedia homeodomain and a phospholipid monolayer, studied by ellipsometry and PM-IRRAS at the air–water interface. *Biochim. Biophys. Acta (BBA)-Biomembranes* **1467**, 131–143 (2000).

175. H. Youssef, C. E. Dewolf, Interfacial Self-Assembly of Antimicrobial Peptide GL13K into Non-Fibril Crystalline β-Sheets. *Langmuir* (2020) https:/doi.org/10.1021/acs.langmuir.9b03120.

176. F. Orsini, *et al.*, Atomic force microscopy imaging of lipid rafts of human breast cancer cells. *Biochim. Biophys. Acta - Biomembr.* **1818**, 2943–2949 (2012).

177. J. M. Henderson, A. J. Waring, F. Separovic, K. Y. C. Lee, Antimicrobial Peptides Share a Common Interaction Driven by Membrane Line Tension Reduction. *Biophys J* **111**, 2176–2189 (2016).

178. J. R. Giorgione, Z. Huang, R. M. Epand, Increased activation of protein kinase C with cubic phase lipid compared with liposomes. *Biochemistry* **37**, 2384–2392 (1998).

179. S. Mallik, R. Prasad, A. Bhattacharya, P. Sen, Synthesis of Phosphatidylserine and Its Stereoisomers: Their Role in Activation of Blood Coagulation. *ACS Med Chem Lett* **9**, 434–439 (2018).

180. R. M. Epand, S. D. Rychnovsky, J. D. Belani, R. F. Epand, Role of chirality in peptide-induced formation of cholesterol-rich domains. *Biochem. J.* **390**, 541–548 (2005).

181. S. K. Samal, *et al.*, Cationic polymers and their therapeutic potential. *Chem Soc Rev* **41**, 7147–7194 (2012).

182. P. Sahariah, *et al.*, Antimicrobial peptide shows enhanced activity and reduced toxicity upon grafting to chitosan polymers. *Chem Commun* **51**, 11611–11614 (2015).

183. S. J. Reshkin, R. A. Cardone, S. Harguindey, Na+-H+ Exchanger, pH Regulation and Cancer. *Recent Pat. Anticancer. Drug Discov.* **8**, 85–99 (2012).

184. S. Harguindey, *et al.*, Cariporide and other new and powerful NHE1 inhibitors as potentially selective anticancer drugs - an integral molecular/biochemical/metabolic/clinical approach after one hundred years of cancer research. *J. Transl. Med.* **11**, 282 (2013).

185. C. Chen, *et al.*, A prodrug strategy based on chitosan for efficient intracellular anticancer drug delivery. *Nanotechnology* **25**, 255101 (2014).